Lower Crustal Heterogeneity and Fractional Crystallisation Control Evolution of Small Volume Magma Batches at Ocean Island Volcanoes (Ascension Island, South Atlantic)

K. J. CHAMBERLAIN[1, 2*], J. BARCLAY[3], K. J. PREECE[4], R. J. BROWN[1], J. P. DAVIDSON[1]

[1] DEPARTMENT OF EARTH SCIENCES, DURHAM UNIVERSITY, DURHAM, DH1 3LE, UK
[2] SCHOOL OF ENVIRONMENTAL SCIENCES, UNIVERSITY OF DERBY, DERBY, DE22 1GB, UK
[3] SCHOOL OF ENVIRONMENTAL SCIENCES, UNIVERSITY OF EAST ANGLIA, NORWICH, NR4 7TJ, UK
[4] DEPARTMENT OF GEOGRAPHY, COLLEGE OF SCIENCE, SWANSEA UNIVERSITY, SINGLETON PARK, SWANSEA, SA2 8PP, UK

Manuscript for: *Journal of Petrology*
Running title: Evolution of Ascension Island magmatism

Keywords: Ascension Island, ocean island volcanism, fractional crystallisation, magmatic processes, oceanic crust

*Corresponding author. Phone (+44-1332-592971)
Email address: k.chamberlain@derby.ac.uk

41 **ABSTRACT**

42 Ocean island volcanoes erupt a wide range of magmatic compositions via a diverse range of
43 eruptive styles. Understanding where and how these melts evolve is thus an essential
44 component in the anticipation of future volcanic activity. Here we examine the role of crustal
45 structure and magmatic flux in controlling the location, evolution and ultimately composition
46 of melts at Ascension Island. Ascension Island, in the south Atlantic, is an ocean island
47 volcano which has produced a continuum of eruptive compositions from basalt to rhyolite in
48 its 1-million-year subaerial eruptive history. Volcanic rocks broadly follow a silica-
49 undersaturated subalkaline evolutionary trend and new data presented here show a continuous
50 compositional trend from basalt through trachyte to rhyolite. Detailed petrographic
51 observations are combined with *in-situ* geochemical analyses of crystals and glass, and new
52 whole rock major and trace element data from mafic and felsic pyroclastic and effusive
53 deposits that span the entire range in eruptive ages and compositions found on Ascension
54 Island. These data show that extensive fractional crystallisation is the main driver for the
55 production of felsic melt for Ascension Island; a volcano built on thin, young, oceanic crust.
56 Strong spatial variations in the compositions of erupted magmas reveals the role of a
57 heterogeneous lower crust: differing degrees of interaction with a zone of plutonic rocks are
58 responsible for the range in mafic lava composition, and for the formation of the central and
59 eastern felsic complexes. A central core of nested small-scale plutonic, or mush-like, bodies
60 inhibits the ascent of mafic magmas, allowing sequential fractional crystallisation within the
61 lower crust, and generating felsic magmas in the core of the island. There is no evidence for
62 magma mixing preserved in any of the studied eruptions, suggesting that magma storage
63 regions are transient, and material is not recycled between eruptions.

64

65 **INTRODUCTION**

Ocean island volcanoes remain enigmatic in terms of their origin (Niu et al., 2011), evolution and ability to produce a range of magmatic compositions and eruptive activity. Many ocean islands such as Iceland, Socorro, and the archipelagos of Hawaii, the Galapagos and the Canaries have been studied in detail (e.g. Sparks & Sigurdsson, 1987; Geist et al., 1988; Ablay et al., 1998; Geist et al., 1995; Bohrson et al., 1996; Harpp & White, 2001; Koppers & Staudigel, 2005; Carracedo et al., 2007; Carley et al., 2011; Mancini et al., 2015), but some ocean island volcanoes remain relatively poorly understood (e.g. the Azores, St Helena), and yet still pose a significant hazard to populations often living proximal to volcanic vents. Ascension Island, in the south Atlantic, is an example of the latter. It is small (subaerial dimensions of 8 km by 12 km), has no associated hotspot trace (cf. Hawaii, the Canaries; e.g. Zhao, 2004; Montelli et al., 2004) and has erupted magmas with a wide range of compositions (Daly, 1925; Coombs, 1963; Weaver et al., 1996; Kar et al., 1998; Jicha et al., 2013). This compositional diversity is matched by a diversity in eruption styles and range of volcanic deposits (Weaver et al., 1996; Kar et al., 1998; Hobson, 2001; Preece et al., 2016).

Evolved, more felsic, melts have the potential to generate significant hazards at ocean island volcanoes, and thus understanding where and how they evolve in the crust is imperative to forecasting future styles of eruption. The various means by which felsic magmas evolve have the potential to produce a range of compositions, which affects magmatic viscosity (Papale et al., 1998), and the amount of dissolved volatiles, all of which contribute to the mode of evacuation of magma from crustal storage regions (e.g. Eichelberger, 1995; Giordano et al., 2004). At ocean islands these silicic melts are considered to be generated via: anatexis of crustal material by hotter mafic melts (e.g. Sverrisdottir, 2007; Carley et al., 2011; Kuritani et al., 2011); extensive crystal fractionation from a more primitive mafic magma (e.g.Geist et al., 1995; Mungall & Martin, 1995; Larrea et al., 2014; Jeffrey et al., 2016); from direct derivation from mantle partial melting (Ashwal

et al., 2016) or through a combination of these processes (e.g. Bohrson & Reid, 1997; Wiesmaier et al., 2013; Sliwinski et al., 2015). Understanding the relative importance of these processes in any one setting has significant implications for understanding the relationships between the timescales of magma genesis, magmatic heat flux and potential triggering mechanisms of eruptions.

Ascension Island has produced more than 70 explosive eruptions of felsic magma in its ~ 1 Myr subaerial history (Preece et al., 2016), in addition to numerous eruptions that produced scoria cones, mafic lava flows, and felsic lava flows and domes. The erupted rocks have largely been used to investigate the origins of Ascension Island magmatism (e.g. Harris et al., 1982; Weaver et al., 1987, 1996; Weis et al., 1987; Kar, 1997; Kar et al., 1998; Paulick et al., 2010). As yet, little is understood about the magmatic plumbing system on Ascension Island and the control it exerts on magmatic composition and styles of eruptive activity. Thus, we focus here on the relationship between the mafic and felsic magmatism on Ascension, utilising whole rock major and trace element data, and a comprehensive suite of *in situ* crystal major and trace element data by EPMA (electron probe microanalyses) and LA-ICPMS (laser ablation inductively coupled plasma mass spectrometry). Samples studied here represent the products of 22 eruptions representing the full range in composition and eruptive styles presented by subaerial volcanism on Ascension Island. By combining these data with previous isotopic work and work on a compositionally-zoned fall deposit (Chamberlain et al., 2016), we present a model for the magmatic plumbing system of Ascension Island where felsic magmas evolve and stall in the lower crust, and highlight the role of crustal structure in the evolution of felsic melts on ocean islands with a low magmatic flux. Other potentially low magmatic flux ocean islands include the archipelagos of the Azores and Cape Verde islands, and thus the results of this study could be tested at other ocean islands around the world.

ASCENSION ISLAND

Ascension Island (7° 56’ S; 14° 22’ W) is located in the southern Atlantic Ocean, 90 km west of the Mid-Atlantic Ridge (MAR) and 50 km south of the Ascension Fracture Zone (AFZ; Fig. 1). Volcanism began on the sea bed 5 – 6 Myr ago, and subaerial volcanism has occurred from ~1 Ma to present (Kar et al., 1998; Minshull et al., 2010; Paulick et al., 2010; Jicha et al., 2013; Preece et al., 2016). The most recent eruption at Ascension Island has been dated using ^{40}Ar-^{39}Ar dating to 0.51 ± 0.18 ka (Preece et al., 2018) - with no evidence for pauses in eruptive activity of greater than 130 kyr throughout the 1 million years of subaerial volcanism (Jicha et al., 2013).

Crustal structure of Ascension Island

Ascension Island is built on 5 – 7 Myr old oceanic crust (Klingelhöfer et al., 2001; Paulick et al., 2010) on, or close to, the MAR. Due to the OIB-like trace element affinities of Ascension mafic lavas (Harris, 1983; Weaver et al., 1996), it has been suggested that magmatism at Ascension Island is the product of a shallow mantle plume, rising at the MAR then diverted along the Ascension Fracture Zone (AFZ, Fig. 1; Burke & Wilson, 1976; Montelli et al., 2006). However, seismic surveys have revealed a crustal structure that cannot be reconciled with a classic intraplate ocean island (i.e. a lack of lithospheric flexure, cf. Klingelhöfer et al., 2001), and instead suggest that significant growth of the Ascension Island edifice occurred on the MAR-axis. The seismic surveys show that the crust is 12 – 13 km thick under Ascension, with over-thickening of layer 3, to 7 km thick (Klingelhöfer et al., 2001). Active-source seismic tomographic studies failed to find evidence for magmatic underplating beneath the island, suggesting that the island’s origins are not related to a hot spot (Evangelidis et al., 2004). Additionally, Evangelidis et al. (2004) located areas of anomalously high velocity

140 within the middle crust, which were inferred to be the crystallised remains of a relict magma
141 chamber.
142
143 **Geochemical insights into the source of Ascension Island**
144 OIB-like trace element patterns have been measured from magmas erupted on Ascension
145 Island, and spurred extensive research into the origins of magmatism, in particular its
146 relationship to an undefined mantle anomaly and the proximal MAR. Sr and Nd isotopic data
147 show little difference between the subaerial and the (volumetrically dominant) submarine
148 products of Ascension: $^{143}Nd/^{144}Nd$ varies between 0.51292 and 0.51310, and significant
149 variation in $^{87}Sr/^{86}Sr$ has been measured- between 0.70276 and 0.70656 (Fig. 2a; Weaver et
150 al., 1996; Kar et al., 1998; Paulick et al., 2010). Submarine products have distinctly different
151 Hf isotopic characteristics to the subaerial products studied here, and this has lead previous
152 workers to suggest that the mantle source tapped by the submarine stage is no longer present
153 (Fig. 2c; Paulick et al., 2010). There is little variation in Sr, Nd or Pb isotopic characteristics
154 with time in the subaerial edifice (Kar, 1997; Paulick et al., 2010; Jicha et al., 2013), nor is
155 the significant variation in $^{87}Sr/^{86}Sr$ coupled to variations in $^{143}Nd/^{144}Nd$ (Fig. 2a). The large
156 variation in $^{87}Sr/^{86}Sr$ has been suggested to reflect post-emplacement alteration of samples
157 (especially evolved rocks) by seawater-derived groundwater fluids as the samples were not
158 acid-leached prior to analysis (Kar et al., 1998; cf. Davidson et al., 1997). Due to the low Sr-
159 contents of the Ascension magmas, they are particularly susceptible to alteration either
160 through post-emplacement alteration, or by small degrees of assimilation of seawater-altered
161 lithologies (Kar et al., 1998).
162 Previous studies utilised the trace element variation in basaltic magmas erupted on
163 Ascension Island to infer source composition and to define three main magmatic groups,
164 principally based on Zr/Nb ratios (Weaver et al., 1996; Kar, 1997). The oldest and most

165 voluminous magma type in submarine and subaerial Ascension is represented by the high
166 Zr/Nb (Zr/Nb > 5.7) mafic lavas (principally exposed on the south coast, Fig. 1; Weaver et
167 al., 1996; Kar, 1997). Low Zr/Nb (Zr/Nb < 4.3) lavas are relatively spatially restricted,
168 outcropping only in the southwest (Fig. 1). Intermediate Zr/Nb lavas (Zr/Nb 4.3 – 5.7) are the
169 most common lavas in the subaerial history (but have erupted coevally with high and low
170 Zr/Nb lavas), and dominate the northern and western regions (Fig. 1; Weaver et al., 1996;
171 Kar, 1997; Jicha et al., 2013). The origins of these mafic lavas, and the process responsible
172 for their variation has been related to varying degrees of partial melting of a consistent
173 source, or melting of different mantle regions with differing mineralogy (Weaver et al., 1996;
174 Kar, 1997; Jicha et al., 2013). Isotopic and trace element data on the mafic lavas types
175 (Weaver et al., 1996; Kar et al., 1998; Paulick et al., 2010; Jicha et al., 2013), show that
176 fractional crystallisation alone cannot reproduce the variability in Ti, Ta and Nb (Fig. 2c),
177 and that variations in degree of partial melting, or source composition are more likely causes
178 of this variability (Jicha et al., 2013). As the Zr/Nb ratios are more characteristic of
179 variations during the initial production of magma (source lithology or degree of partial
180 melting), and will not be used here to investigate the nature of the magmatic plumbing
181 system.
182
183 **Evolution and distribution of volcanism at Ascension Island**
184 The magmatism on Ascension Island defines a transitional to mildly-alkaline, silica under-
185 saturated array from olivine basalt - hawaiite - mugearite - benmoreite - trachyte - rhyolite
186 (Daly, 1925; Weaver et al., 1996; Fig. 3). Mafic volcanic products are erupted all across the
187 island (Fig. 1), while felsic products are limited to central and eastern areas (Fig. 1). Previous
188 authors have divided the silicic eruptive products into two main centres: the older (Kar et al.,
189 1998; Hobson, 2001; Jicha et al., 2013) central felsic region, which contains the oldest dated

exposed lava on the island (at 1094 ka, Jicha et al., 2013), and the younger eastern complex (youngest published Ar-Ar date of 52 ± 3 ka; Jicha et al., 2013; Fig. 1). Felsic magmas are inferred to be the product of high degrees of fractional crystallisation (Fig. 2c; Weis et al., 1987; Kar et al., 1998; Webster & Rebbert, 2001; Jicha et al., 2013) originating chiefly from similar mafic melts to those erupted around the peripheries of the felsic complexes (both high and intermediate Zr/Nb basalts have been suggested as parental melts; Figs. 1, 2c; Weaver et al., 1996; Kar et al., 1998; Jicha et al., 2013).

The nature of the magmatic plumbing system on Ascension Island has not been established, yet fractional crystallisation is suggested as the dominant process for the formation of felsic melts (Kar et al., 1998; Jicha et al., 2013). There is only limited geochemical evidence for interaction between evolved magma batches to date (Kar et al., 1998; Chamberlain et al., 2016). Melt inclusion compositions and whole rock isotopic ratios of plutonic lithic clasts have been used to infer a genetic association between the plutonic lithics and the spectrum of volcanic rocks (Roedder & Coombs, 1967, Harris et al., 1982, Weis et al., 1987, Webster & Rebbert, 2001). These studies have suggested that the formation of the granitic plutonic bodies occurred at temperatures of 710 – 865 °C, and pressures of 200 – 300 MPa (Webster & Rebbert, 2001, and references therein). Recent work on the crystal cargo and melt inclusions from a compositionally-zoned fall deposit on the island (Chamberlain et al., 2016) supports the hypothesis that felsic magma evolved through closed-system evolution on Ascension (as suggested by Harris, 1986, Weaver et al., 1987), with no petrological or textural evidence for magma mixing or multiple phases of stalling. We test the relevance of this model for the generation of all felsic magmas on Ascension Island, and use these data to improve our understanding of the temporal and spatial relationships between felsic and mafic volcanism.

SAMPLING & METHODOLOGY

The volcanic rocks on Ascension Island are extremely diverse and present evidence for Hawaiian, Strombolian and as well as more explosive (Subplinian to Plinian) eruptions, as well as phreatomagmatic activity. These products include lava flows and domes, pumice, scoria and ash fall deposits and pyroclastic density current deposits (Preece et al., 2016). The products of 22 representative eruptions that cover the full range in magmatic composition, eruptive style (Fig. 3) and the temporal and spatial extent of subaerial volcanism were analysed in detail to capture this range (Fig. 1; Table 1). Mafic lavas outcrop widely across the island and dominate its submarine history (see Nielson & Sibbett, 1996; Minshull et al., 2010). Mafic lava samples were selected to represent the main fields of mafic lava flows found on Ascension Island: the north coast (Sisters; samples AI14-411, AI14-471); the south-west region (Wideawakes; samples AI14-445, AI14-449); the south-east (Letterbox, AI14-423, AI14-429); the south coast (South Coast, AI14-514, AI14-522). In this way, the spatial and temporal variability (old vs. young lavas from the same eruptive centres) of mafic lavas on Ascension Island can be examined (Fig. 1; Table 1). Felsic samples come from effusive and explosive products, including samples from the older central felsic complex (AI-94, AI-103, AI15-621, AI14-459, AI14-488, AI14-493) and the younger eastern felsic complex (AI14-511, AI14-419, AI14-618, AI14-428, AI14-435, AI14-438). These samples were chosen to ensure a wide spatial and temporal sampling of the felsic volcanism (for individual sample names see Table 1).

Scoria and pumice samples were sieved to > 16 mm (or 8 mm if juvenile clasts were less than 16 mm) and all lithic clasts were removed by hand. These samples were then thoroughly cleaned by removing any adhering matrix or oxidised rind followed by soaking in (frequently changed) milli-RO water for a minimum of one week. Lava was treated by removing external, altered material then washed to remove any cutting fluid. All samples

240 were then dried thoroughly at 60 °C prior to crushing. An aliquot of each sample was selected
241 to mill for X-ray fluorescence (XRF) analysis at the University of East Anglia (UEA) using a
242 Brucker-AXS S4 Pioneer. For major elements (>0.5 wt.%) analyses of multiple international
243 standards yielded uncertainties ≤ ± 0.5 wt.% (2σ), except for SiO_2 which yielded
244 uncertainties of ± 1.06 wt.% (2σ). Values of the standards compared with published values
245 yielded accuracies within 2% for all major elements, except for MnO, CaO and P_2O_5 where
246 values were within 9% of published values; for full details of standards used, and their
247 precision see Electronic Appendix 1. Trace element analyses of selected standards gave
248 uncertainties < 5% (2σ) for V, Cr, Ni, Cu, Zn, Rb, Sr, Y, Zr, Nb, Mo and Ba, with
249 uncertainties <10% for As, Ce and U. For full details see Electronic Appendix 1.
250 The remaining material was prepared for *in-situ* analyses of major and trace elements
251 in crystals and glass. Thin sections were made of lava samples, whilst pyroclastic samples
252 were crushed, sieved into various size fractions (< 2 mm), before crystal and glass separates
253 (from the 0.5 – 1 mm size fraction), were hand-picked and mounted into low-activity epoxy
254 discs, and polished.
255 Prior to *in-situ* analyses, back-scattered electron (BSE) images were taken of all thin
256 sections and epoxy blocks to identify crystal phases present, any zonation preserved in
257 crystals and to locate suitable analytical spots. These images were obtained on a JEOL JSM
258 5900LV scanning electron microscope (SEM) at UEA. Percentages of phases were calculated
259 using ImageJ® software of transmitted light photomicrographs and BSE imagery, by filtering
260 images based on colour or greyscale characteristics.
261 *In-situ* major element analyses were obtained by EPMA using a JEOL JXA 8230
262 system at Victoria University of Wellington (VUW), or using a CAMECA SX100 at
263 Edinburgh University, both using wavelength-dispersive spectrometry. Operating conditions
264 varied depending on the phases and elements analysed, but precision of standard analyses of

major elements (>1 wt.% concentration) were always within 2 relative % (2 s.d.); with slightly higher uncertainties for minor elements (see Electronic Appendix 1 for further details on accuracy and precision of secondary standards). Due to their hydrous nature, only glass analyses with totals of <93 wt.% were set aside; values for the remaining analyses were then normalised to 100 %.

Trace element analyses of crystal phases and matrix glass were carried out at the University of Durham using a New Wave deep UV laser (193 nm solid state) coupled to an X-series 2 ICPMS (inductively-coupled plasma mass spectrometer). Analyses were run using a 35 μm spot (for glass) or 50 μm spot (for crystals). The LA-ICPMS data were internally normalized to ^{29}Si or ^{43}Ca from EPMA analyses. Abundances of single trace elements were calculated relative to a bracketing standard (NIST 612) which was analysed throughout the run under identical conditions. Precision and accuracies varied depending on the analytical conditions but generally have <10% (2 s.d.) uncertainties (see Electronic Appendix 1 for full details of precision and accuracy).

RESULTS

Whole rock data

The whole rock data confirm that the samples typify the full range in magmatic compositions exposed on Ascension Island, from the least-evolved Green Mountain scoria sample (AI14-552; 47.7 wt.% SiO_2, 3.01 wt.% Total Alkalis [TA]) through to the most-evolved sample of 1094 kyr-old (AI-94; Jicha et al., 2013) felsic lava (72.3 wt.% SiO_2, 10.3 wt.% TA; Fig. 3a, Table 2). When selected whole rock trace element data are normalised to primitive mantle (Palme & O'Neill, 2003) felsic lava and pumice samples are clearly depleted in Sr, Ti and Ba relative to mafic lava and scoria samples (Fig. 3b). Felsic pumice and lavas are generally more enriched in incompatible trace elements than the mafic lavas and scorias (Fig. 3b).

290 The whole rock data show increasing total alkalis, and decreasing CaO and MgO,
291 with increasing SiO_2 (Fig. 4). Mafic lavas are typically more-enriched in MgO, CaO and
292 TiO_2 (Fig. 4a, c), and depleted in FeO, Na_2O, K_2O, Zr and Ba (Fig. 4b, d, f, Table 3), relative
293 to felsic lavas. While having the textural characteristics of basaltic volcanism, samples of
294 Letterbox 'mafic' lavas are in fact intermediate, with 55.8 – 57.6 wt.% SiO_2, and 2.10 – 2.29
295 wt. % MgO. Pumice and felsic lava samples have similar major and trace element
296 concentrations (Fig. 3, 4), as do mafic lavas and scorias (Fig. 3, 4); thus there is no
297 appreciable difference in whole rock compositions between magmas erupted effusively or
298 explosively (Fig. 3, 4). Whilst there appear to be gaps within the MgO content (Fig. 4), these
299 solely reflect the samples selected for study, when compared with a large published data set
300 no gaps in composition are observed for Ascension Island volcanics (Fig.2c; Fig. 4 grey
301 fields).
302
303 **Petrology of Ascension lavas**
304 Mafic and intermediate lavas studied are generally crystal poor, with less than 5%
305 phenocrysts, apart from the samples from the South Coast (high Zr/Nb) lava with 18% and
306 40% phenocrysts in the two samples studied here (see Table 3, Fig. 5a, b). In the mafic and
307 intermediate lava flows, phenocrysts (> 500 μm) are predominantly plagioclase feldspar (Fig.
308 5c, d), with minor olivine in some samples (Table 3, Fig. 5). Phenocryst phases in the crystal
309 rich lavas (from the South Coast) are larger, up to 5mm, modal size 3mm, when compared
310 with all other mafic and intermediate phases, where phenocrysts are generally < 1mm in
311 diameter. The groundmass of all mafic and intermediate lavas studied here is
312 microcrystalline, with no glass present. The groundmass consists of plagioclase feldspar,
313 clinopyroxene, olivine and Fe-Ti oxides (Fig. 5a-d, Fig. 6) in decreasing order of abundance.

Felsic lava samples come from the (older) central felsic complex (AI14-103, AI15-621, AI-94; Fig. 1) and the (younger) eastern felsic complex (AI14-511, AI14-485, AI14-419, AI14-428). All felsic lavas are crystal poor, with <6% phenocrysts visible in hand sample (Table 3). Phenocrysts phases are dominantly ternary feldspars (plagioclase to alkali-feldspars, Fig. 7), with minor Fe-Ti oxides and aegirine-augite present as phenocrysts phases in two samples (Table 3). Phenocrysts are always <3 mm diameter. In thin section, crystals are largely euhedral, and feldspar crystals often present as clots of 2-5 crystals (Fig. 5e-h; Fig. 6d, e). The groundmass is usually microcrystalline, consisting of ternary feldspar, cristobalite, interstitial aegirine-augite and Fe-Ti oxides in decreasing order of abundance (Table 3; Fig. 6d, e, f). A single felsic lava sample has a glassy matrix (AI14-419, the Letterbox felsic lava sample), which has SiO_2 concentrations between 71.2 and 74.0 wt.% (Table 3; Fig. 11).

Mineral compositions of the mafic and intermediate lavas

Plagioclase feldspar is a dominant mineral phase in all mafic and intermediate lavas with compositions varying between $An_{37}Ab_{61}Or_2$ and An_{82} Ab_{17} Or_1 (Fig. 7). BSE images of feldspar crystals typically show faint oscillatory zoning (Fig. 6c) with the South Coast (high Zr/Nb) lavas having better developed zonation and resorbed cores (Fig. 6a, b). The lack of well-developed BSE image zonation patterns in the Sisters, Wideawakes and Letterbox feldspars (mafic lava fields, see Fig. 1 for name origins) is reflected in their major and trace element compositions which show limited variations (Fig. 7, 8). The South Coast lavas exhibit some compositional variation between core and rims in their feldspar population (Fig. 8c, 9a), with cores typically being less-evolved than feldspar rims. Olivine compositions in the groundmass (or as phenocrysts in South Coast and Wideawakes samples) vary between Fo49 – Fo89. Where groundmass olivine can be identified separately to phenocrysts, groundmass olivines have higher CaO and lower MnO concentrations at any given value of

Fo number. Olivine crystals are faintly normally-zoned, if they are zoned at all, with no evidence for resorbed cores in any samples studied (Fig. 6a, b, 9b, 10).

No variation is seen in phenocryst compositions between the stratigraphically older and younger samples from the same geographic regions. However, some variation in mineral compositions exists between different geographic regions, with differences in major and trace elements between geographic regions (Fig. 8a, c). Letterbox samples have more restricted feldspar and olivine compositions, representing the more-evolved end of the range in mineral compositions displayed by all mafic lavas (Fo 56 – 69; An 36 – 47; Fig. 8a; Figs. 9, 10a, 10c), consistent with their whole rock compositions (see Table 2). South Coast, Sisters and Wideawakes lavas generally contain more variable An-plagioclase (An 32 – 82; see Table 5, Fig. 1, 8, 9), which has lower Sr concentrations (and extends to higher anorthite contents; Fig. 8a, c), and more variable olivine (that extends to less-evolved compositions) than Letterbox (Fo49 – Fo89; Table 5, Fig. 1, 9, 10), consistent with their less evolved whole rock compositions.

Mineral compositions of the felsic lavas

Ternary feldspar is the dominant mineral phase in all felsic lavas with compositions varying between $An_{20}Ab_{75}Or_5$ and $Ab_{70}Or_{30}$ (Fig. 7). BSE images of feldspar crystals from felsic lava samples are unzoned (Fig. 6d, e). However, some lava flows show core-rim-groundmass variations in feldspar compositions (see Fig. 8c and Electronic Appendix 2), which is unresolvable in BSE images alone. In particular, sample AI14-485 (from the eastern felsic complex; Fig. 1) has systematically more-evolved rims than cores, and more-evolved groundmass than rims. Feldspar compositions of felsic lavas range from andesine ($An_{20}Ab_{75}Or_5$) through to anorthoclase ($Ab_{70}Or_{30}$; Fig. 7, Table 4), with the most-evolved compositions ($Ab_{70}Or_{30}$) present in both the older and younger felsic samples (see Fig. 8b;

364 Electronic Appendix 2). Most felsic feldspars (that are ternary) define a separate trend to the
365 mafic and intermediate lava samples (with plagioclase feldspar only), having higher
366 concentrations of Eu and Ba at any given Sr concentration. (Fig. 8d). Aegirine-augite is
367 present as a groundmass phase in all felsic lava samples studied here, with compositions
368 between 0.5 – 12.1 wt.% Na_2O and 0.1 – 6.2 wt.% MgO. Aegirine-augite, typically < 500 μm
369 (Fig. 11), commonly contains Fe-Ti oxide inclusions, and has higher Mn and lower Sr
370 concentrations than the intermediate lavas (Fig. 11c), whilst the minor olivine (< 1%), present
371 only in the Letterbox felsic lava, is Fo12.5 (see Electronic Appendix 2).
372 The crystal compositions between samples of felsic lavas and samples of mafic to
373 intermediate lavas do not overlap in their major elements. The samples from the younger
374 eastern felsic complex (Fig. 1) have the greatest range in both feldspar ($An_{20}Ab_{75}Or_5$ –
375 $Ab_{70}Or_{30}$) and clinopyroxene compositions (0.5 – 12.2 wt.% Na_2O; Fig. 8b, 11a, b, Table 5,
376 7), while crystals within samples from the central felsic complex are typically more-evolved;
377 containing anorthoclase feldspar ($An_7Ab_{73}Or_{20}$ – $Ab_{70}Or_{30}$) and more aegirine-rich
378 clinopyroxene (2.9 – 9.0 wt.% Na_2O; Fig. 11a, b; Table 7).
379
380 **Petrological variation in mafic pyroclastic deposits**
381 Pyroclastic deposits are exposed all across the island and have compositions ranging from
382 basalt to rhyolite, with no obvious Daly Gap when all published samples are considered
383 (Daly, 1925, Fig. 3, 4). The scoriaceous deposits studied here are crystal poor, with
384 phenocrysts of plagioclase feldspar and minor olivine, clinopyroxene and Fe-Ti oxides. The
385 Green Mountain scoria (AI14-552) is a relatively voluminous eruption, with widespread
386 deposits originating from within the central felsic complex. Its key identifying feature is the
387 presence of abundant white-cream plutonic lithic clasts. In thin section, juvenile scoria
388 typically contains plagioclase feldspar + olivine ± clinopyroxene ± Fe-Ti oxides. The

groundmasses of the scoria clasts from these deposits have varying proportions of microlites (feldspar + olivine).

In BSE imagery, crystal phases are not zoned, and preserve euhedral crystal habits. Feldspar compositions overlap those of both the mafic and felsic lavas, ranging between $An_{14}Ab_{72}Or_{14}$ and $An_{84}Ab_{15}Or_{1}$. The Green Mountain scoria has the largest variation in feldspar compositions (AI14-552; Table 5), but there are no systematic differences in core and rim compositions of individual crystals (Fig. 8c, Table 5). Olivine, the other major phenocrystic phase, overlaps compositionally with olivine in the mafic lavas, with Fo74 to Fo87 (Fig. 9b, 10b; Table 6) and also has no systematic difference in core and rim compositions from individual olivines (Fig. 10c). Matrix glass compositions are typical of mafic melts, with low SiO_2 (< 50 wt.%) and high CaO (> 6 wt.%), (Fig. 12, Table 8); the bulk scoria composition is slightly less-evolved (45.8 – 49.3 wt.% SiO_2) than the NE Bay scoria (AI14-438, 49.0 – 52.4 wt.% SiO_2).

Petrological variation in felsic pyroclastic deposits

Pumice clasts are typically crystal poor, with < 5% crystals. Ternary feldspar is the dominant crystal phase (oligoclase to anorthoclase composition ± sanidine) with one ferromagnesian phase of either amphibole or fayalitic olivine, with minor magnetite ± ilmenite ± apatite, and rarely augitic clinopyroxene is present. One exception to this is the intermediate sample AI14-459 which has ~15% crystals, with large amphibole (up to 3 mm) phenocrysts. Crystal phases are not zoned in BSE, and preserve euhedral crystal habits. Groundmass is typically glassy, with varying amount of feldspar microlites.

Feldspar compositions from these pumice fall deposits intersect and straddle those from the evolved effusive eruptions (Fig. 7, Table 4): with compositions ranging between $An_{51}Ab_{47}Or_{2}$ and $An_{0.5}Ab_{58.5}Or_{41}$. Some eruptions have relatively restricted feldspar

compositions (e.g. AI14-488: $An_{0.5}Ab_{65.5}Or_{34}$ – $An_{1}Ab_{69}Or_{30}$) whereas other extend over wide ranges (e.g. AI14-435: $An_{2}Ab_{73}Or_{25}$ – $An_{18}Ab_{76}Or_{6}$). In trace elements, the felsic pyroclastic feldspars plot within the higher- and lower-Eu trend (Fig. 8d). No clear core-rim relationships were found in feldspar compositions: only one pumice fall deposit in Middleton's Valley (AI14-459) has slightly less-evolved cores relative to rim compositions (cores: $An_{51}Ab_{47}Or_{2}$ – $An_{20}Ab_{74}Or_{6}$; rims $An_{43}Ab_{54}Or_{2}$ – $An_{20}Ab_{74}Or_{6}$). This comparatively crystal-rich sample (see Table 3) also bridges the divide between our felsic and mafic lava feldspar populations. Fosterite content in olivines (Fo1 – 57) from felsic pyroclastic samples mirrors the relationships between pyroclastic and effusive lava feldspars- intersecting with and extending the range in compositions of mafic lava sourced olivines (Fig. 10b, Table 6). Again, no differences between core and rim compositions are observed in olivine from all pyroclastic samples (Fig. 10c).

Glass compositions of felsic pyroclastic deposits range from ~ 66 wt.% to 75 wt.% SiO_2 (Fig. 12; Table 8). All sampled pyroclastic deposits have relatively homogenous glass compositions, with the one exception being the glass from the compositionally-zoned fall deposit, previously described in Chamberlain et al. (2016; Fig. 12a). In detail, individual sample variation in trace elements shows up to a four-fold variation in elements compatible in feldspar (Ba, Sr; Fig. 12b). However, limited variations in source-related trace elements (such as Th/U ratio; Fig. 12c) are evident between samples, where variation within a single sample is of the same magnitude or greater than variations between samples.

Intensive variables

Where available, two co-existing oxides (magnetite and ilmenite) were analysed and Fe-Ti oxide thermometry of Ghiorso & Evans (2008) was applied (if the pairs passed the equilibrium test of Bacon & Hirschman, 1988). Iron-titanium oxide derived temperatures

range from 932 °C to 1037 °C for the mafic lavas (Table 8). Oxygen fugacity varies between –0.45 log units relative to the Nickel-Nickel Oxide (Δ NNO) buffer to +0.05 log units Δ NNO. Felsic lavas and pyroclastic samples yield Fe-Ti oxide temperatures ranging from 850 °C to 960 °C, and fO_2 ranging from –0.5 log units Δ NNO to –2.3 log units Δ NNO (Table 8).

Plagioclase-melt thermometry (Putirka, 2008) and alkali feldspar-melt thermometry (Putirka, 2008) was applied to all samples where equilibrium between feldspars and melt could be established (Putirka, 2008). Pressures of 330 MPa were assumed for mafic samples, as this is consistent with equilibration at the base of the crust, (Klingelhöfer et al., 2001) and pressures of 250 MPa were used for felsic samples, based on melt inclusion entrapment pressures modelled from samples of a zoned fall deposit on Ascension Island (Chamberlain et al., 2016). This modelling yielded temperatures within a similar range (but often higher) to that of the Fe-Ti oxide thermometry (Table 8) with modelled temperatures ranging between 772 °C and 1034 °C for felsic samples, and between 1093°C and 1174 °C for mafic samples (Table 8). Although a specific pressure was assumed, testing demonstrated that the pressure effect is minimal, with less than 10 °C variation in estimated temperatures with > 200 MPa variation in assumed pressures.

Using measured alkali feldspar-melt compositions and temperatures modelled from plagioclase-melt thermometry, the alkali feldspar-melt hygrometer of Mollo et al. (2015) was also applied (see Table 8 for summarised results, full results in Electronic Appendix 2). Calculated water concentrations are high (average concentrations for the felsic units between 4.66 wt.% and 8.12 wt.%, Table 8). Modelled water contents associated with the felsic lava and dome samples have consistently lower water concentrations than the explosively erupted samples. These high concentrations of water in explosive felsic samples are similar to those measured in Ascension Island melt inclusions (Chamberlain et al., 2016) and with the high

463 loss on ignition from felsic pyroclastic samples measured during XRF analyses (see
464 Electronic Appendix 2 for full XRF results).
465
466 **DISCUSSION**
467 **Origin of compositional variations in Ascension Island magmas**
468 A range in whole rock and crystal compositions are evident in Ascension Island samples,
469 with no clear differences observed between effusively erupted lava samples and explosively
470 erupted pumice and scoria samples (Fig. 4, 7a). When considered alone, the variations in
471 whole rock chemistry presented here (Fig. 4) do not give reason to disagree with previous
472 whole rock studies of Ascension Island, which have suggested that fractional crystallisation is
473 the dominant mechanism for producing evolved melts (e.g. Harris, 1983; Kar et al., 1998;
474 Jicha et al., 2013; Chamberlain et al., 2016), evidenced by the continuous trend in major and
475 trace element concentrations (Figs. 3, 4; Weaver et al., 1996; Kar et al., 1998; Jicha et al.,
476 2013), and the lack of whole rock radiogenic isotopic ratio variation with major element
477 concentrations (Fig. 2d; Weaver et al., 1996; Kar et al., 1998; Paulick et al., 2010).
478 Partial melting of mafic material is another process through which felsic melts have
479 been proposed to be generated at ocean island volcanoes (e.g. Borhson & Reid, 1997;
480 Sverrisdottir, 2007; Carley et al., 2011; Kuritani et al., 2011). Unlike other ocean islands,
481 there is no evidence for divergence in Nd isotopic ratios between mafic and felsic melts (Kar
482 et al., 1998), and major and trace elements vary co-linearly (Fig. 2b; Kar et al., 1998; Jicha et
483 al., 2013) which previous studies suggest is not supportive of a partial melting origin for
484 evolved melts at Ascension. Some minor assimilation and contamination has been inferred to
485 be partly responsible for the radiogenic Sr isotopic compositions of more felsic melts (Kar et
486 al., 1998), but this cannot be quantified based on the new data presented here, and it is noted
487 that none of the earlier isotopic data was acid leached prior to analysis (cf. Davidson et al.,

1997). At other volcanic systems where partial melting has been shown to be a significant driver for the production of evolved magmas, magmatic compositions can be bimodal, with few erupted magmas of intermediate composition (e.g. Charlier et al., 2013, Meade et al., 2014), which is not observed at Ascension (Fig. 3, 4). However, small degree direct partial melting of a seawater-altered basaltic/gabbroic parent cannot be ruled out with our new data set for Ascension (cf. Kar et al., 1998), and may be responsible for some of the variation in $^{87}Sr/^{86}Sr$ isotopic ratios (Fig. 2a).

Magma mixing between mafic and felsic magmas to produce the intermediate rocks could be responsible for the continuum in whole rock compositions at Ascension (Fig. 3), yet non-linear variations in major and trace elements in both whole rock compositions (especially in TiO_2, K_2O and Zr, Fig. 4) and crystal phases (Fig. 8d, 10d) suggest that this is unlikely. Similarly, crystal compositions form coherent trends within individual samples, with no evidence for the distinct populations (cf. Geist et al., 1995; Troll & Schminke, 2002; Fig. 8 – 11) that could represent growth in different magmas. Petrographic data shows no evidence of magma mixing, therefore fractional crystallisation is hypothesised to be the main mechanism for generation of felsic melts at Ascension Island, in agreement with previous authors (cf. Kar et al., 1998; Jicha et al., 2013).

To test the fractional crystallisation hypothesis further, MELTS modelling of isobaric liquid lines of descent (Gualda & Ghiorso, 2015) from the least evolved sample (AI14-438, see Table 1) has been undertaken at a range of pressures, from 330 MPa (the base of the crust, Klingelhöfer et al., 2001) to 90 MPa (~ 3.5 km depth), as well as an isothermal decompression model from 90 MPa to 1MPa (Fig. 13, 14). An initial starting composition from AI14-438 was used, with an assumed water concentration of 0.5 wt.% H_2O, and fO_2 at the NNO-buffer based on Fe-Ti oxide thermometry (Table 8) and analyses of nearby MAR glasses (Almeev et al., 2008) which tap a mixed enriched Ascension Island-type source and a

depleted high εHf mantle (Paulick et al., 2010). It has been shown that oxygen fugacity is not solely fractionation dependent at Ascension Island (Chamberlain et al., 2016) and this one-step MELTS modelling does not properly reflect the fractionating phases at the more-evolved end. Thus, at T< 950 °C the composition of AI15-621 was used, the least-evolved of the felsic lava samples, with an assumed water concentration of (5.1 wt.% H_2O) from feldspar-melt hygrometry, and fO_2 -1.5 ΔNNO from Fe-Ti oxide thermometry (Table 8).

The modelled liquid lines of descent of this two-step MELTS modelling reproduce the observed variations in whole rock composition (Fig. 13), with the models run at higher pressure (250 MPa or greater) having a better fit for MgO and CaO concentrations (Fig. 13b, c), suggesting fractionation at depths of more than 7 km. At the more evolved compositions (>68 wt.% SiO_2), fractionation at 170 MPa better reproduces the more evolved compositions of Ascension Island magmas (Fig. 13a). Whilst isobaric fractionation is unlikely to occur at Ascension Island, the MELTS modelling shows that simple fractional crystallisation can replicate the observed variations in whole rock composition, when oxygen fugacity can be controlled to represent that measured in Ascension Island magmas. Similarly, modelled increases in H_2O with increasing SiO_2 support the modelled high melt H_2O concentrations from feldspar-melt hygrometry (Table 8), especially at higher pressures of evolution (Fig. 13d).

Fractional crystallisation in mafic and intermediate magmas

Fractional crystallisation, as modelled by MELTS, has demonstrated that the observed whole rock compositional range within the Ascension Island magmatic suite can be reproduced in this process. For the mafic and intermediate magmas, the crystal compositions measured overlap well with the modelled crystallising phases from MELTS (Fig. 14), and up to 70% total fractionation has occurred to produce the most evolved intermediate magmas (Fig. 13).

538 Whilst MELTS details proportions of phases fractionating, previous studies have
539 demonstrated some limitations on the model's ability to accurately predict crystallisation of
540 water-bearing phases (Gualda et al., 2012), clinopyroxene (Fowler & Spera, 2010) and apatite
541 (Rooney et al., 2012). Therefore, to yield further insights into proportions of phases
542 crystallising least-squares modelling of the major elements has been undertaken, constrained
543 by using only phases observed in samples of Ascension Island volcanics.
544 Major element least-squares modelling was carried out using Petrograph (Petrelli et
545 al., 2005, built on the least-squares modelling of Stormer & Nicholls, 1978), and to include
546 entrainment where appropriate (cf. Kar et al., 1998, Electronic Appendix 3). A comparison of
547 phases crystallising at each modelled stage between MELTS and Petrograph can be seen in
548 Electonic Appendix 3. Two stages of evolution are considered initially, to attempt to
549 reproduce the variations in mafic to intermediate whole rock compositions (Fig. 3): Stage 1)
550 from the NE Bay Scoria (the most primitive basalt; AI14-438) to the Wideawakes (an
551 intermediate Zr/Nb basalt marking the inflection in MgO vs TiO_2, Fig 4c; AI-445); Stage 2)
552 Wideawakes (AI14-445) to Letterbox (the intermediate lava; AI14-423). In both stages,
553 compositions of plagioclase feldspar, olivine, clinopyroxene, ilmenite and magnetite
554 measured in the parent sample were used. Apatite was also used as an accessory phase, given
555 its presence as inclusions in mineral phases and the variation in P_2O_5 evident in whole rock
556 data (Table 2; full details of modelling conditions see Electronic Appendix 3). Whilst this
557 modelling is limited by the assumption of uniform compositions of the fractionating phases,
558 and has no pressure or temperature dependence, it provides a first order constraint on modal
559 fractionating assemblage provided the sum of the squared residuals is < 2 (Stormer &
560 Nicholls, 1978). Stage 1 fractionation modelling (sum of squared residuals [SSR] 0.25)
561 suggests that ~ 8% fractionation of an assemblage dominated by plagioclase feldspar with
562 subordinate olivine and apatite, coupled with the minor entrainment (4%) of clinopyroxene

563 and two oxides could produce the compositions of AI-445. The second stage of modelling
564 (SSR 0.05), to produce the intermediate Letterbox magmas, suggests a further 56%
565 fractionation (0.4 melt fraction remaining) of an assemblage dominated by feldspar and
566 clinopyroxene, with minor olivine, magnetite, ilmenite and apatite (See Electronic Appendix
567 3 for graphic representation; and comparison with modelled MELTS fractionating phases).
568 These modelled fractionating assemblages have been further tested using published
569 distribution coefficients for Rb, Sr, Y, Zr, Nb and Ba in the fractionating phases (Fig. 15, full
570 details and references for the distribution coefficients used is given in Electronic Appendix
571 3). Generally fractional crystallisation (excluding any accumulation) can reproduce observed
572 variations in Rb, Nb, Ba and Zr, with a poorer agreement with Sr and Y data (Fig. 15 and
573 Electronic Appendix 3) for the variation observed in mafic magmas.
574
575 *Felsic magma evolution*
576 Felsic magma evolution through closed system fractional crystallisation, modelled by
577 MELTS, is shown to reproduce well the major elements of the whole rock data for Ascension
578 in most elements (Fig. 13), and pressure of fractionation has a significant effect on total
579 alkalis (Fig. 13a) reflecting the pressure-sensitivity of feldspar crystallisation (Fig. 14a).
580 Fractionating assemblages again reproduce well the measured compositions of feldspar,
581 olivine and clinopyroxene. In the more-evolved lavas, growth of low-pressure phases
582 (evidenced by feldspars with ~4 – 6 wt.% K_2O and Na-rich clinopyroxenes, Fig. 14a, c)
583 reflect growth at a range of pressures (cf. isothermal decompression crystal compositions
584 from MELTS modelling; Fig. 14) which are not observed in equivalent explosive deposits.
585 Again, to supplement the MELTS modelling, major element least-squares modelling
586 was carried out using Petrograph (Petrelli et al., 2005; from Stormer & Nicholls, 1978). Two
587 further stages of evolution are considered, to attempt to reproduce the trends observed in

588 whole rock concentrations (Fig. 3): Stage 3) Letterbox (AI14-423) to Devils Riding School
589 (representative of the trachytic lavas on Ascension, Fig 3; AI15-621) and Stage 4) Devils
590 Riding School (AI15-621) to Middleton's Ridge (most-evolved rhyolite, AI-94). In both
591 stages, compositions of feldspars (plagioclase and ternary feldspar), olivine, clinopyroxene,
592 ilmenite and magnetite measured in the parent sample were used. Apatite was also used as an
593 accessory phase, given its presence as inclusions in mineral phases and the variation in P_2O_5
594 evident in whole rock data (Table 2; full details of modelling conditions see Electronic
595 Appendix 3).

596 Stage 3 (SSR 1.23) requires a further 60% fractionation (0.16 melt fraction remaining
597 from initial mafic starting sample) of an assemblage again dominated by plagioclase feldspar,
598 with subordinate clinopyroxene, apatite, ilmenite, and minor entrainment of magnetite (1%).
599 Contrastingly, MELTS modelling suggests both biotite and orthopyroxene should begin to
600 fractionate (neither of which have been observed on Ascension Island, Electronic Appendix
601 3). Stage 4 (SSR 0.08) shows a clear change in fractionating assemblage with ternary feldspar
602 dominating the fractionating assemblage with clinopyroxene and magnetite, and requiring a
603 further 57% fractionation (0.07 melt fraction remaining, in agreement with MELTS
604 modelling of liquid lines of descent: 0.06 melt fraction remaining, Fig. 13). Minor
605 accumulation (4%) of fayalite, ilmenite and apatite contributes to the evolution of the felsic
606 magmas (see Electronic Appendix 3). These inferred fractionating phases are in good
607 agreement with the observed crystal phases present in Ascension samples with feldspar being
608 the dominant crystal phase present, with minor fayalitic olivine or clinopyroxene present,
609 unlike MELTS modelling which again fails to accurately reproduce the observed mineral
610 phases, with the suggested presence of leucite and orthopyroxene (Table 3, Electronic
611 Appendix 3).

612 Trace element modelling of the proposed fractionating assemblages was undertaken
613 for stages 3 and 4, again excluding any accumulation of phases. The results of this modelling
614 show that Ba is successfully modelled by this fractionating assemblage, with moderate but
615 less consistent results for modelled vs. measured Sr and Nb (Fig. 15, Electronic Appendix 3).
616 There is poor agreement between modelled and measured Zr, Rb and Y (Fig. 15, Electronic
617 Appendix 3). Zircon is observed in the most evolved samples, but fractionation of this phase
618 has not been modelled as the proportions are challenging to quantify using major element
619 modelling, although it could be the cause of the variations between observed and modelled
620 concentrations of Zr and Y in the felsic magmas of Ascension. We note that accumulation or
621 fractionation of minor phases, whilst not significant in terms of the major element evolution
622 of the felsic melts, can significantly affect the trace element compositions of melts. With a K_d
623 of ~ 40 in rhyolitic apatites (Pearce & Norry, 1979), Y concentrations will be significantly
624 affected by even minor amounts of fractionation of this phase.
625
626 *The role of ascent rate and oxygen fugacity*
627 Use of MELTS modelling to yield crystal compositions has highlighted the role of crystal
628 growth in the upper crust during ascent in the presence or absence of phases in the felsic
629 magmas. Moderate 4 – 6 wt.% K_2O feldspar and aegirine-augite are only found in felsic
630 lavas; in felsic pyroclastic samples no feldspar has 4 – 6 wt.% K_2O and fayalite is the
631 common 'mafic' phase (Fig. 10b)- rare clinopyroxene is augitic in composition, and reflects
632 fractionation at pressures ≥ 90 MPa (Fig. 14c). Pyroclastic samples have high modelled water
633 concentrations (Table 8) perhaps reflective of higher pressure storage (Fig. 13d, cf. Di Matteo
634 et al., 2004; Brenna et al., 2014). Combining the lack of chemical zonation (Figs 9c, 10c), the
635 euhedral nature of the phenocryst phases (Fig, 6), and no low-P phases forming (cf. Fig. 14c),

636 ascent rates for pyroclastic magmas, fractionating at high pressures (≥ 250 MPa, c.f. Fig. 13)
637 is likely to be rapid and warrants further comparison with their effusive counterparts.
638 In other alkaline systems it has been shown that variations in fO_2 at constant
639 temperatures can result in variable phase assemblages (White et al., 2009; Markl et al., 2010).
640 Given the large variation in calculated fO_2 within Ascension Island magmas (Table 8), some
641 of the small variation around liquid lines of descent, and mismatch between the MELTS-
642 modelled vs. observed phases, may stem from variable phase crystallisation at differing fO_2
643 conditions, as well as variations in ascent rate and depth to storage regions within the lower
644 crust.
645
646 **Spatial and temporal variations in magmatism at Ascension Island**
647 *Temporal and spatial variation of mafic magmas*
648 Whole rock major and trace element data and crystal compositions show little variation
649 between samples of older and younger lavas (Table 2, Fig. 4) from the same eruptive centres,
650 suggesting that the mode of mafic magma generation and ascent has been relatively constant
651 for the subaerial (and exposed) history of Ascension Island. This is in agreement with
652 previous whole rock isotopic data, which shows no clear variation in the subaerial edifice of
653 Sr, Nd or Pb isotopic ratios over time, indicative of source characteristics (Weaver et al.,
654 1996; Kar, 1997; Paulick et al 2010; Jicha et al., 2013). While there is no temporal variation
655 in the composition of mafic subaerial magmas erupted on Ascension, there are significant
656 spatial differences in the phenocryst percentages, whole rock compositions, and crystal
657 compositions, depending on the location of the eruptive centre (detailed in Table 1; Table 3,
658 Figs. 4, 8, 10). South Coast lavas have the highest crystal contents (>17 %) and the least-
659 evolved crystal compositions (down to An82, and Fo87; Fig 8, 10), whereas the Letterbox

samples from the SE of the island are intermediate in composition, contain clinopyroxene as a minor component (instead of olivine; Table 3), and more restricted feldspar compositions.

Origin of the crystal cargo

Given the marked differences in crystallinity between the South Coast lavas (AI14-522 and AI14-514; Table 1) and the other mafic to intermediate lavas (Table 3), modelling of plagioclase and olivine equilibrium compositions, based on the whole rock compositions at an assumed temperature and pressure, following the method of Price et al. (2012), was undertaken (Fig. 9). The range in olivine Mg# from different eruptive centres (Fig. 9) shows that not all of the olivine crystal cargo is modelled to be in equilibrium with the melt in which it is erupted (Fig. 9b). Rim analyses are just as likely to be in disequilibrium with the whole rock compositions as core analyses. This range in olivine Mg# shows that some crystals are not phenocrystic, despite the lack of significant overgrowths and the crystals mostly having a euhedral to subhedral habit (Fig. 6).

Similarly, plagioclase feldspar compositions are not in equilibrium with their whole rock compositions (Fig. 9a) and yet only feldspars from the South Coast lavas display reaction rims and anhedral cores (Fig. 6b). Whilst the calculation of equilibrium plagioclase compositions (following the method of Panjasawatwong et al., 1995) is only calibrated for plagioclase feldspar compositions (and not in alkaline systems such as Ascension), and thus could be a potential reason for why feldspars are in apparent disequilibrium, single samples preserve a wide variation in An content in the feldspars, showing that irrespective of the modelled equilibrium conditions, significant amounts of feldspar crystals will not be in equilibrium with their host rock composition.

Mafic lavas, excluding those from the South Coast group, are clearly in chemical disequilibrium with their feldspars, with less variation from the calculated equilibrium

685 composition for olivines (Fig. 9). Densities of the mafic magmas were calculated following
686 the method of Bottinga & Weill (1970), at pressure of 330 MPa (the base of the crust
687 (Klingelhöfer et al., 2001) using measured whole rock compositions and a water
688 concentration of 0.5 wt.%. Densities of mafic magmas are on the order of 2.7 g/cm^3,
689 remarkably similar to that of plagioclase feldspar (2.6 – 2.7 g/cm^3, Scoates, 2000; Ghiorso &
690 Gualda, 2015), yet less dense than olivine and clinopyroxene, (~3.6 g/cm^3 and ~3.2 g/cm^3
691 respectively, Scoates, 2000; Ghiorso & Gualda, 2015). Thus, fractionating feldspar in a zone
692 of magma storage will not sink, and instead may form lateral mushy cumulates as the magma
693 evolves, whereas olivine and clinopyroxene have bigger density differences with the mafic
694 magmas, and thus can sink more effectively. As the mafic magma reaches eruptible
695 conditions, either due to concentration of volatiles within the magma (e.g. Stock et al., 2016),
696 tectonic destabilisation of the system (e.g. Allan et al., 2012) or through gas injection (e.g.
697 Caricchi et al., 2018), the mafic magma rapidly incorporates these lateral mushy feldspar
698 antecrysts, producing the wide range in feldspar compositions found within single eruptions,
699 that are in disequilibrium with their whole rock composition, yet native to the magmatic
700 system (Fig. 9a, 14a). The timescale of incorporation of these antecrystic crystals prior to
701 eruption must be short, as no zonation is observed (see Figs. 8 – 10), and feldspars generally
702 retain their euhedral appearance (Figs. 5, 6). Similarly, the mushy storage regions in which
703 the feldspars and mafic phases are forming are transient; no evidence is preserved for long-
704 lived melt-dominant magma storage regions for mafic to intermediate magmas, with no
705 evidence for incorporated crystals seeing more than one 'triggering' event (cf. Kahl et al.,
706 2013).
707 *Role of crystal entrainment in mafic to intermediate magma genesis:* Excluding the
708 South Coast group lavas, all other mafic and intermediate lavas have crystallinities less than
709 5% (Table 3), with limited evidence for chemical zonation (Fig. 10c) and euhedral crystal

habits (Fig. 4, 6), thus incorporation of mushy antecrysts (which are subsequently resorbed) appears unlikely to constitute more than 5% (total rock crystallinity) of the rock volume. The similarities in antecrystic and phenocrystic crystal cargo in Ascension Island lavas make assessing the proportions of assimilated material challenging, as incorporation of these antecrysts may merely shift the whole rock compositions along the modelled liquid line of descent. This has implications for modelling the total amount of fractional crystallisation responsible for individual mafic and intermediate magmas, thus these estimates of degree of fractional crystallisation from both MELTS and the least-squares modelling must be treated with caution.

Lavas in the South Coast group have relatively high crystallinity compared with other mafic and intermediate lavas (Table 3), with crystals that show the most zoning in BSE imagery and major and trace element analyses (Fig. 6, 8), and feldspars that lie furthest from the modelled equilibrium compositions (Fig. 9). These South Coast lavas are also observed to contain significant proportions of plutonic lithic clasts (ranging from gabbros to syenites, Roedder & Coombs, 1967; Harris et al., 1982; Harris, 1983; Webster & Rebbert, 2001). These observations suggest that the range in compositions of feldspar and olivines found in South Coast lavas is the result of incorporation of large amounts crystals from other sources, as antecrysts or xenocrysts (Charlier et al., 2005). Potential sources of contaminant crystals are oceanic crust (thus crystals are xenocrystic), plutonic bodies related to Ascension Island magmatism (thus antecrysts), or from a mushy, not yet solid fractionated crystal residue (also antecrysts, as in the other mafic to intermediate lavas, above). Few analyses of crystals from the abundant lithic clasts exist, however feldspar compositions from gabbros overlap those found in the mafic lavas (Harris, 1983) and isotopic data suggests a cogenetic origin for gabbros and mafic lavas (Weis et al., 1987). Contrastingly, ocean crust feldspars define a lower K_2O trend than alkaline-magmatism-sourced feldspars when plotted against An content

735 (Davis et al., 2007). No difference is seen in the feldspar and olivine compositions of the
736 South Coast lavas (Fig. 7 – 10), suggesting that incorporated crystals are antecrystic (and not
737 xenocrystic, see representative compositions of Mid-Atlantic Ridge feldspar crystals on Fig.
738 8b) in origin. No evidence is seen in crystal compositions or textures for mixing with a
739 chemically distinct magma, thus mechanical incorporation of antecrystic plutonic material
740 (e.g. Humphreys et al., 2009) is our favoured method by which these materials are included
741 within the South Coast lavas, on top of the 'background' accumulation of mushy antecrystic
742 material similar to the other mafic and intermediate lavas.
743 South coast lavas are the only samples studied here which show overgrowths on
744 feldspars (Fig. 6b), glomerocrystic textures (Fig. 5b) and increased crystallinity, suggestive of
745 higher degrees of antecryst incorporation. The relative importance of antecrysts in south coast
746 lavas could be due to these south coast magmas having a greater ability to erode these deep
747 mafic plutonic bodies upon ascent, or that that these deep mafic plutonic bodies are only
748 present in the source and ascent region of the crust through which the south coast lavas travel
749 prior to eruption. A magma's ability to mechanically disaggregate any lithic fragment is
750 dependent upon its enthalpy and composition (Glazner, 2007). The variations in whole rock
751 compositions between south coast lavas and other mafic lavas is not significant (Fig. 4), thus
752 only variations in temperature could change the magmas ability to erode and disaggregate the
753 plutonic lithic fragment. Modelled feldspar-melt temperatures are similar across the suite of
754 mafic lavas (Table 8) and so it seems unlikely that increased antecryst incorporation is due to
755 an increased ability of south coast magmas to erode plutonic lithic fragments. Instead, the
756 increased proportion of antecrysts in south coast lavas is suggested to reflect an increased
757 presence of mafic plutonic rocks at depth in this region. These plutonic rocks are anteliths,
758 related to Ascension Island generation and not oceanic crust plutonic rocks (Fig. 8b), and

highlight the lateral variability in plutonic or mushy regions within the Ascension Island crust.

Crustal control on the location of felsic eruptive centres

Eruptions of felsic magma occurred from two main centres: the older central felsic complex, and the younger eastern felsic complex with mafic magmas erupted around the peripheries of these centres (Fig. 1; Jicha et al., 2013). In these regions, felsic magmas - erupted as lavas and pyroclasts - are the dominant magma type. Spatial separation of mafic and felsic lavas has been seen at other ocean islands (both active and extinct), and has been suggested to be a result of crustal structure inhibiting the ascent of more dense mafic magmas in the felsic complexes (e.g. Mahood & Hildreth, 1983; Druitt et al., 1995; Carracedo et al., 2007; Brenna et al., 2015).

Active-source tomography reveals an area of elevated seismic velocities in the core of the island, at 6.5 km depth beneath the felsic complexes (Evangelidis et al., 2004). This was interpreted to represent a single crystallised magma body, supported by the presence of plutonic lithic clasts in the erupted products (e.g. Roedder & Coombs, 1967; Harris, 1986; Weis et al., 1987; Hobson, 2001; Webster & Rebbert, 2001). This central core of nested plutonic rocks (of gabbroic through to granitic compositions – Roedder & Coombs, 1967) under the felsic complexes could inhibit the ascent of almost all mafic magmas in these regions.

The presence of plutonic rocks in ocean island crust has long been known to affect the evolution of magmas prior to eruption—the volcanic islands of Terceira (Mungall & Martin, 1995) and Oki-Dōzen (Brenna et al., 2015), among others, have evidence for central felsic complexes (both as plutonic rocks, and as storage regions for felsic volcanic eruptions) which inhibit the eruption of mafic magmas. Ascension Island has a modelled growth rate of 0.4

784 km/Myr (Minshull et al., 2010), which is significantly lower even than post-shield Hawaii
785 (0.9 km/Myr, Minshull et al., 2010 and references therein) and dramatically lower than shield
786 stage Mauna Kea (8.6km/Myr, Minshull et al., 2010 and references therein). Therefore we
787 suggest that this 'filtering' of mafic magmas and spatial segregation of mafic and felsic
788 eruptive centres could be a result of low rates of magmatic flux. If magmatic flux is higher,
789 this could destabilise the central felsic systems, and mafic and felsic magmas would no
790 longer show such clear spatial separation, and mixing textures would be much more
791 dominant, such as those observed in Tenerife (Sliwinski et al., 2015) or Iceland (Carley et al.,
792 2011), where mafic and felsic magmas are still produced, but with less clear spatial
793 separation and increased role of partial melting of crustal material than that inferred at
794 Ascension.
795 We suggest that multiple plutonic bodies representative of multiple ephemeral magma
796 reservoirs, rather than a single magma body, are necessary to generate the range in
797 compositions seen on Ascension Island as there is no evidence from crystal compositions for
798 repeated use of a single magma storage region which is repeatedly rejuvenated (cf. Kahl et
799 al., 2013). This observation suggests the 'plutonic body' identified seismically (Evangelidis
800 et al., 2004) beneath Ascension is a series of smaller-volume, nested plutonic bodies which
801 cannot be resolved seismically from a single large body in the same dimensions (Bauer et al.,
802 2003).
803 The presence of plutonic lithic clasts in pyroclastic fall deposits on Ascension Island
804 (including some of the oldest fall units on the island, Hobson, 2001), combined with the
805 rhyolitic nature of the oldest-dated subaerial lava (Jicha et al., 2013), implies that the plutonic
806 complex was established well before the beginning of the subaerial phase of Ascension
807 Island's volcanic history. While the felsic plutonic and volcanic rocks share an apparently
808 common origin (with similar isotopic characteristics, Weis et al., 1987 and following the

same liquid line of descent, Harris et al., 1982) the timing of plutonic formation must pre-date the earliest subaerial eruptions on the island (1094 ka; Jicha et al., 2013), and could relate to the more voluminous submarine volcanism that began ~5 – 6 Myr ago (Minshull et al., 2010; Paulick et al., 2010).

The magmatic plumbing system

Here we combine our new results with all previously published data to present a model for the magmatic plumbing system underlying Ascension Island (Fig. 16) during the subaerial phase of activity from ~1 Ma to present. The key features of the model are as follows:

1) A zone of melt extraction from which all Ascension Island volcanism is sourced, at varying degrees of partial melt (Fig. 16; Paulick et al., 2010; Jicha et al., 2013). This melt extraction zone is geochemically distinct from the mantle melting responsible for the significantly larger volume submarine volcanism of Ascension which was active from ~5-6 Ma to ~3 Ma (Minshull et al., 2010; Paulick et al., 2010).
2) Heterogeneity in the lower crust affects the ascent and incorporation of antecrysts in basaltic melts. The variably over-thickened layer 3 (lower crust) presently underlying Ascension Island (Klingelhöfer et al., 2001) likely formed during the large volume, on-axis volcanism which built the submarine edifice (Minshull et al., 2010). We suggest that the over-thickening of layer 3 (represented mainly by mafic plutonic lithic clasts, not the nested felsic plutonic lithic clasts) is most significant underneath the vents for the South Coast lavas (AI14-514, AI14-522). South Coast lavas contain many crystals that are not in equilibrium with their whole rock compositions (Fig. 9), suggesting that these magmas have mechanically incorporated large numbers of antecrystic feldspar and olivine, shortly prior to eruption. This spatial heterogeneity in

deep mafic plutonic rocks is reflected in the proportions of antecrysts incorporated during ascent of mafic magmas.

3) A central nested region of small discrete plutonic bodies of varying composition (of a higher proportion of felsic bodies), which forces the majority of ascending mafic magmas to stall and fractionate until they reach a level where their buoyancy has increased enough to allow them to ascend further. This is supported by the felsic plutonic lithic clasts within the Green Mountain scoria, erupted in the central felsic complex, and by mechanically incorporated plutonic lithic fragments in many felsic pyroclastic deposits (Fig. 16).

4) Felsic magma evolution occurs only in the lower crust at pressures greater than 170 MPa (Fig. 13). No evidence is seen for magmatic stalling (and subsequent eruption) of felsic melts stored at pressures less than 170 MPa. The only modelled entrapment pressures from melt inclusions from a zoned fall deposit on Ascension Island showed that crystals grew in a storage region at 250 MPa (Chamberlain et al., 2016), with melt inclusions having up to 4 wt.% H_2O. This is in agreement with modelled entrapment pressures from felsic plutonic bodies being between 200 and 300 MPa (or 6.8 – 10.2 km, assuming a crustal density of 3000 kgm^{-3}; Webster & Rebbert, 2001). The modelled high water concentrations of melts from which feldspars have grown (Table 8) could support this storage and evolution within the lower crust (or Layer 3 of Klingelhöfer et al., 2001; Fig. 13, 16). Lower crustal storage means that any unrest signals will be harder to resolve, and has implications for the methods implemented to monitor future volcanic unrest on Ascension Island.

5) Magmas are erupted as discrete batches, with no evidence for long-lived storage, or for crystal recycling between eruptions in a mushy or melt-dominant magma storage region (cf. Kahl et al., 2013). Magma mixing is therefore not an eruptive trigger.

Instead, triggers could be internal (due to volatile over-pressure), or from external tectonic changes, which again presents challenges for monitoring potential future volcanic unrest at Ascension Island.

6) The magmas that fed explosive and effusive felsic eruptions exhibit differences in the presence or absence of low pressure phases (Fig. 14) perhaps suggestive of variation in the location of their storage regions and ascent rates, and warrants further investigation. However, fractional crystallisation (with minor crystal entrainment) of predominantly feldspars induced by stalling (at varying depths) in the nested (more felsic) plutonic region, remains the dominant evolutionary process for all felsic magmas, irrespective of the eruptive style.

Implications for the generation of felsic magmas on ocean islands

The petrogenetic processes responsible for the generation of felsic magmas in ocean island volcanoes built on thin oceanic crust have long been debated. Many authors suggested that felsic magma production at ocean island volcanoes could be a proxy for the initiation of continental crust formation in the Archean (e.g., Gazel et al., 2014; Mancini et al., 2015). While the low growth rates of Ascension Island (Minshull et al., 2010) negate its use in understanding Archean felsic magma genesis, the dominance of fractional crystallisation in the generation of felsic magmas, with little evidence for magma mixing, is unusual when compared with other ocean island volcanoes (e.g., the Canary Islands and Iceland: e.g. Borhson & Reid 1997; Caroff et al., 1999; Sverrisdottir, 2007; Carley et al., 2011; Longpré et al., 2014).

Open vs. closed system evolution

882 The new data presented here suggests evolution of Ascension Island magmas is dominated by
883 simple crystal fractionation in a relatively closed system of short-lived discrete storage
884 regions, and supports conclusions of previous workers (Harris et al., 1982; Kar et al., 1998;
885 Webster & Rebbert, 2001; Jicha et al., 2013; Chamberlain et al., 2016). This is contrary to
886 many other ocean island volcanoes where open system processes such as magma mixing and
887 significant partial melting of oceanic crust contribute to the formation of evolved magmas,
888 and where there is less evidence for closed system fractional crystallisation (Bohrson & Reid
889 1995, 1997; Caroff et al., 1999; Carley et al., 2011; Weismaier et al., 2013; Longpré et al.,
890 2014; Sliwinski et al., 2015). The main factor controlling whether open or closed system
891 behaviour dominates could be the magmatic flux: it has been shown that increased magma
892 fluxes correspond to increased degrees of crustal assimilation and crystal entrainment at mid
893 ocean ridges (Michael & Cornell, 1998). Ascension Island has an order of magnitude slower
894 growth rate when compared with Hawaii (Sharp & Renne, 2005; Minshull et al., 2010), and
895 thus we infer a significantly lower magmatic flux, which led to the development of small-
896 scale, short-lived magma storage regions, and closed system evolution of felsic magmas.
897 Multiple volcanic centres also display evidence for relatively closed system evolution of
898 mafic magmas by extensive fractional crystallisation to produce alkaline felsic magmas (e.g.
899 Volcán Alcedo in the Galápagos [Geist et al., 1995], Terceira, São Miguel and Graciosa in
900 the Azores [Mungall & Martin, 1995; Larrea et al., 2014; Jeffrey et al., 2016], and the extinct
901 Oki-Dōzen volcano, Japan [Brenna et al., 2015]). These islands are all likely the result of low
902 magmatic production rates, and are likely not related to a deep-seated mantle hotspots
903 (Hildenbrand et al., 2014; Métrich et al., 2014). Fractional crystallisation always requires the
904 formation of a large volume of plutonic rocks as a by-product of extensive fractional
905 crystallisation. Erupted lithic fragments or surface exposures provide evidence for these

906 plutonic rocks (Mungall & Martin, 1995; Larrea et al., 2014; Brenna et al., 2015; Jeffrey et
907 al., 2016).
908
909 *Fractional crystallisation: the space problem*
910 Extensive fractional crystallisation of > 80% mafic melt to produce the felsic magmas seen
911 on small ocean islands such as Ascension Island and the Azores implies that significant
912 volumes of plutonic material remain in the crust. While eruptive volumes are unconstrained
913 at Ascension Island due to high erosion rates and dispersal over the ocean, the high degrees
914 of fractionation responsible for a single body of felsic magma evolution suggest that
915 significant volumes of plutonic rocks remain in the crust. Taking the evolution from NE Bay
916 scoria to Middleton's Ridge rhyolite as an example, in total the rhyolite represents only ~9%
917 of the original mass of basalt. If we assume a modest eruptive volume of 0.2 km^3 (compared
918 with the AD 1630 eruption from São Miguel which evacuated ~0.85 km^3 of magma [DRE,
919 Cole et al., 1995]), then ~2 km^3 of fractionated crystals, preserved as plutonic rocks, remain
920 in the crust. Erupted volumes and degree of fractionation vary between eruptions, yet as over
921 70 eruptions of felsic magma have occurred over the last 1 million years on Ascension
922 (Preece et al., 2016), then a minimum of ~140 km^3 of plutonic rocks may remain in the crust,
923 with no evidence for their rejuvenation preserved in any volcanic products on Ascension
924 Island. This could be viewed as a minimum volume, given the lack of constraints on eruptive
925 volumes, and the unknown number of magmatic (not necessarily eruptive) events. Evidence
926 for a central nested plutonic core (Evangelidis et al., 2004) and over-thickening of layer 3
927 (where magmatic evolution is interpreted to occur at Ascension Island, see above) has been
928 observed in seismic reflection surveys (Klingelhöfer et al., 2001). Evangelidis et al. (2004)
929 suggest that the central high velocity region, inferred to consist of plutonic rocks (of
930 unknown compositions), could have a volume approaching 7000 km^3. This appears large

compared to our minimum estimates (above), however small discrete bodies of plutonics of varying composition would not be resolvable from the seismic reflection surveys, and therefore this volume represents an area affected by plutonism, not necessarily the volumes of individual plutonic bodies. Aside from over-thickening of layer 3 (Klingelhöfer et al., 2001), it remains unclear how such large potential volumes of plutonic rocks are accommodated in thin oceanic crust, yet their presence seems vital for the formation of evolved melts in low magma flux ocean island volcanoes.

CONCLUSIONS

- There are no differences in whole rock or crystal compositions from the lavas erupted in the same spatial regions of the island, suggesting that in the last 1 Myr the processes controlling mafic melt production and eruption have remained constant, even if source region composition and degree of partial melting have changed (cf. Jicha et al., 2013).
- Spatial variation in crystallinity and in the composition and origin of crystals between mafic eruptive centres highlights heterogeneity in the lower crust under Ascension Island. The mafic magmas which erupted along the South Coast region, as well as the Green Mountain scoria sample in the felsic complexes incorporated higher volumes of antecrysts during ascent, consistent with the observation of increased numbers of coherent plutonic lithic fragments in these lava flows.
- Felsic melt evolution at Ascension Island is dominantly controlled by crystal fractionation of ternary feldspar with minor fayalite or sodic clinopyroxene, dependent upon ascent rate and oxidation state of the magma, with isotopic evidence of minor crustal assimilation of seawater-altered crustal material (Kar et al., 1998). There is no evidence for magma mixing in any of the eruptive deposits studied here,

indicating that while a wide range of magma compositions are erupted across a ~12 km diameter island, they do not encounter other melts during their transport through the crust. Magmatic evolution occurs in small, short-lived, isolated magma storage regions in the lower crust. Antecrysts do not show reaction rims, and therefore their incorporation is purely mechanical and occurred late (during ascent).

- Alkali feldspar-melt hygrometry reveals high water concentrations of up to 8 wt.% H_2O in the more-evolved magmas. These high H_2O concentrations, combined with the lack of evidence for an external trigger in the crystal chemistry suggests that internal over-pressure from high degrees of fractional crystallisation concentrating H_2O in the liquid phase is a likely eruptive trigger for explosive eruptions on Ascension Island.
- Felsic magmas are almost entirely erupted in the central and eastern areas of Ascension Island implying a spatial control on the evolution of felsic melts. We infer that the presence of significant volumes of plutonic bodies at depth inhibits magma ascent in these regions, and allow magmas to evolve and incorporate antecrysts. While the origin and nature of these plutonic bodies is not yet known, they must pre-date the subaerial stage of Ascension Island volcanism. The presence of plutonic rocks as abundant lithic clasts in the central and eastern regions highlights the importance of heterogeneous crustal structure in the evolution of magmas in thin young oceanic crust at Ascension Island.

ACKNOWLEDGEMENTS

In memory of Jon Davidson (1959–2016). We thank Marc Holland, the Ascension Island Government, the Heritage Society, the Conservation Department and island residents (in particular Drew Avery) for their logistical support during field seasons. George Cooper, Chris

Hayward, Ian Schipper, Bertrand Lezé and Chris Ottley are thanked for their laboratory and technical assistance during the course of analyses for this project. Vibrant discussions with Ben Cohen, Julia Crummy, Bridie Davies, Sue Loughlin, Darren Mark, Jane Scarrow, Fin Stuart, Charlotte Vye-Brown and Barry Weaver helped in formulating our ideas. Constructive and considered reviews by Marco Brenna, Felix Genske, Karen Harpp and an anonymous reviewer, and the expert editorial handling of Wendy Bohrson have led to significant improvements to this manuscript.

FUNDING

This project was funded by a Leverhulme Trust Research Project Grant (RPG-2013-042), with the second field season supported by a Gloyne Outdoor Geological Research award from the Geological Society of London.

REFERENCES

Ablay, G. J., Carroll, M. R., Palmer, M. R., Martí, J., & Sparks, R. S. J. (1998). Basanite–phonolite lineages of the Teide–Pico Viejo volcanic complex, Tenerife, Canary Islands. *Journal of Petrology*, *39*(5), 905-936.

Allan, A. S., Wilson, C. J., Millet, M. A., & Wysoczanski, R. J. (2012). The invisible hand: Tectonic triggering and modulation of a rhyolitic supereruption. *Geology, 40(6),* 563-566.

Almeev, R., Holtz, F., Koepke, J., Haase, K., & Devey, C. (2008). Depths of partial crystallization of H2O-bearing MORB: phase equilibria simulations of basalts at the MAR near Ascension Island (7–11 S). *Journal of Petrology*, *49*(1), 25-45.

Arth, J. G. (1976). Behavior of trace elements during magmatic processes: a summary of theoretical models and their applications. *J. Res. US Geol. Surv.;(United States)*, *4*(1).

1006 Ashwal, L., Torsvik, T., Horváth, P., Harris, C., Webb, S., Werner, S., & Corfu, F. (2016). A
1007 Mantle-derived Origin for Mauritian Trachytes. *Journal of Petrology*, *57(9)*, 1645-
1008 1676
1009 Bacon, C. R. & Hirschmann, M. M. (1988). Mg/Mn partitioning as a test for equilibrium
1010 between coexisting Fe^Ti oxides. *American Mineralogist 73,* 57-61
1011 Bauer, K., Trumbull, R. B., & Vietor, T. (2003). Geophysical images and a crustal model of
1012 intrusive structures beneath the Messum ring complex, Namibia. *Earth and Planetary*
1013 *Science Letters*, *216*(1-2), 65-80.
1014 Bohrson, W. A., & Reid, M. R. (1995). Petrogenesis of alkaline basalts from Socorro Island,
1015 Mexico: Trace element evidence for contamination of ocean island basalt in the
1016 shallow ocean crust. *Journal of Geophysical Research: Solid Earth*, *100*(B12), 24555-
1017 24576.
1018 Bohrson, W. A., & Reid, M. R. (1997). Genesis of silicic peralkaline volcanic rocks in an
1019 ocean island setting by crustal melting and open-system processes: Socorro Island,
1020 Mexico. *Journal of Petrology*, *38*(9), 1137-1166.
1021 Bohrson, W. A., Reid, M. R., Grunder, A. L., Heizler, M. T., Harrison, T. M., & Lee, J.
1022 (1996). Prolonged history of silicic peralkaline volcanism in the eastern Pacific
1023 Ocean. *Journal of Geophysical Research: Solid Earth*, *101*(B5), 11457-11474.
1024 Bottinga, Y., & Weill, D. F. (1970). Densities of liquid silicate systems calculated from
1025 partial molar volumes of oxide components. *American Journal of Science, 269(2)*,
1026 169-182.
1027 Brenna, M., Nakada, S., Miura, D., Toshida, K., Ito, H., Hokanishi, N., & Nakai, S. I. (2015).
1028 A trachyte–syenite core within a basaltic nest: filtering of primitive injections by a
1029 multi-stage magma plumbing system (Oki-Dōzen, south-west Japan). *Contributions to*
1030 *Mineralogy and Petrology*, *170*(2), 1-21.

1031 Burke, K. C., & Wilson, J. T. (1976). Hot spots on the Earth's surface. *Scientific American,*
1032 *235*(2), 46-59.
1033 Caricchi, L., Sheldrake, T. E., & Blundy, J. (2018). Modulation of magmatic processes by
1034 CO2 flushing. *Earth and Planetary Science Letters, 491,* 160-171.
1035 Carley, T. L., Miller, C. F., Wooden, J. L., Bindeman, I. N., & Barth, A. P. (2011). Zircon
1036 from historic eruptions in Iceland: reconstructing storage and evolution of silicic
1037 magmas. *Mineralogy and Petrology*, *102*(1-4), 135-161.
1038 Caroff, M., Guillou, H., Lamiaux, M., Maury, R. C., Guille, G., & Cotten, J. (1999).
1039 Assimilation of ocean crust by hawaiitic and mugearitic magmas: an example from
1040 Eiao (Marquesas). *Lithos*, *46*(2), 235-258.
1041 Carracedo, J.C., Badiola, E.R., Guillou, H., Paterne, M., Scaillet, S., Torrado, F.P., Paris, R.,
1042 Fra-Paleo, U. & Hansen, A., (2007). Eruptive and structural history of Teide Volcano
1043 and rift zones of Tenerife, Canary Islands. *Geological Society of America*
1044 *Bulletin*, *119*(9-10), 1027-1051.
1045 Chamberlain, K. J., Barclay, J., Preece, K., Brown, R. J., & Davidson, J. P. (2016). Origin
1046 and evolution of silicic magmas at ocean islands: Perspectives from a zoned fall
1047 deposit on Ascension Island, South Atlantic. *Journal of Volcanology and Geothermal*
1048 *Research, 327,* 349-360.
1049 Charlier, B. L. A., Wilson, C. J. N., Lowenstern, J. B., Blake, S., Van Calsteren, P. W., &
1050 Davidson, J. P. (2005). Magma generation at a large, hyperactive silicic volcano
1051 (Taupo, New Zealand) revealed by U–Th and U–Pb systematics in zircons. *Journal of*
1052 *Petrology*, *46*(1), 3-32.
1053 Charlier, B., Namur, O., & Grove, T. L. (2013). Compositional and kinetic controls on liquid
1054 immiscibility in ferrobasalt–rhyolite volcanic and plutonic series. *Geochimica et*
1055 *Cosmochimica Acta*, *113*, 79-93.

1056 Cole, P. D., Queiroz, G., Wallenstein, N., Gaspar, J. L., Duncan, A. M., & Guest, J. E.
1057 (1995). An historic subplinian/phreatomagmatic eruption: the 1630 AD eruption of
1058 Furnas volcano, Saõ Miguel, Azores. *Journal of Volcanology and Geothermal*
1059 *Research*, *69*(1), 117-135.
1060 Coogan, L.A., Kempton, P. D., Saunders, A. D., Norry, M. J. (2000): Melt aggregation within
1061 the crust beneath the Mid-Atlantic Ridge: evidence from plagioclase and
1062 clinopyroxene major and trace element compositions. *Earth and Planetary Science*
1063 *Letters*, *176*(2), 245-257.
1064 Coombs, D. W. (1963). Trends and affinities of basaltic magmas and pyroxenes as illustrated
1065 on the diopside-olivine-silica diagram: in Miscellaneous papers—International
1066 Mineralogical Association Third General Meeting, Mineral. Soc. Amer., Spec. Pap.,
1067 Vol. 1, p. 227-250.
1068 Daly, R. A. (1925, June). The geology of Ascension Island. In *Proceedings of the American*
1069 *Academy of Arts and Sciences* (Vol. 60, No. 1, pp. 3-80). American Academy of Arts
1070 & Sciences.
1071 Davidson J. P., Kar A. & Weaver B. L. (1997). The origin of extreme isotope signatures
1072 among differentiated rocks from Ascension Island. *Geological Society of America,*
1073 *Abstracts with Programs 29*, A-89.
1074 Davis, A. S., Clague, D. A., & Paduan, J. B. (2007). Diverse origins of xenoliths from
1075 seamounts at the continental margin, offshore central California. *Journal of*
1076 *Petrology*, *48*(5), 829-852.
1077 Di Matteo, V., Carroll, M. R., Behrens, H., Vetere, F., & Brooker, R. A. (2004). Water
1078 solubility in trachytic melts. *Chemical Geology*, *213*(1-3), 187-196.

1079 Druitt, T. H., Brenchley, P. J., Gökten, Y. E., & Francaviglia, V. (1995). Late Quaternary
1080 rhyolitic eruptions from the Acigöl Complex, central Turkey. *Journal of the*
1081 *Geological Society*, *152*(4), 655-667.
1082 Eichelberger, J. C. (1995). Silicic volcanism: ascent of viscous magmas from crustal
1083 reservoirs. *Annual Review of Earth and Planetary Sciences*, *23*(1), 41-63.
1084 Evangelidis, C. P., Minshull, T. A., & Henstock, T. J. (2004). Three-dimensional crustal
1085 structure of Ascension Island from active source seismic tomography. *Geophysical*
1086 *Journal International*, *159*(1), 311-325.
1087 Ewart, A., & Griffin, W. L. (1994). Application of proton-microprobe data to trace-element
1088 partitioning in volcanic rocks. *Chemical Geology*, *117*(1-4), 251-284.
1089 Fowler, S. J., & Spera, F. J. (2010). A metamodel for crustal magmatism: phase equilibria of
1090 giant ignimbrites. *Journal of Petrology, 51*(9), 1783-1830.
1091 Gazel, E., Hayes, J. L., Kelemen, P. B., Everson, E. D., Holbrook, W. S., & Vance, E. (2014,
1092 December). Generation of continental crust in intra-oceanic arcs. In *AGU Fall*
1093 *Meeting Abstracts* (Vol. 1, p. 4845).
1094 Geist, D. J., White, W. M., & McBirney, A. R. (1988). Plume-asthenosphere mixing beneath
1095 the Galapagos archipelago. *Nature*, *333*(6174), 657.
1096 Geist, D., Howard, K. A., & Larson, P. (1995). The generation of oceanic rhyolites by crystal
1097 fractionation: the basalt-rhyolite association at Volcan Alcedo, Galapagos
1098 Archipelago. *Journal of Petrology*, *36*(4), 965-982.
1099 Ghiorso, M. S., & Evans, B. W. (2008). Thermodynamics of rhombohedral oxide solid
1100 solutions and a revision of the Fe-Ti two-oxide geothermometer and oxygen-barometer.
1101 *American Journal of Science*, *308*(9), 957-1039.

1102 Giordano, D., Romano, C., Dingwell, D. B., Poe, B., & Behrens, H. (2004). The combined
1103 effects of water and fluorine on the viscosity of silicic magmas. *Geochimica et*
1104 *Cosmochimica Acta*, *68*(24), 5159-5168.
1105 Glazner, A. F. (2007). Thermal limitations on incorporation of wall rock into
1106 magma. *Geology*, *35*(4), 319-322.
1107 Goldich, S. S., Ingamells, C. O., Suhr, N. H. & Anderson, D. H. (1967). Analyses of silicate
1108 rock and mineral standards. *Canadian Journal of Earth Sciences* **4**, 747-755.
1109 Gualda, G. A., & Ghiorso, M. S. (2015). MELTS_Excel: A Microsoft Excel‐based MELTS
1110 interface for research and teaching of magma properties and evolution. *Geochemistry,*
1111 *Geophysics, Geosystems*, *16*(1), 315-324.
1112 Gualda, G. A., Ghiorso, M. S., Lemons, R. V., & Carley, T. L. (2012). Rhyolite-MELTS: a
1113 modified calibration of MELTS optimized for silica-rich, fluid-bearing magmatic
1114 systems. *Journal of Petrology, 53*(5), 875-890.
1115 Harpp, K. S., & White, W. M. (2001). Tracing a mantle plume: Isotopic and trace element
1116 variations of Galápagos seamounts. *Geochemistry, Geophysics, Geosystems*, *2*(6).
1117 Harris, C. (1983). The petrology of lavas and associated plutonic inclusions of Ascension
1118 Island. *Journal of Petrology*, *24*(4), 424-470.
1119 Harris, C. (1986). A quantitative study of magmatic inclusions in the plutonic ejecta of
1120 Ascension Island. *Journal of Petrology*, *27*(1), 251-276.
1121 Harris, C., Bell, J. D., & Atkins, F. B. (1982). Isotopic composition of lead and strontium in
1122 lavas and coarse-grained blocks from Ascension Island, South Atlantic. *Earth and*
1123 *Planetary Science Letters*, *60*(1), 79-85.
1124 Hildenbrand, A., Weis, D., Madureira, P., & Marques, F. O. (2014). Recent plate re-
1125 organization at the Azores Triple Junction: Evidence from combined geochemical and

1126 geochronological data on Faial, S. Jorge and Terceira volcanic islands. *Lithos*, *210*,
1127 27-39.
1128 Hobson, K.E. (2001). The pyroclastic deposits and eruption history of Ascension Island: a
1129 palaeomagnetic and volcanological study. *Doctoral dissertation, University of*
1130 *Oxford*.
1131 Humphreys, M. C., Christopher, T., & Hards, V. (2009). Microlite transfer by disaggregation
1132 of mafic inclusions following magma mixing at Soufrière Hills volcano,
1133 Montserrat. *Contributions to Mineralogy and Petrology*, *157*(5), 609-624.
1134 Ingamells, C. O. (1980). Analysed minerals for electron microprobe standards. *Geostandards*
1135 *Newsletter* **2**, 115.
1136 Jarosewich, E., Nelen, J. A. & Norberg, J. A. (1980). Reference samples for electron
1137 microprobe analysis. *Geostandards Newsletter* **4,** 43-47.
1138 Jeffery, A. J., Gertisser, R., O'Driscoll, B., Pacheco, J. M., Whitley, S., Pimentel, A., & Self, S.
1139 (2016). Temporal evolution of a post-caldera, mildly peralkaline magmatic system:
1140 Furnas volcano, São Miguel, Azores. *Contributions to Mineralogy and*
1141 *Petrology*, *171*(5), 1-24
1142 Jicha, B. R., Singer, B. S., & Valentine, M. J. (2013). 40Ar/39Ar Geochronology of Subaerial
1143 Ascension Island and a Re-evaluation of the Temporal Progression of Basaltic to
1144 Rhyolitic Volcanism. *Journal of Petrology*, *54*(12), 2581-2596.
1145 Jochum, K. P., Weis, U., Stoll, B., Kuzmin, D., Yang, Q., Raczek, I., Jacob, D.E., Stracke, A.,
1146 Birbaum, K., Frick, D.A. & Günther, D. (2011). Determination of reference values for
1147 NIST SRM 610–617 glasses following ISO guidelines. *Geostandards and*
1148 *Geoanalytical Research*, *35*(4), 397-429.
1149 Jochum, K. P., Weis, U., Schwager, B., Stoll, B., Wilson, S. A., Haug, G. H., Andreae, M. O.
1150 & Enzweiler, J. (2016). Reference values following ISO guidelines for frequently

requested rock reference materials. *Geostandards and Geoanalytical Research*, *40*(3), 333-350.

Kahl, M., Chakraborty, S., Costa, F., Pompilio, M., Liuzzo, M., & Viccaro, M. (2013). Compositionally zoned crystals and real-time degassing data reveal changes in magma transfer dynamics during the 2006 summit eruptive episodes of Mt. Etna. *Bulletin of Volcanology*, *75*(2), 1-14

Kar, A. (1997). A comprehensive geological, geochemical, and petrogenetic study of hotspot-related oceanic basalt–rhyolite series rocks from Ascension Island, South Atlantic Ocean. Norman: University of Oklahoma. p. 260. Unpublished Ph.D. dissertation.

Kar, A., Weaver, B., Davidson, J., & Colucci, M. (1998). Origin of differentiated volcanic and plutonic rocks from Ascension Island, South Atlantic Ocean. *Journal of Petrology*, *39*(5), 1009-1024.

Klingelhöfer, F., Minshull, T. A., Blackman, D. K., Harben, P., & Childers, V. (2001). Crustal structure of Ascension Island from wide-angle seismic data: implications for the formation of near-ridge volcanic islands. *Earth and Planetary Science Letters*, *190*(1), 41-56

Klügel, A. Hansteen, T. H. & Galipp, K. (2005). Magma storage and underplating beneath Cumbre Vieja volcano, La Palma (Canary Islands). *Earth and Planetary Science Letters* **236**, 211-226.

Koppers, A. A., & Staudigel, H. (2005). Asynchronous bends in Pacific seamount trails: a case for extensional volcanism? *Science*, *307*(5711), 904-907.

Kuehn, S. C., Froese, D. G., Pearce, N. J., & Foit, F. F. (2009, December). ID3506, a new/old Lipari obsidian standard for characterization of natural glasses and for tephrochronology. In *AGU Fall Meeting Abstracts*.

1175 Kuritani, T., Yokoyama, T., Kitagawa, H., Kobayashi, K., & Nakamura, E. (2011).
1176 Geochemical evolution of historical lavas from Askja Volcano, Iceland: Implications
1177 for mechanisms and timescales of magmatic differentiation. *Geochimica et*
1178 *Cosmochimica Acta*, *75*(2), 570-587.
1179 Larrea, P., Galé, C., Ubide, T., Widom, E., Lago, M., & França, Z. (2014). Magmatic
1180 Evolution of Graciosa (Azores, Portugal). *Journal of Petrology*, *55*(11), 2125-2154.
1181 Lemarchand, F., Villemant, B., & Calas, G. (1987). Trace element distribution coefficients in
1182 alkaline series. *Geochimica et Cosmochimica Acta*, *51*(5), 1071-1081.
1183 Longpré, M. A., Klügel, A., Diehl, A., & Stix, J. (2014). Mixing in mantle magma reservoirs
1184 prior to and during the 2011–2012 eruption at El Hierro, Canary
1185 Islands. *Geology*, *42*(4), 315-318.
1186 Luhr, J. F., & Carmichael, I. S. (1990). Petrological monitoring of cyclical eruptive activity at
1187 Volcan Colima, Mexico. *Journal of Volcanology and Geothermal Research*, *42*(3),
1188 235-260.
1189 Mahood, G. A., & Stimac, J. A. (1990). Trace-element partitioning in pantellerites and
1190 trachytes. *Geochimica et Cosmochimica Acta*, *54*(8), 2257-2276.
1191 Mahood, G., & Hildreth, W. (1983). Large partition coefficients for trace elements in high-
1192 silica rhyolites. *Geochimica et Cosmochimica Acta*, *47*(1), 11-30.
1193 Mancini, A., Mattsson, H. B., & Bachmann, O. (2015). Origin of the compositional diversity
1194 in the basalt-to-dacite series erupted along the Heiðarsporður ridge, NE Iceland.
1195 *Journal of Volcanology and Geothermal Research*, *301*, 116-127.
1196 Markl, G., Marks, M. A., & Frost, B. R. (2010). On the controls of oxygen fugacity in the
1197 generation and crystallization of peralkaline melts. *Journal of Petrology*, *51*(9), 1831-
1198 1847.

1199 Meade, F. C., Troll, V. R., Ellam, R. M., Freda, C., Font, L., Donaldson, C. H., &
1200 Klonowska, I. (2014). Bimodal magmatism produced by progressively inhibited
1201 crustal assimilation. *Nature Communications*, *5,* 4199.
1202 Métrich, N., Zanon, V., Créon, L., Hildenbrand, A., Moreira, M., & Marques, F. O. (2014). Is
1203 the 'Azores hotspot'a wetspot? Insights from the geochemistry of fluid and melt
1204 inclusions in olivine of Pico basalts. *Journal of Petrology*, *55*(2), 377-393.
1205 Michael, P. J., & Cornell, W. C. (1998). Influence of spreading rate and magma supply on
1206 crystallization and assimilation beneath mid-ocean ridges: Evidence from chlorine
1207 and major element chemistry of mid-ocean ridge basalts. *Journal of Geophysical*
1208 *Research: Solid Earth, 103(*B8), 18325-18356.
1209 Minshull, T. A., Ishizuka, O., & Garcia-Castellanos, D. (2010). Long-term growth and
1210 subsidence of Ascension Island: Constraints on the rheology of young oceanic
1211 lithosphere. *Geophysical Research Letters*, *37*(23).
1212 Mollo, S., Masotta, M., Forni, F., Bachmann, O., De Astis, G., Moore, G., & Scarlato, P.
1213 (2015). A K-feldspar–liquid hygrometer specific to alkaline differentiated
1214 magmas. *Chemical Geology*, *392*, 1-8.
1215 Montelli, R., Nolet, G., Dahlen, F. A., Masters, G., Engdahl, E. R., & Hung, S. H. (2004).
1216 Finite-frequency tomography reveals a variety of plumes in the
1217 mantle. *Science*, *303*(5656), 338-343
1218 Montelli, R., Nolet, G., Dahlen, F. A., & Masters, G. (2006). A catalogue of deep mantle
1219 plumes: New results from finite‐frequency tomography. *Geochemistry, Geophysics,*
1220 *Geosystems*, *7*(11).
1221 Mungall, J. E., & Martin, R. F. (1995). Petrogenesis of basalt-comendite and basalt-
1222 pantellerite suites, Terceira, Azores, and some implications for the origin of ocean-
1223 island rhyolites. *Contributions to Mineralogy and Petrology*, *119*(1), 43-55.

1224 Nash, W. P., & Crecraft, H. R. (1985). Partition coefficients for trace elements in silicic
1225 magmas. *Geochimica et Cosmochimica Acta*, *49*(11), 2309-2322
1226 Niu, Y., Wilson, M., Humphreys, E. R., & O'hara, M. J. (2011). The origin of intra-plate
1227 ocean island basalts (OIB): the lid effect and its geodynamic implications. *Journal of*
1228 *Petrology, 52*(7-8), 1443-1468.
1229 Nielson, D. L., & Sibbett, B. S. (1996). Geology of Ascension Island, South Atlantic Ocean.
1230 *Geothermics*, *25*(4), 427-448.
1231 Palme, H., & O'Neill, H. S. C. (2003). Cosmochemical estimates of mantle
1232 composition. *Treatise on Geochemistry*, *2*, 568.
1233 Panjasawatwong, Y., Danyushevsky, L. V., Crawford, A. J., & Harris, K. L. (1995). An
1234 experimental study of the effects of melt composition on plagioclase-melt equilibria at
1235 5 and 10 kbar: implications for the origin of magmatic high-An
1236 plagioclase. *Contributions to Mineralogy and Petrology*, *118*(4), 420-432.
1237 Papale, P., Neri, A., & Macedonio, G. (1998). The role of magma composition and water
1238 content in explosive eruptions: 1. Conduit ascent dynamics. *Journal of Volcanology*
1239 *and Geothermal Research*, *87*(1-4), 75-93.
1240 Paulick, H., Münker, C., & Schuth, S. (2010). The influence of small-scale mantle
1241 heterogeneities on Mid-Ocean Ridge volcanism: evidence from the southern Mid-
1242 Atlantic Ridge (7 30′ S to 11 30′ S) and Ascension Island. *Earth and Planetary*
1243 *Science Letters*, *296*(3), 299-310.
1244 Pearce, J. A., & Norry, M. J. (1979). Petrogenetic implications of Ti, Zr, Y, and Nb variations
1245 in volcanic rocks. *Contributions to Mineralogy and Petrology*, *69*(1), 33-47.
1246 Petrelli, M., Poli, G., Perugini, D., & Peccerillo, A. (2005). PetroGraph: A new software to
1247 visualize, model, and present geochemical data in igneous petrology. *Geochemistry,*
1248 *Geophysics, Geosystems*, *6*(7).

1249 Preece, K., Mark, D. F., Barclay, J., Cohen, B. E., Chamberlain, K. J., Jowitt, C., Vye-Brown,
1250 C., Brown, R. J. (2018). Bridging the gap: $^{40}Ar/^{39}Ar$ dating of volcanic eruptions from
1251 the 'Age of Discovery'. *Geology, 46*(12), 1035-1038.
1252 Preece, K., Barclay, J., Brown, R., Mark, D. F., Chamberlain, K, Cohen, B. E., Vye-Brown,
1253 C. (2016) A 1 million year eruption history of Ascension Island: insights from
1254 stratigraphy and $^{40}Ar/^{39}Ar$ dating. Cities on Volcanoes 9, Puerto Varas, Chile, Nov,
1255 2016
1256 Price, R. C., Gamble, J. A., Smith, I. E., Maas, R., Waight, T., Stewart, R. B., & Woodhead,
1257 J. (2012). The anatomy of an Andesite volcano: a time–stratigraphic study of andesite
1258 petrogenesis and crustal evolution at Ruapehu Volcano, New Zealand. *Journal of*
1259 *Petrology*, *53*(10), 2139-2189.
1260 Putirka, K. D. (2008). Thermometers and barometers for volcanic systems. *Reviews in*
1261 *Mineralogy and Geochemistry*, *69*(1), 61-120.
1262 Roedder, E., & Coombs, D. S. (1967). Immiscibility in Granitic Melts, Indicated by Fluid
1263 Inclusions in Ejected Granitic Blocks from Ascension Island. *Journal of*
1264 *Petrology*, *8*(3), 417-451.
1265 Rooney, T. O., Hart, W. K., Hall, C. M., Ayalew, D., Ghiorso, M. S., Hidalgo, P., & Yirgu,
1266 G. (2012). Peralkaline magma evolution and the tephra record in the Ethiopian Rift.
1267 *Contributions to Mineralogy and Petrology, 164*(3), 407-426.
1268 Rollinson, H. R. (1993). *Using geochemical data: evaluation, presentation, interpretation*.
1269 Routledge.
1270 Scoates, J. S. (2000). The plagioclase–magma density paradox re-examined and the
1271 crystallization of Proterozoic anorthosites. *Journal of Petrology, 41(5)*, 627-649.

1272 Sharp, W. D., & Renne, P. R. (2005). The 40Ar/39Ar dating of core recovered by the Hawaii
1273 Scientific Drilling Project (phase 2), Hilo, Hawaii. *Geochemistry, Geophysics,*
1274 *Geosystems*, *6*(4).
1275 Sliwinski, J. T., Bachmann, O., Ellis, B. S., Dávila-Harris, P., Nelson, B. K., & Dufek, J.
1276 (2015). Eruption of Shallow Crystal Cumulates during Explosive Phonolitic Eruptions
1277 on Tenerife, Canary Islands. *Journal of Petrology*, *56*(11), 2173-2194.
1278 Sparks, R. S. J., & Sigurdsson, H. (1987). The 1875 eruption of Askja volcano, Iceland:
1279 combined fractional crystallization and selective contamination in the generation of
1280 rhyolitic magma. *Mineralogical Magazine, 51*(360), 183-202.
1281 Stock, M. J., Humphreys, M. C., Smith, V. C., Isaia, R., & Pyle, D. M. (2016). Late-stage
1282 volatile saturation as a potential trigger for explosive volcanic eruptions. *Nature*
1283 *Geoscience, 9(3),* 249.
1284 Stormer, J. C., & Nicholls, J. (1978). XLFRAC: a program for the interactive testing of
1285 magmatic differentiation models. *Computers & Geosciences*, *4*(2), 143-159.
1286 Sverrisdottir, G. (2007). Hybrid magma generation preceding Plinian silicic eruptions at
1287 Hekla, Iceland: evidence from mineralogy and chemistry of two zoned deposits.
1288 *Geological Magazine*, *144*(04), 643-659.
1289 Troll, V. R., & Schmincke, H. U. (2002). Magma mixing and crustal recycling recorded in
1290 ternary feldspar from compositionally zoned peralkaline ignimbrite ‘A’, Gran
1291 Canaria, Canary Islands. *Journal of Petrology*, *43*(2), 243-270.
1292 Watson, E. B., & Green, T. H. (1981). Apatite/liquid partition coefficients for the rare earth
1293 elements and strontium. *Earth and Planetary Science Letters*, *56*, 405-421.
1294 Weaver, B. L., Wood, D. A., Tarney, J., & Joron, J. L. (1987). Geochemistry of ocean island
1295 basalts from the south Atlantic: Ascension, Bouvet, St. Helena, Gough and Tristan da
1296 Cunha. *Geological Society, London, Special Publications*, *30*(1), 253-267.

1297 Weaver, B., Kar, A., Davidson, J., & Colucci, M. (1996). Geochemical characteristics of
1298 volcanic rocks from Ascension Island, South Atlantic Ocean. *Geothermics*, *25*(4),
1299 449-470.
1300 Webster, J. D., & Rebbert, C. R. (2001). The geochemical signature of fluid-saturated magma
1301 determined from silicate melt inclusions in Ascension Island granite xenoliths.
1302 *Geochimica et Cosmochimica Acta*, *65*(1), 123-136.
1303 Weis, D., Demaiffe, D., Cauet, S., & Javoy, M. (1987). Sr, Nd, O and H isotopic ratios in
1304 Ascension Island lavas and plutonic inclusions; cogenetic origin. *Earth and Planetary*
1305 *Science Letters*, *82*(3), 255-268.
1306 Wiesmaier, S., Troll, V. R., Wolff, J. A., & Carracedo, J. C. (2013). Open-system processes
1307 in the differentiation of mafic magma in the Teide–Pico Viejo succession, Tenerife.
1308 *Journal of the Geological Society*, *170*(3), 557-570.
1309 White, J. C., Holt, G. S., Parker, D. F., & Ren, M. (2003). Trace-element partitioning
1310 between alkali feldspar and peralkalic quartz trachyte to rhyolite magma. Part I:
1311 Systematics of trace-element partitioning. *American Mineralogist*, *88*(2-3), 316-329.
1312 White, J. C., Parker, D. F., & Ren, M. (2009). The origin of trachyte and pantellerite from
1313 Pantelleria, Italy: insights from major element, trace element, and thermodynamic
1314 modelling. *Journal of Volcanology and Geothermal Research*, *179*(1), 33-55.
1315 Zhao, D. (2004). Global tomographic images of mantle plumes and subducting slabs: insight
1316 into deep Earth dynamics. *Physics of the Earth and Planetary Interiors*, *146*(1), 3-34.

1317 **FIGURE CAPTIONS**

1318 Figure 1: Geological map of Ascension Island, located 90 km from the Mid Atlantic Ridge
1319 and between the Ascension Fracture Zone (AFZ) and Boca Verde Fracture Zone
1320 (BVFZ; inset), adapted from Weaver et al. (1995), Paulick et al. (2010) & Chamberlain
1321 et al. (2016). Sample locations indicated by triangles, diamonds and pentagons;
1322 eruptive centres identified in grey font. Surface expressions of known faults outlined in
1323 red. Major lava flow boundaries are indicated with black lines in the mafic lava flows.

1324 Figure 2: (a) Radiogenic isotope variations in Ascension Island lavas (subaerial unless
1325 otherwise stated); (b) Trace HFSE variation with major element variations; (c) Adapted
1326 from Jicha et al., 2013, trace element variation in Ascension lavas, showing the
1327 variation due to source heterogeneity, differentiation, and Fe-Ti oxide controlled
1328 fractionation paths; (d) variation in $^{143}Nd/^{144}Nd$ with degree of evolution (MgO). All
1329 data presented is a combination of Weaver et al. (1995, grey diamonds), Kar et al.
1330 (1998, orange diamonds), Paulick et al. (2010, blue squares) and Jicha et al. (2013,
1331 crosses).

1332 Figure 3: (a) Whole rock compositions of selected samples compared with all known
1333 Ascension Island whole rock data in grey field- (data from Weaver et al., 1996, Kar et
1334 al., 1998, Jicha et al., 2013). Diagram adapted from LeMaitre et al. (1989). (b)
1335 Primitive mantle (Palme & O'Neill, 2003) normalised trace element ranges for mafic-
1336 intermediate lavas (purple), scoria samples (orange), pumice samples (yellow) and
1337 felsic lava samples (blue).

1338 Figure 4: Whole rock variation in major and trace elements for all studied samples of
1339 Ascension Island mafic-intermediate lavas (purple triangles), felsic lavas (blue
1340 pentagons) and pyroclastics both pumiceous (yellow diamonds) and scoriaceous

(orange diamonds). Grey fields represent the full range of compositions found at Ascension from Weaver et al. (1995). For full data set, see Electronic Appendix 2.

Figure 5: Photomicrographs of Ascension lava samples. (a, b): Young South Coast lava sample showing a glomerocryst of feldspar and olivine; (c, d): Young Sisters lava sample showing euhedral plagioclase feldspar in a microcrystalline matrix; (e, f): Cricket Valley lava with sodic feldspars and minor aegirine-augite in a microcrystalline groundmass; (g): Letterbox felsic lava with large ternary feldspar phenocrysts in a microcrystalline groundmass; (h): Ariane lava flow with ternary feldspars and aegirine-augite in a microcrystalline groundmass. Images (a, c, e, g) in plane-polarised light; images (b, d, f, h) in cross-polarised light. Sample numbers relate to those listed in Table 1 and numbers in square brackets show whole rock SiO_2 concentrations.

Figure 6: Back Scattered Electron (BSE) images of Ascension Island lavas. Sample numbers relate to those listed in Table 1 and numbers in square brackets show whole rock SiO_2 concentrations. Features labelled in red refer to A: Reverse-zoned feldspar; B: Normally-zoned olivine; C: Faint oscillatory-zoned plagioclase. D: Mafic lava groundmass, typically consisting of feldspar + olivine + magnetite ± clinopyroxene ± ilmenite; E: Unzoned feldspar typical of felsic products; F: Unzoned fayalitic olivine; G: Groundmass of felsic lavas flows consists dominantly of feldspar with minor interstitial aegirine and fayalite; H: Dark in BSE cristobalite with characteristic fish-scale textures replacing groundmass and some feldspar crystals.

Figure 7: Ternary feldspar diagrams showing all feldspars differentiated by composition and eruptive style. For full data set see Electronic Appendix 2.

Figure 8: Compositions of feldspars from (a) mafic to intermediate lavas; (b) felsic lavas and (c, d) all Ascension Island samples. Sample areas relate to those used in Table 1. For full data set see Electronic Appendix 2. The purple field on panel (b) shows the

compositions of feldspars from mafic to intermediate lava samples. The pink field on panel (b) shows the Mid Atlantic Ridge ocean crust feldspars from the Kane Fracture Zone (Coogan et al., 2000). Core-rim differences within individual samples shown by filled (core) and open (rim) symbols in (c); sample colours and shapes refer to those listed in the key on (c).

Figure 9: Variation in plagioclase (a) and olivine (b) compositions with whole rock SiO_2 (a) or Mg# (b), and the calculated equilibrium compositions of the respective crystal phases based on whole rock XRF data (Table 1, and Electronic Appendix 2). In (a) equilibrium compositions of feldspar are calculated at 1150 °C and 330 MPa (black) and 1050 °C and 330 MPa (grey) respectively, based on feldspar-melt and Fe-Ti oxide thermometry (see Table 8), and the pressure at the base of the crust at Ascension Island (Klingelhöfer, 2001).

Figure 10: Compositions of olivines from (a) mafic to intermediate lavas; (b) all pyroclastic samples. Variations between core and rim compositions shown in panel (c), where open symbols refer to rim analyses, and filled symbols core analyses. Sample areas relate to those used in Table 1. For full data set see Electronic Appendix 2. The purple field on (b) shows the compositions of olivines from mafic to intermediate lava samples.

Figure 11: Compositions of pyroxenes from all Ascension Island samples. Triangles refer to samples of mafic to intermediate lava samples; squares and circles are felsic lava samples. Sample areas relate to those used in Table 1. For full data set see Electronic Appendix 2.

Figure 12: Matrix glass compositions from all Ascension Island samples. Sample areas relate to those used in Table 1. For full data set see Electronic Appendix 2.

Figure 13: Combined liquid lines of descent modelled from AI14-438 (to 950 °C, end marked by dashed line) and AI-621 (< 950 °C, start from dashed line) using rhyolite-MELTS

(Gualda & Ghiorso, 2015) at 330 MPa, 250 MPa, 170 MPa and 90 MPa. Purple ticks mark 20% increments of melt fraction remaining; grey ticks mark 10% melt fraction remaining, black ticks show liquid composition at 5% melt fraction remaining. Initial water concentrations for AI-438 were 0.5 wt.% H_2O, from MAR glasses showing a component of the fertile mantle end member suggested to be the source of magmatism at Ascension Island (Almeev et al., 2008; Paulick et al., 2010). *XRF data used is a combination of data presented here and Weaver et al. (1996) and Kar (1997).

Figure 14: Modelled fractionating crystal compositions from MELTS (purple symbols representing different pressures of crystallisation, Gualda & Ghiorso, 2015) compared with those measured in this study (grey symbols). The decompression trend (black crosses) represents isothermal decompression at 800 °C from 90 to 1 MPa.

Figure 15: Trace element fractional crystallisation modelling following the stages modelling using Petrograph (Petrelli et al., 2005). XRF data used for the modelling shown in diamonds, the resultant modelled liquid as diamonds. Each stage (1 – 4, connected by dashed lines) represents 0.92, 0.40, 0.16, 0.07 total melt fraction remaining. *Total XRF data field in grey is a combination of data presented here, and Weaver et al., 1996 and Kar, 1997. [1], [2]: For stages and full modelled compositions and references for partition coefficients used, see Electronic Appendix 3. The dashed field in (a) represents a subset of samples which plot towards syenitic samples of Ascension (not sampled in this study) and thus not modelled here.

Figure 16: Magmatic plumbing system model for Ascension Island- magma storage regions are not to scale. Note the geographic variation in the distribution of plutonic bodies (mafic plutonics in blue, zone of nested felsic plutonics hashed, with examples in purple) within the crust. Ascent paths shown in red (mafic) and purple-blue (felsics). Crustal structure derived from Klingelhöfer et al. (2001).

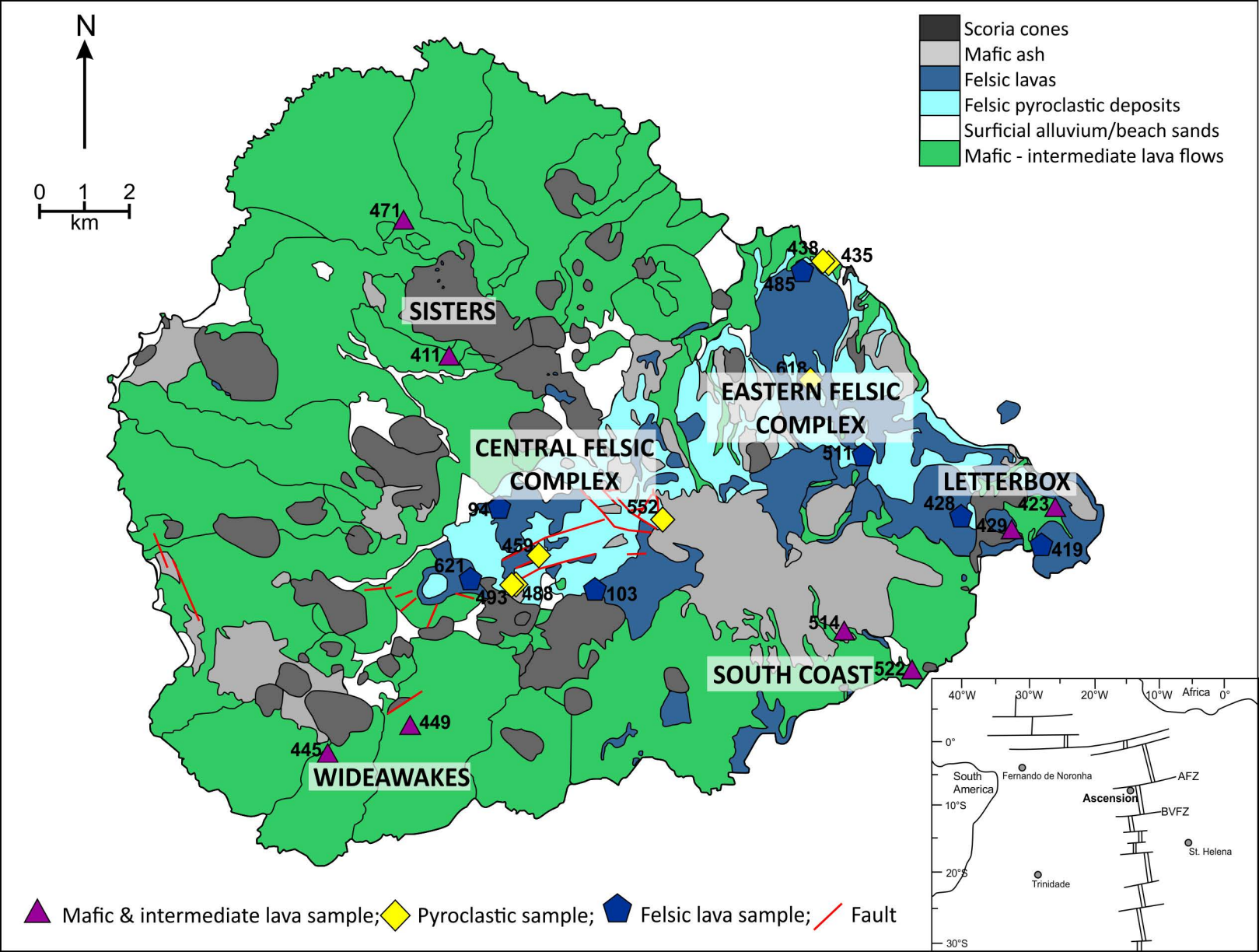
N
0 1 2
km
Scoria cones
Mafic ash
Felsic lavas
Felsic pyroclastic deposits
Surficial alluvium/beach sands
Mafic - intermediate lava flows
SISTERS
CENTRAL FELSIC COMPLEX
EASTERN FELSIC COMPLEX
LETTERBOX
SOUTH COAST
WIDEAWAKES
471
411
438
435
485
618
511
428
423
429
419
94
552
459
621
493
488
103
514
522
449
445
Mafic & intermediate lava sample;
Pyroclastic sample;
Felsic lava sample;
Fault
40°W
30°W
20°W
10°W
Africa
0°
South America
Fernando de Noronha
Ascension
AFZ
BVFZ
10°S
St. Helena
20°S
Trinidade
30°S

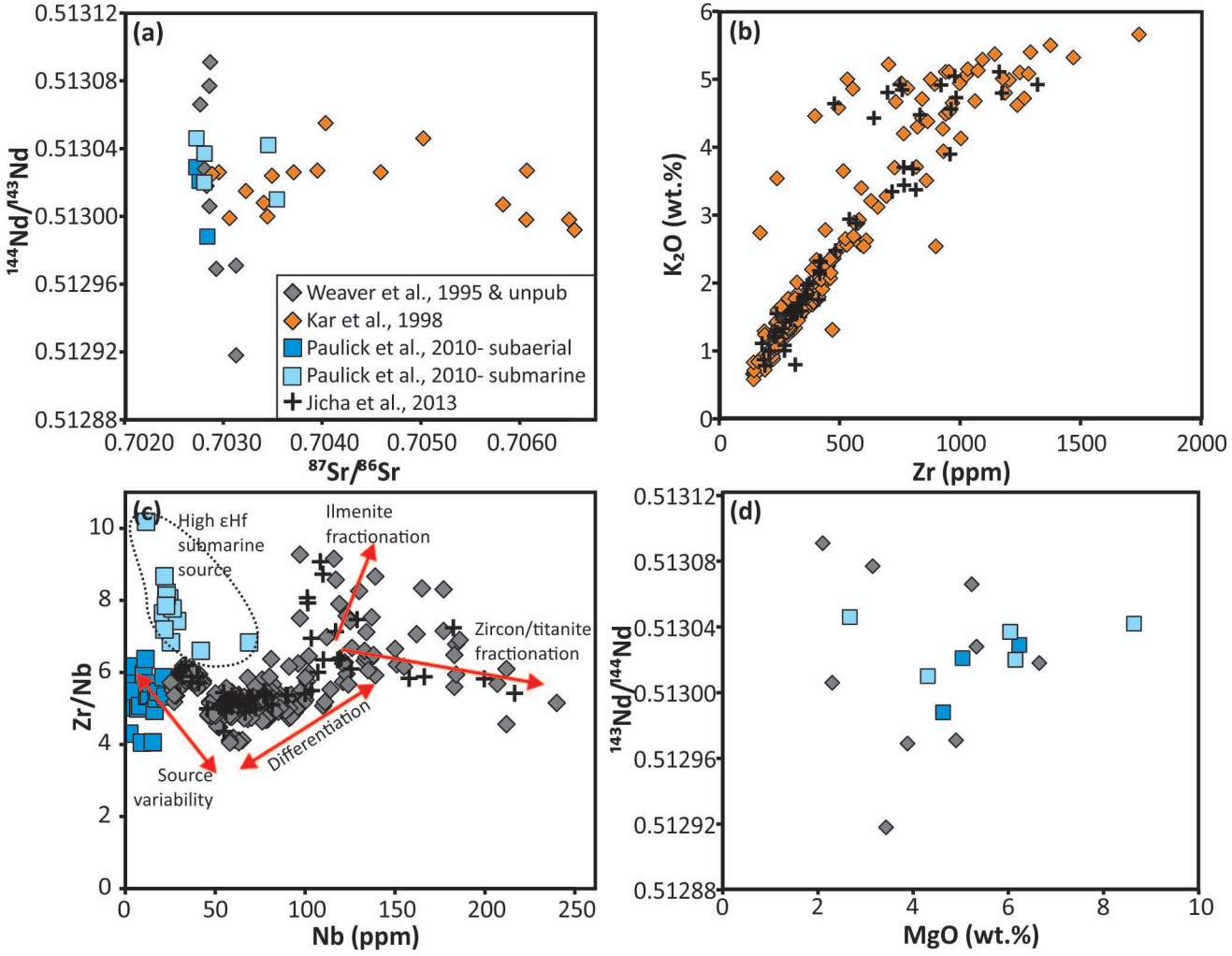
(a)
$^{144}Nd/^{143}Nd$
$^{87}Sr/^{86}Sr$
Weaver et al., 1995 & unpub
Kar et al., 1998
Paulick et al., 2010- subaerial
Paulick et al., 2010- submarine
Jicha et al., 2013
(b)
K_2O (wt.%)
Zr (ppm)
(c)
High εHf submarine source
Ilmenite fractionation
Zircon/titanite fractionation
Differentiation
Source variability
Zr/Nb
Nb (ppm)
(d)
$^{143}Nd/^{144}Nd$
MgO (wt.%)

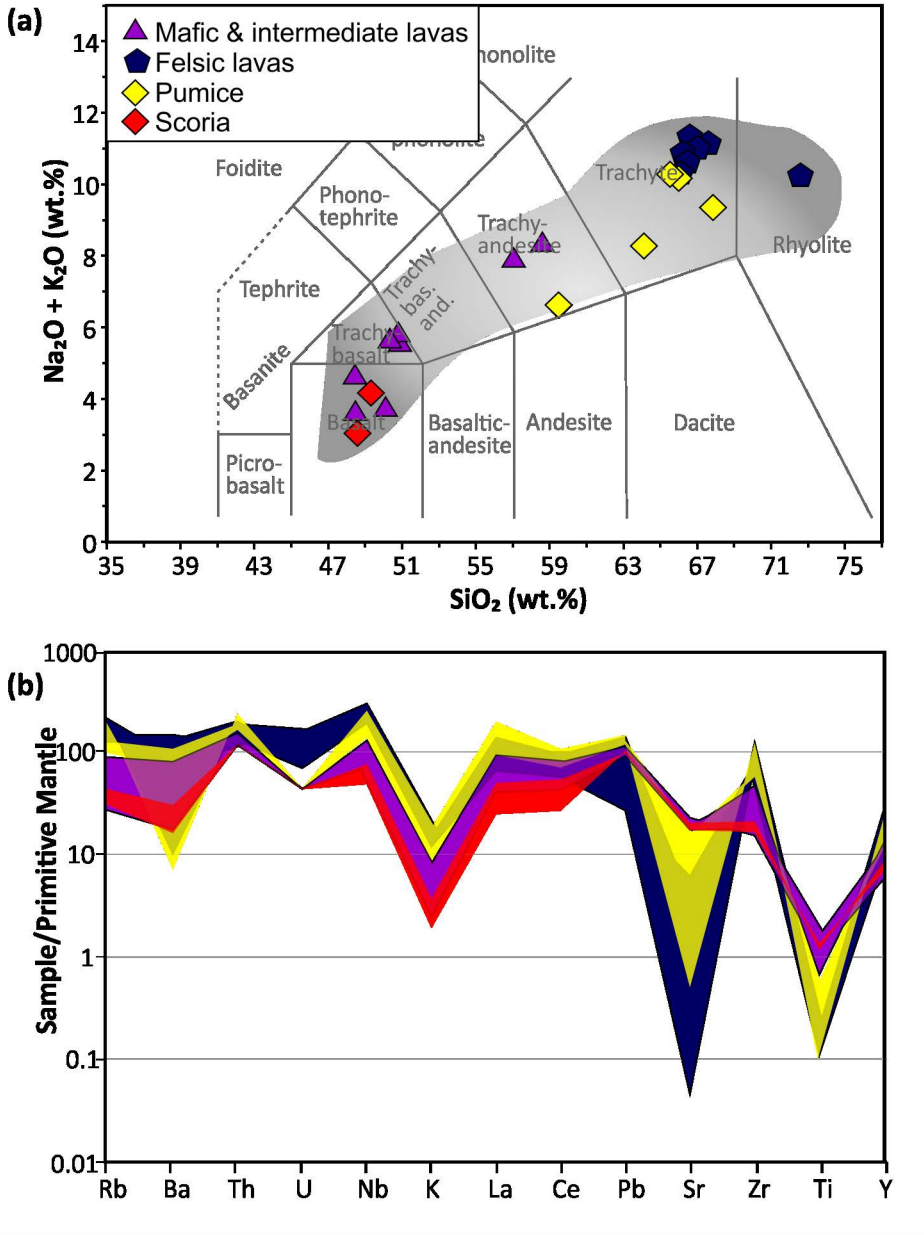
(a)
Mafic & intermediate lavas
Felsic lavas
Pumice
Scoria
Foidite
Phono-tephrite
Tephrite
Basanite
Trachy-bas. and.
Trachy-andesite
Trachyte
Rhyolite
Trachy-basalt
Basalt
Basaltic-andesite
Andesite
Dacite
Picro-basalt
Na2O + K2O (wt.%)
SiO2 (wt.%)
(b)
Sample/Primitive Mantle
Rb
Ba
Th
U
Nb
K
La
Ce
Pb
Sr
Zr
Ti
Y

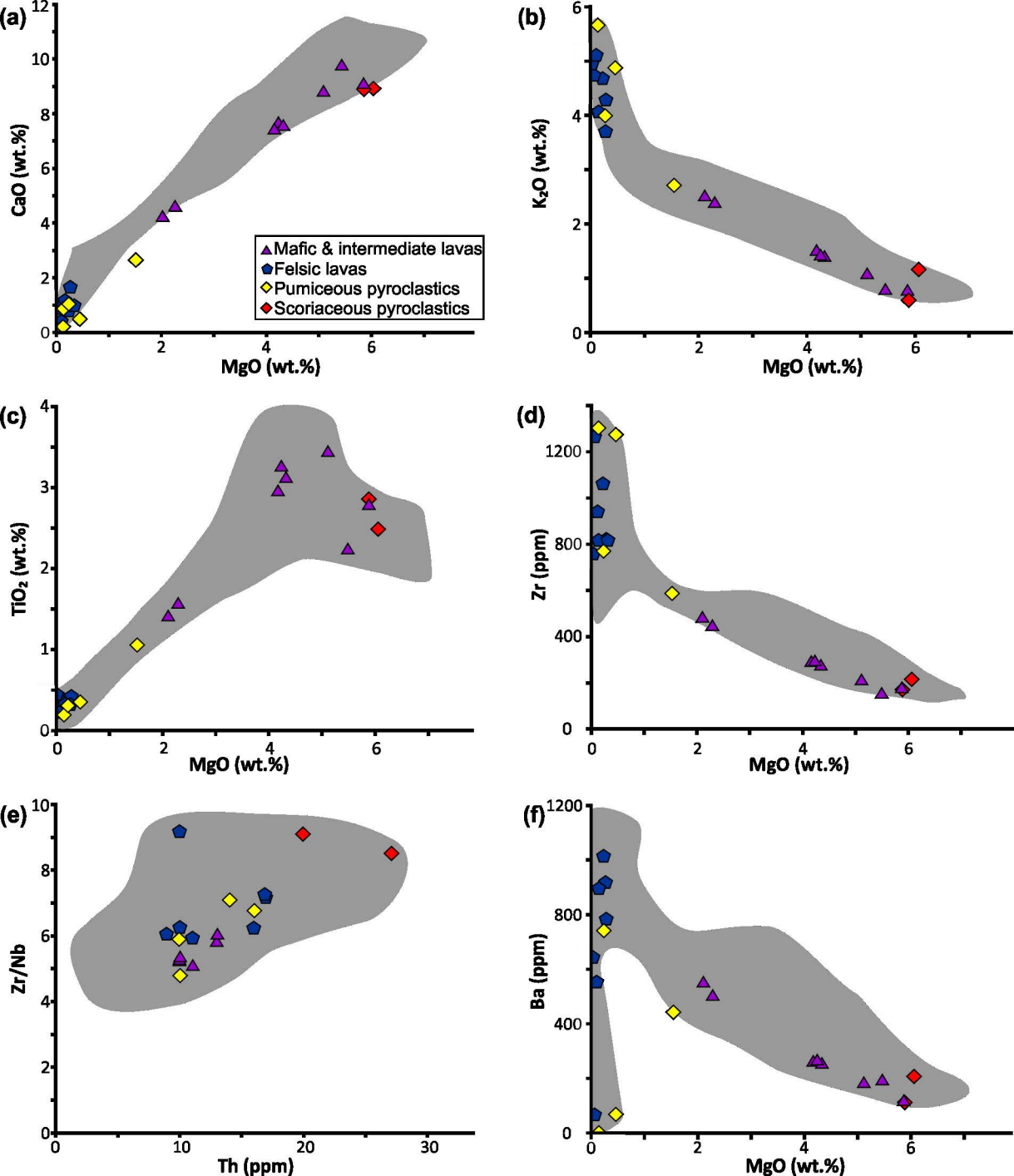
(a)
CaO (wt.%)
MgO (wt.%)
Mafic & intermediate lavas
Felsic lavas
Pumiceous pyroclastics
Scoriaceous pyroclastics
(b)
K2O (wt.%)
MgO (wt.%)
(c)
TiO2 (wt.%)
MgO (wt.%)
(d)
Zr (ppm)
MgO (wt.%)
(e)
Zr/Nb
Th (ppm)
(f)
Ba (ppm)
MgO (wt.%)

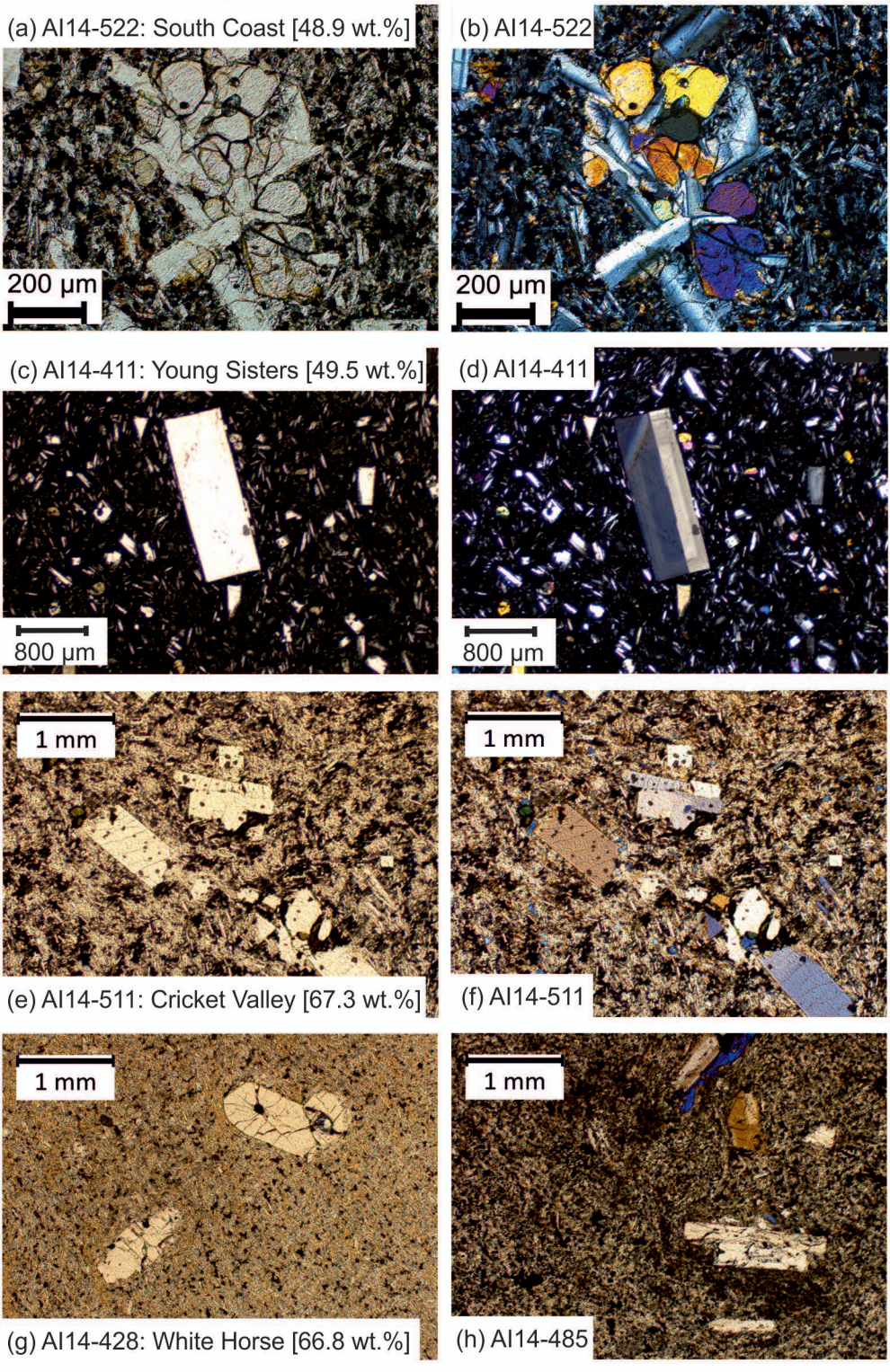
PPL
XPL
(a) Al14-522: South Coast [48.9 wt.%]
200 µm
(b) Al14-522
200 µm
(c) Al14-411: Young Sisters [49.5 wt.%]
800 µm
(d) Al14-411
800 µm
1 mm
1 mm
(e) Al14-511: Cricket Valley [67.3 wt.%]
(f) Al14-511
1 mm
1 mm
(g) Al14-428: White Horse [66.8 wt.%]
(h) Al14-485

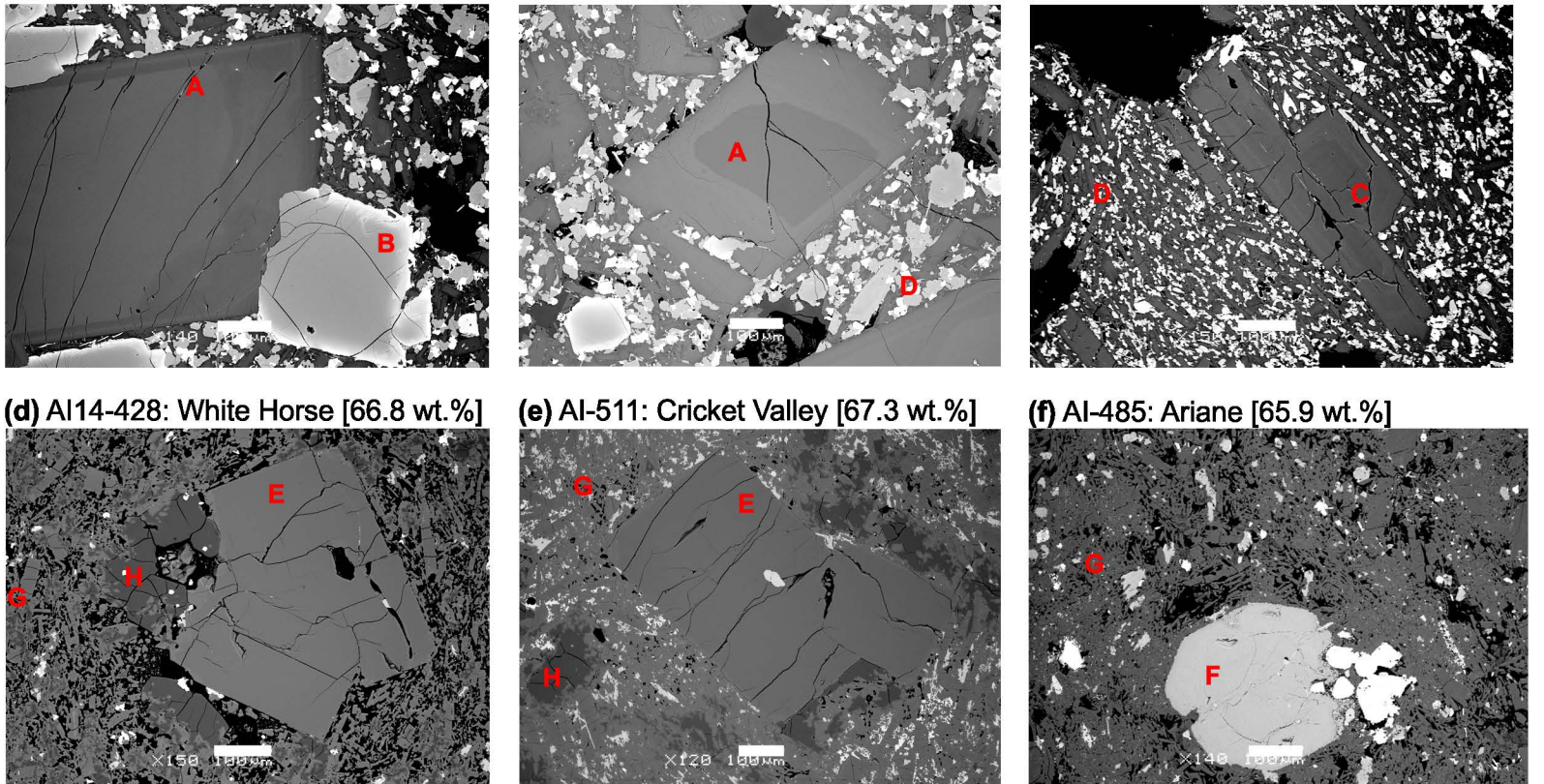
(a) Al-522: South Coast [48.9 wt.%]
A
B
(b) Al-522: South Coast [48.9 wt.%]
A
D
(c) Al-423: Letterbox [57.6 wt.%]
D
C
(d) Al14-428: White Horse [66.8 wt.%]
E
H
G
(e) Al-511: Cricket Valley [67.3 wt.%]
G
E
H
(f) Al-485: Ariane [65.9 wt.%]
G
F

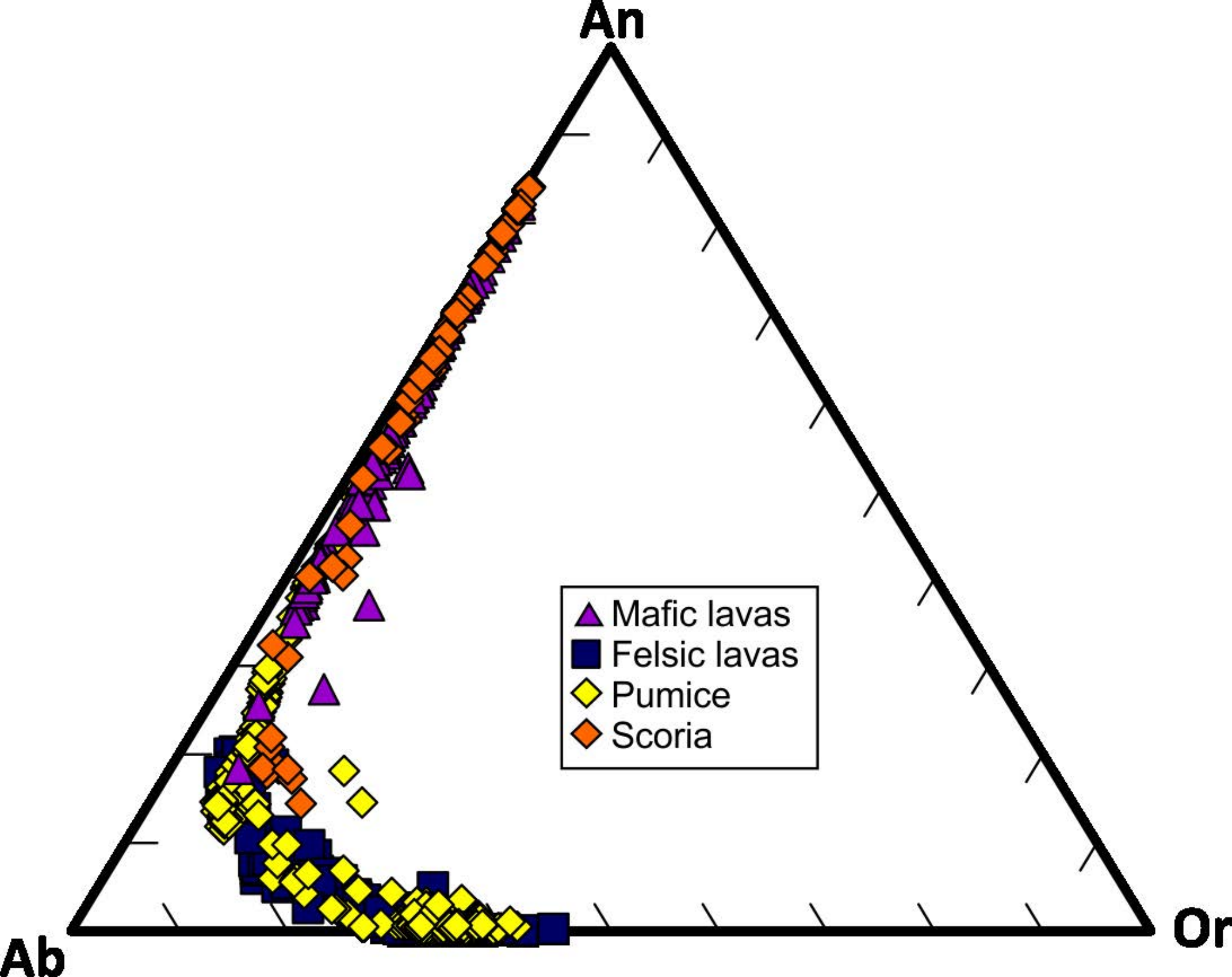
An
Ab
Or
Mafic lavas
Felsic lavas
Pumice
Scoria

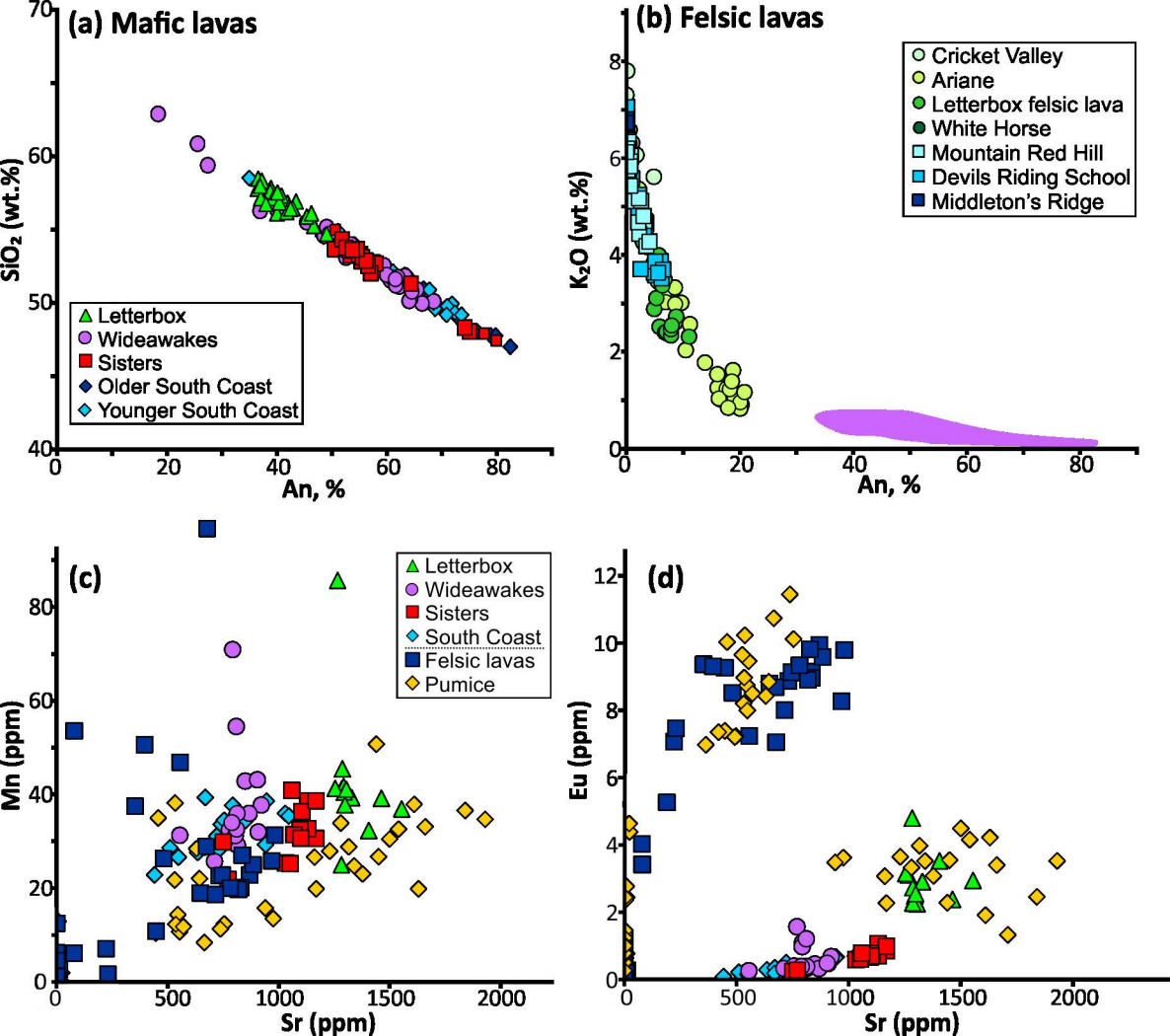
(a) Mafic lavas
SiO2 (wt.%)
An, %
Letterbox
Wideawakes
Sisters
Older South Coast
Younger South Coast
(b) Felsic lavas
K2O (wt.%)
An, %
Cricket Valley
Ariane
Letterbox felsic lava
White Horse
Mountain Red Hill
Devils Riding School
Middleton's Ridge
(c)
Mn (ppm)
Sr (ppm)
Letterbox
Wideawakes
Sisters
South Coast
Felsic lavas
Pumice
(d)
Eu (ppm)
Sr (ppm)

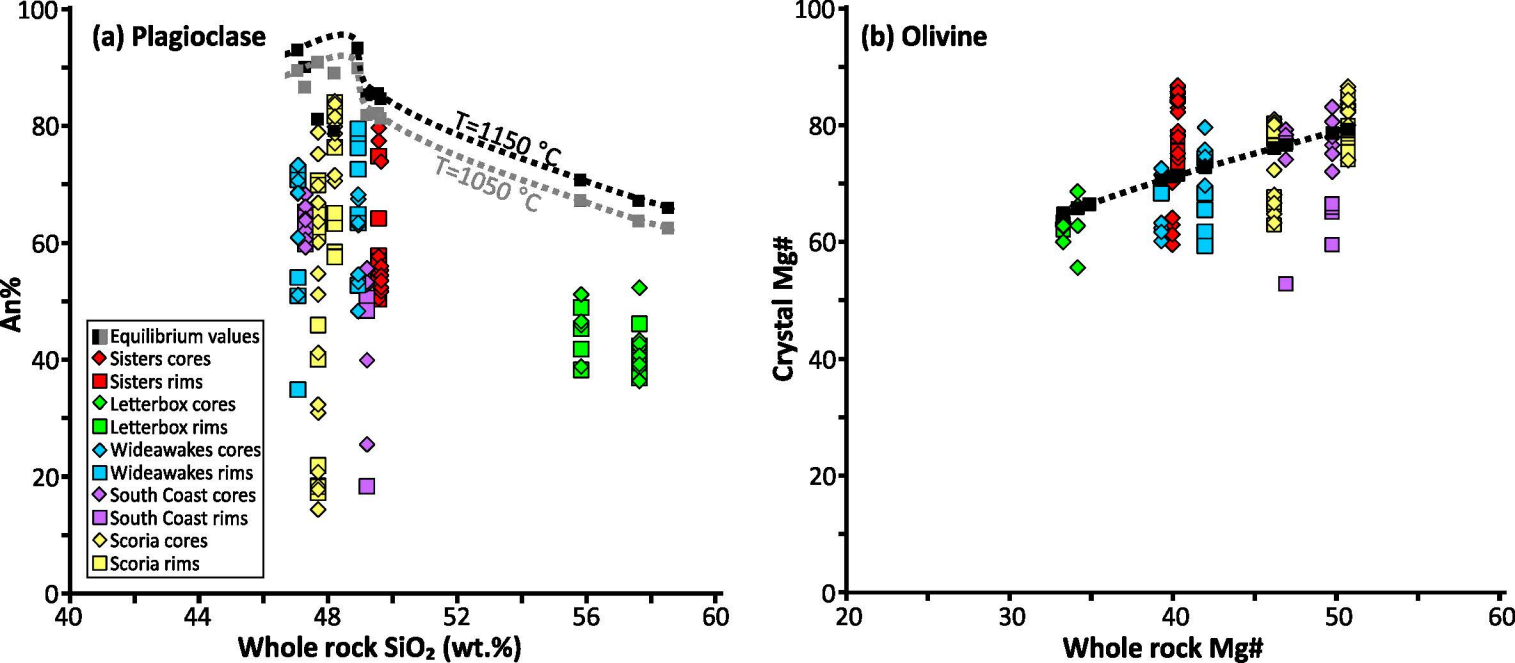
(a) Plagioclase
An%
Whole rock SiO2 (wt.%)
T=1150 °C
T=1050 °C
Equilibrium values
Sisters cores
Sisters rims
Letterbox cores
Letterbox rims
Wideawakes cores
Wideawakes rims
South Coast cores
South Coast rims
Scoria cores
Scoria rims
(b) Olivine
Crystal Mg#
Whole rock Mg#

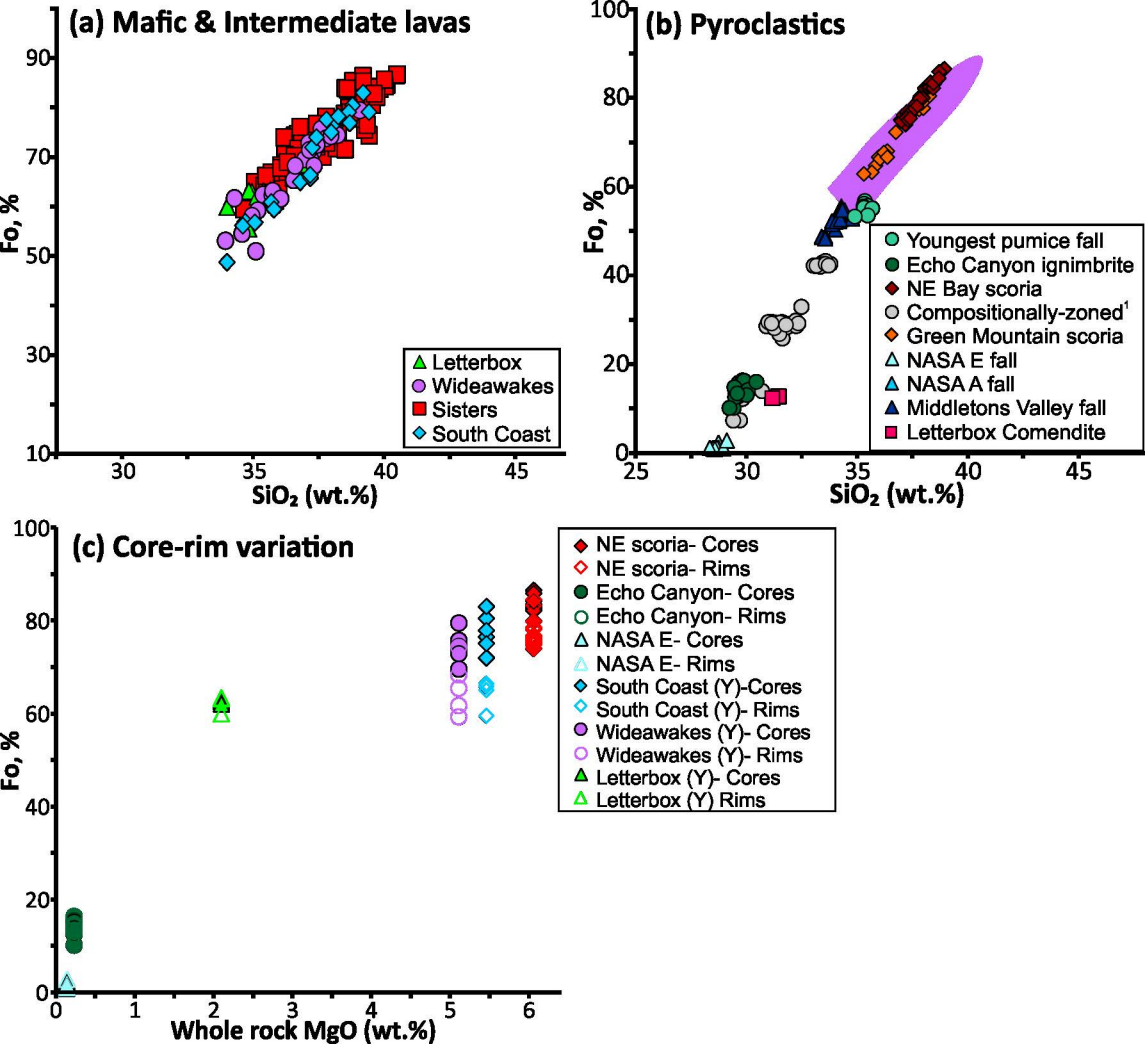
(a) Mafic & Intermediate lavas
Fo, %
SiO2 (wt.%)
Letterbox
Wideawakes
Sisters
South Coast
(b) Pyroclastics
Fo, %
SiO2 (wt.%)
Youngest pumice fall
Echo Canyon ignimbrite
NE Bay scoria
Compositionally-zoned[1]
Green Mountain scoria
NASA E fall
NASA A fall
Middletons Valley fall
Letterbox Comendite
(c) Core-rim variation
Fo, %
Whole rock MgO (wt.%)
NE scoria- Cores
NE scoria- Rims
Echo Canyon- Cores
Echo Canyon- Rims
NASA E- Cores
NASA E- Rims
South Coast (Y)-Cores
South Coast (Y)- Rims
Wideawakes (Y)- Cores
Wideawakes (Y)- Rims
Letterbox (Y)- Cores
Letterbox (Y) Rims

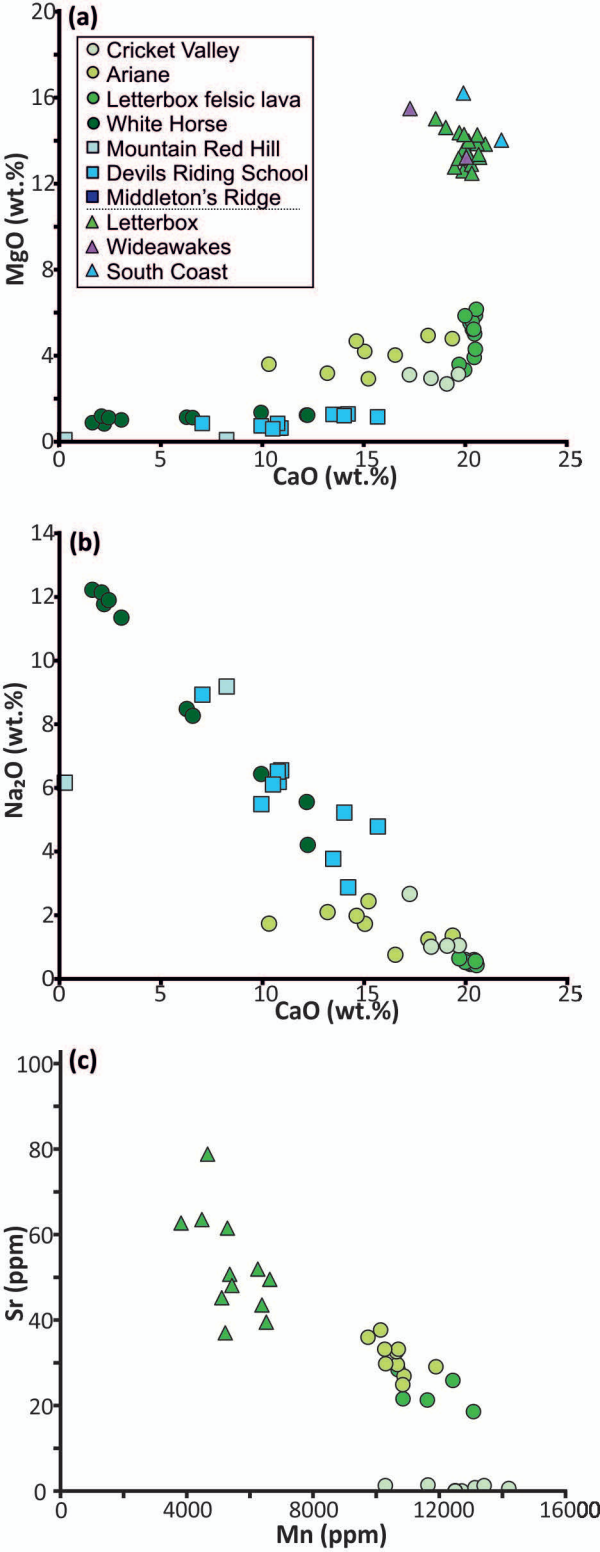
(a)
Cricket Valley
Ariane
Letterbox felsic lava
White Horse
Mountain Red Hill
Devils Riding School
Middleton's Ridge
Letterbox
Wideawakes
South Coast
MgO (wt.%)
CaO (wt.%)
(b)
Na2O (wt.%)
CaO (wt.%)
(c)
Sr (ppm)
Mn (ppm)

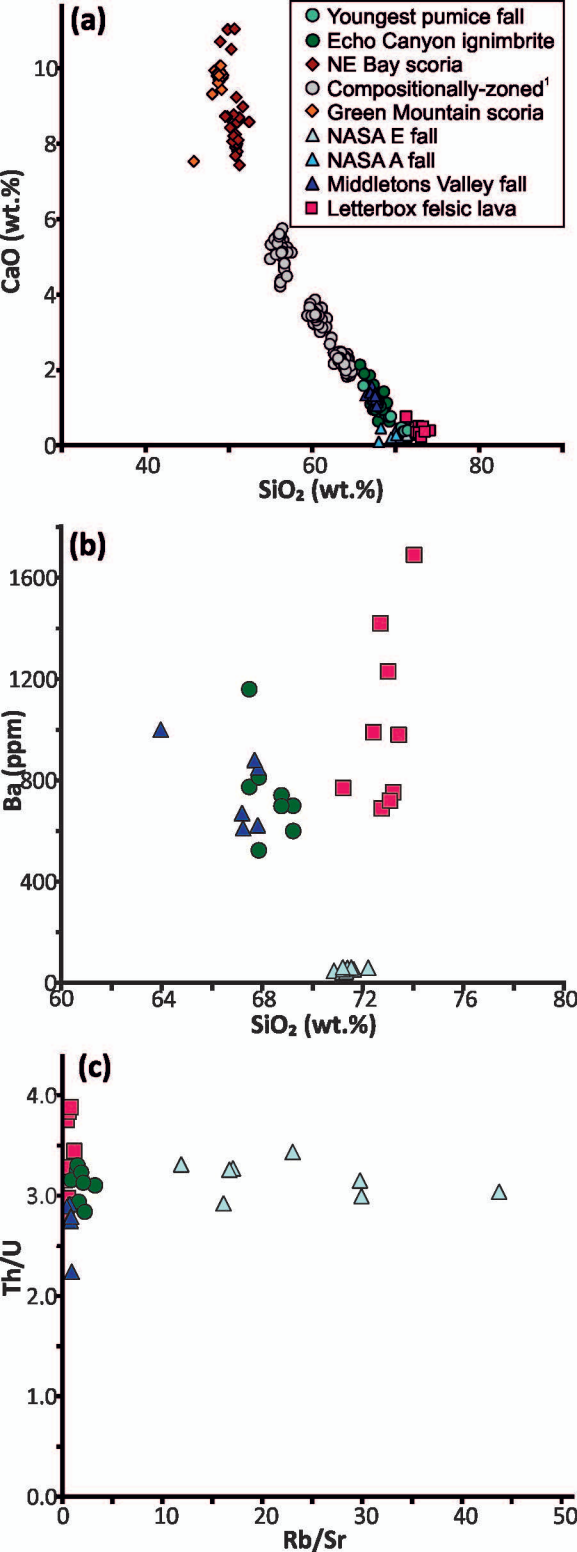
(a)
Youngest pumice fall
Echo Canyon ignimbrite
NE Bay scoria
Compositionally-zoned[1]
Green Mountain scoria
NASA E fall
NASA A fall
Middletons Valley fall
Letterbox felsic lava
CaO (wt.%)
SiO2 (wt.%)
(b)
Ba (ppm)
SiO2 (wt.%)
(c)
Th/U
Rb/Sr

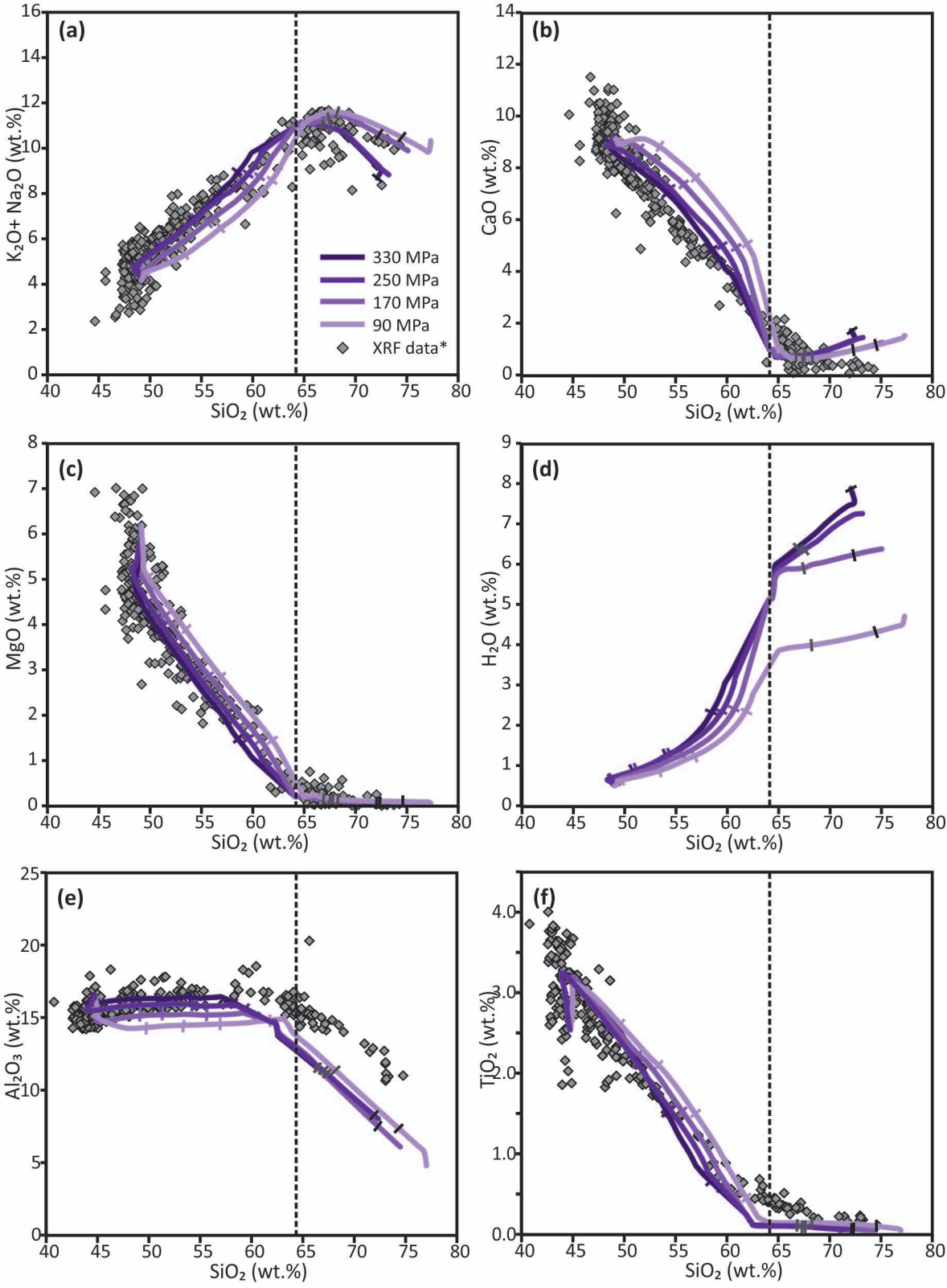
(a)
K_2O+ Na_2O (wt.%)
SiO_2 (wt.%)
330 MPa
250 MPa
170 MPa
90 MPa
XRF data*
(b)
CaO (wt.%)
SiO_2 (wt.%)
(c)
MgO (wt.%)
SiO_2 (wt.%)
(d)
H_2O (wt.%)
SiO_2 (wt.%)
(e)
Al_2O_3 (wt.%)
SiO_2 (wt.%)
(f)
TiO_2 (wt.%)
SiO_2 (wt.%)

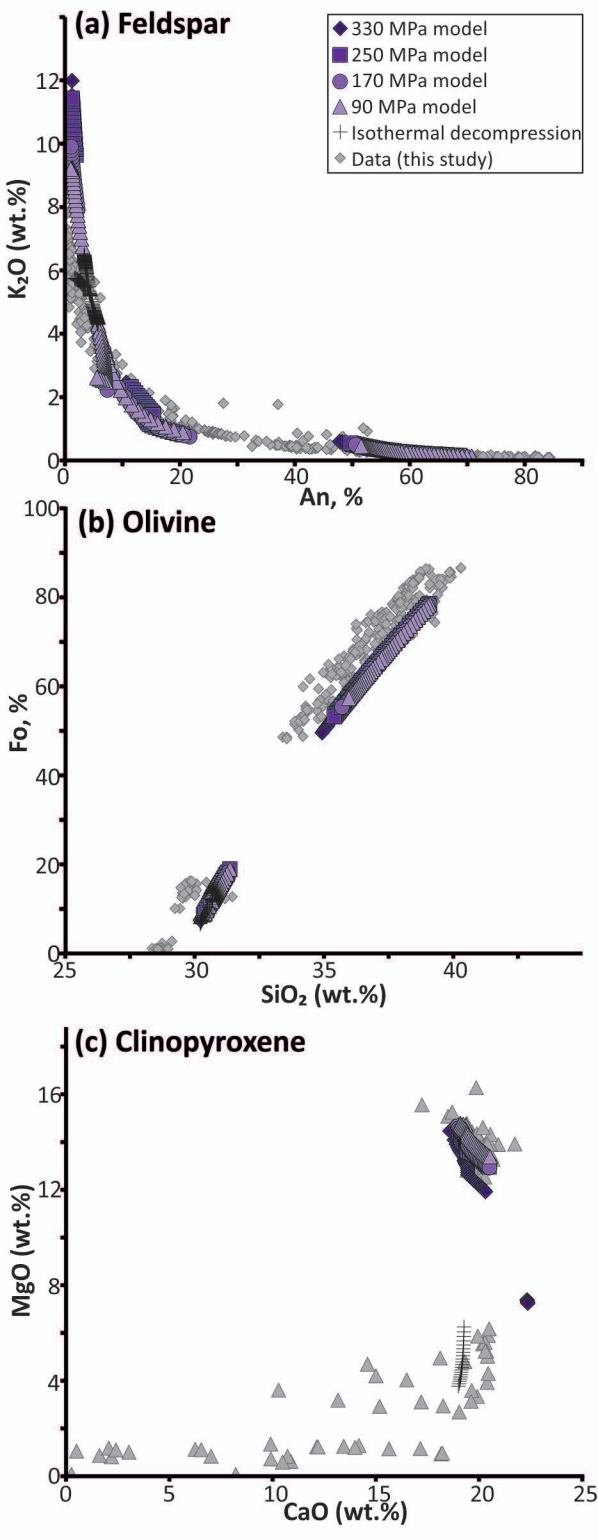
(a) Feldspar
330 MPa model
250 MPa model
170 MPa model
90 MPa model
Isothermal decompression
Data (this study)
K2O (wt.%)
An, %
(b) Olivine
Fo, %
SiO2 (wt.%)
(c) Clinopyroxene
MgO (wt.%)
CaO (wt.%)

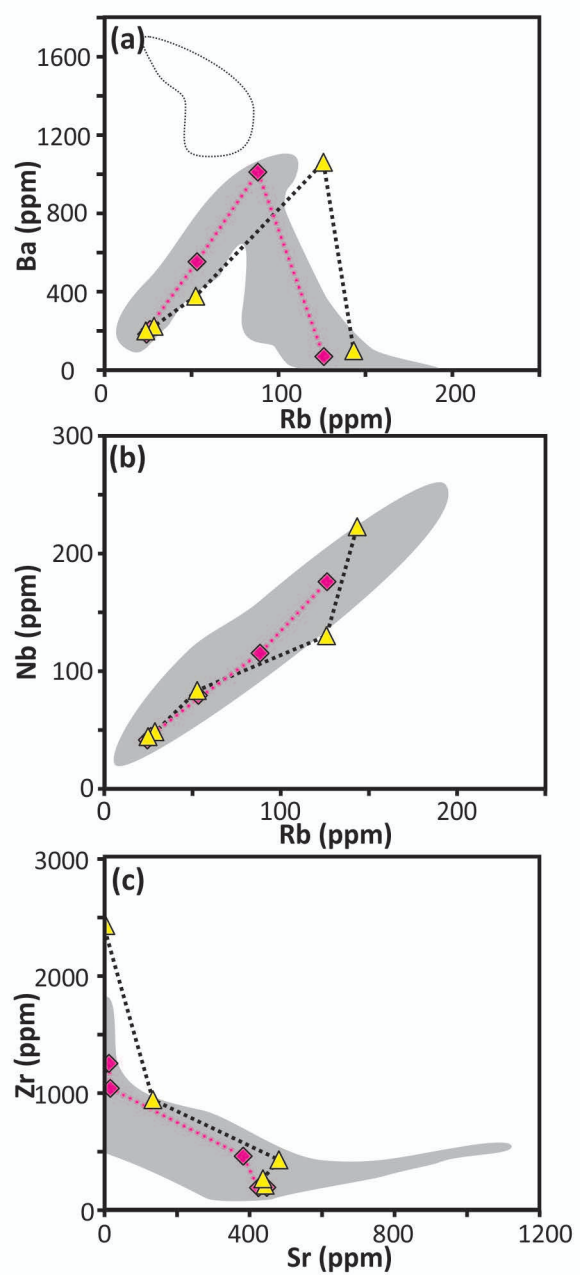
(a)
Ba (ppm)
1600
1200
800
400
0
0
100
200
Rb (ppm)
(b)
Nb (ppm)
300
200
100
0
0
100
200
Rb (ppm)
(c)
Zr (ppm)
3000
2000
1000
0
0
400
800
1200
Sr (ppm)
XRF data field*
XRF data stage 1-4[1]
Modelled outputs stage 1-4[2]

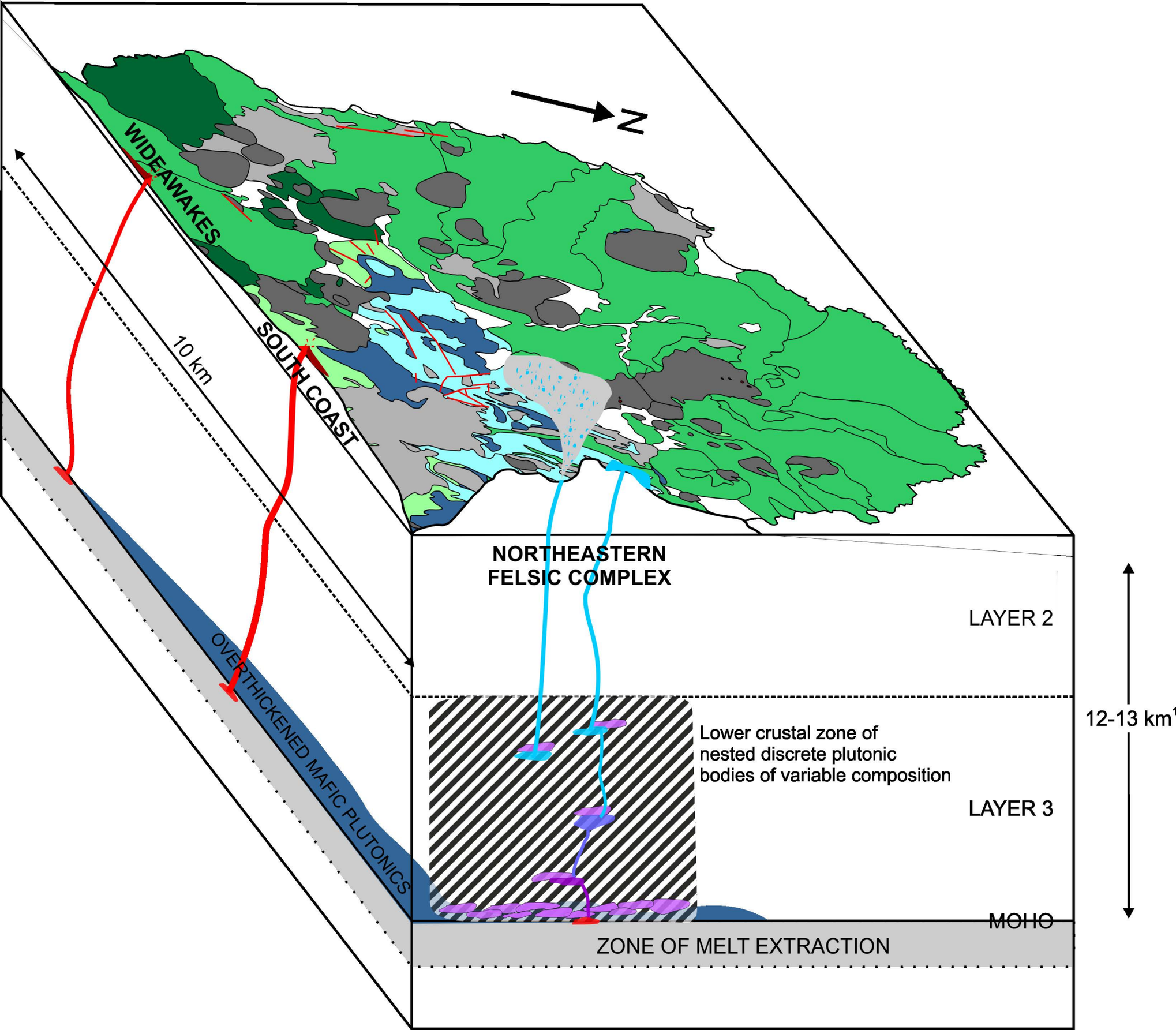
N
WIDE AWAKES
SOUTH COAST
10 km
NORTHEASTERN
FELSIC COMPLEX
LAYER 2
Lower crustal zone of
nested discrete plutonic
bodies of variable composition
LAYER 3
OVERTHICKENED MAFIC PLUTONICS
MOHO
ZONE OF MELT EXTRACTION
12-13 km

Table 1: Samples investigated for this study

Sample number	Region	TAS classification	Sample type	Grid Reference (E, N)	Approximate age of sample
AI14-411	Youngest Sisters	Trachy-basalt	mafic lava	0568706, 9123576	zero age *
AI14-471	Older Sisters	Trachy-basalt	mafic lava	0567966, 9125332	> AI14-411¥
AI14-423	Youngest Letterbox	Trachy-andesite	mafic lava	0577052, 9121328	- -
AI14-429	Older Letterbox	Trachy-andesite	mafic lava	0576443, 9121020	> AI14-423¥
AI14-445	Youngest Wideawakes	Basallt	mafic lava	0566907, 9117906	298 ka *
AI14-449	Older Wideawakes	Trachy-basalt	mafic lava	0568052, 9118271	> 298 ka ¥
AI14-522	Youngest South Coast	Basalt	mafic lava	0575056, 9119068	120 ka ""
AI14-514	Older South Coast	Basalt	mafic lava	0574092, 9119604	> 120 ka ¥
AI14-485	Ariane flow	Trachyte	felsic lava	0573518, 9124726	169 ka *
AI14-511	Cricket Valley	Trachyte	felsic dome	0574341, 0122098	52 ka *
AI14-428	White Horse	Trachyte	felsic dome	0575736, 9121232	zero age *
AI-94	Middleton's Ridge	Rhyolite	felsic lava	05693, 91214	1094 ka *
AI-103	Mountain Red Hill	Trachyte	felsic lava	05706, 91202	602 ka *
AI14-419	Letterbox felsic lava	Trachyte	felsic dome	0576780, 9120822	- -
AI15-621	Devil's Riding School	Trachyte	felsic dome	0568897, 9120365	652 ka*
AI15-618	Youngest pumice fall	Trachyte	pumice fall	0573646, 9123128	- -
AI14-435A	Echo Canyon	Trachyte	pumice flow	0573840, 9124754	- -
AI14-438	NE scoria	Basalt	scoria fall	0573786, 9124790	- -
AI14-493A	NASA unit E	Trachyte	pumice fall	0569420, 9120262	> AI14-488A ¥
AI14-488A	NASA unit A	Trachyte	pumice fall	0569475, 9120264	- -
AI14-459A	Middleton's Valley fall	Trachy-andesite	pumice fall	0569849, 9120661	- -
AI14-552	Green Mountain scoria	Basalt	scoria fall	0571584, 9121198	- -
AI14-439A[+]	*Compositionally-zoned top*	*Trachy-andesite*	*zoned fall*	*0573786, 9124790*	- -
AI14-439D[+]	*Compositionally-zoned mid*	*Trachy-andesite*	*zoned fall*	*0573786, 9124790*	
AI14-439G[+]	*Compositionally-zoned base*	*Trachyte*	*zoned fall*	*0573786, 9124790*	

[+] Data presented in Chamberlain et al., 2016.

* Ar-Ar age data from Jicha et al., 2014

"" K-Ar age data from Harris et al., 1992

¥ Stratigraphic relationship observed in the field

Table 2: Whole rock XRF data for Ascension samples, major elements in wt.%, trace elements in ppm.

Sample number	**AI114-411**	**AI14-471**	**AI14-423**	**AI14-429**	**AI14-445**	**AI14-449**	**AI14-522**	**AI14-514**	**AI14-485**	**AI14-511**	**AI14-428**	**AI-94**	**AI-103**
Location	Young Sisters	Old Sisters	Young Letterbox	Old Letterbox	Younger Wideawakes	Older Wideawakes	Younger South Coast	Older South Coast	Ariane	Cricket Valley	White Horse	Middleton's Mountain Ridge	Red Hill
SiO_2	49.5	49.6	57.6	55.8	47.3	49.2	48.9	47.0	65.9	67.3	66.8	72.5	66.6
TiO_2	3.12	2.97	1.42	1.58	3.44	3.26	2.25	2.79	0.42	0.37	0.41	0.23	0.45
Al_2O_3	15.5	15.5	16.9	16.7	15.3	15.2	16.1	15.5	16.1	15.3	15.5	12.7	15.5
Fe_2O_3	12.5	12.2	8.23	8.63	13.8	12.8	10.8	13.0	4.97	4.62	4.68	3.70	5.85
MnO	0.22	0.22	0.24	0.23	0.20	0.23	0.16	0.18	0.22	0.16	0.18	0.12	0.12
MgO	4.33	4.16	2.10	2.29	5.11	4.24	5.46	5.87	0.28	0.11	0.28	0.06	0.04
CaO	7.55	7.42	4.23	4.62	8.80	7.70	9.8	9.13	1.6	0.88	1.04	0.33	0.38
Na_2O	4.03	4.18	5.68	5.40	3.45	4.09	2.85	2.76	6.62	6.07	6.73	5.60	6.04
K_2O	1.41	1.50	2.53	2.37	1.08	1.44	0.80	0.77	3.71	5.11	4.30	4.72	4.94
P_2O_5	0.89	1.03	0.60	1.04	0.81	1.18	0.53	0.4	0.09	0.06	0.09	0.03	0.06
LOI	-0.10	-0.02	-0.45	-0.51	-0.21	-0.34	0.24	-0.14	0.12	0.00	0.15	0.37	0.95
Total	99.0	98.8	99.0	98.1	99.1	98.9	97.8	97.3	100.1	100.0	100.2	100.4	101.0
Ba	254	263	553	503	183	266	194	120	780	554	919	69	644
Rb	32	34	53	50	24	29	17	16	76	117	94	126	81
Sr	455	461	381	410	423	458	501	391	135	7	24	1	4
Pb	18	20	20	21	17	19	bdl	bdl	5	8	6	10	5
Th	10	10	13	13	11	10	bdl	bdl	9	16	11	17	10
U	bdl	bdl	1	1	1	1	bdl	bdl	bdl	3.7	1.6	bdl	2.0
Zr	279	291	483	450	214	292	158	182	818	940	823	1266	756
Nb	52	55	80	77	42	54	28	29	135	151	139	177	121
Y	41	44	54	52	27	49	24	30	85	62	45	113	57
La	34	35	64	56	28	41	bdl	bdl	71	53	50	78	45
Ce	96	105	144	140	74	115	61	49	156	119	112	177	100
Sc	21	19	12	12	24	18	26	28	9	9	8	3	12
V	227	203	42	55	317	208	252	314	3	4	7	4	3
Ni	8	5	3	5	24	3	56	65	5	3	4	6	5
Zn	122	128	128	132	115	130	83	105	150	126	136	197	151

Sample number	**AI114-419**	**AI15-621**	**AI15-618**	**AI14-435A**	**AI14-438**	**AI14-493A**	**AI14-488A**	**AI14-459A**	**AI14-552**
Location	Letterbox Felsic lava	Devils Riding School	Youngest Pumice fall	Echo Canyon	NE scoria	NASA unit E	NASA unit A	Middleton's Valley fall	Green Mountain scoria
SiO_2	65.5	66.9	65.0	65.6	48.2	68.1	64.3	58.5	47.7
TiO_2	0.32	0.33	0.33	0.31	2.49	0.18	0.33	1.06	2.85
Al_2O_3	15.9	15.4	13.7	15.7	16.1	13.1	14.5	17.6	16.0
Fe_2O_3	4.58	4.41	4.05	4.34	11.5	3.74	5.18	5.59	13.4
MnO	0.17	0.17	0.16	0.20	0.19	0.11	0.19	0.16	0.18

MgO	0.15	0.22	0.16	0.23	6.06	0.14	0.46	1.53	5.88
CaO	0.87	1.03	0.80	1.08	8.93	0.21	0.49	2.65	8.90
Na_2O	6.48	6.76	5.23	6.35	2.95	3.78	3.47	3.84	2.41
K_2O	4.06	4.68	4.84	4.00	1.15	5.66	4.88	2.72	0.60
P_2O_5	0.57	0.04	0.07	0.04	0.94	0.02	0.03	0.37	0.31
LOI	0.27	0.93	4.57	2.70	-0.56	5.73	6.90	4.68	0.15
Total	98.9	100.9	98.9	100.5	97.9	100.8	100.7	98.7	98.3
Ba	898	1011	49	740	207	bdl	68	446	111
Rb	75	88	121	77	26	139	105	61	19
Sr	83	15	50	79	446	bdl	11	338	381
Pb	26	5	bdl	24	18	27	24	22	19
Th	17	10	20	16	10	27	20	14	10
U	2	3.4	bdl	bdl	1	bdl	bdl	1	1
Zr	818	1062	948	770	216	1301	1276	589	171
Nb	114	116	147	114	45	152	140	83	29
Y	76	73	89	72	35	96	88	52	28
La	95	57	109	91	34	135	127	64	17
Ce	157	117	173	162	94	188	186	124	47
Sc	6	10	bdl	bdl	23	bdl	bdl	6	28
V	2	4	bdl	bdl	209	bdl	bdl	34	307
Ni	3	7	bdl	bdl	65	bdl	bdl	6	45
Zn	138	145	141	142	111	171	179	103	105

Table 3: Petrography of Ascension lavas

Sample number	Region	TAS classification	Percentage Phenocrysts*	Vesicularity (%)	Fspar	Ol	Cpx	Cbt	Aeg	Glass	Ox+Accessory
AI14-411	Youngest Sisters	Trachy-basalt	<1 (f)	5	67	5	20				8
AI14-471	Older Sisters	Trachy-basalt	<1 (f)	7	68	10	17				5
AI14-445	Youngest Wideawakes	Basallt	3 (f, ol)	3	68	14	12				6
AI14-449	Older Wideawakes	Trachy-basalt	<1 (f, ol)	6	55	9	32				4
AI14-423	Youngest Letterbox	Trachy-andesite	<1 (f)	5	80	6	10				4
AI14-429	Older Letterbox	Trachy-andesite	2 (f)	43	77	8	9				6
AI14-522	Youngest South Coast	Basalt	40 (f, ol)	3	62	31	<1				7
AI14-514	Older South Coast	Basalt	18 (f, ol)	23	56	23					21
AI14-428	White Horse	Trachyte	2 (f)	24	64			29	4		3
AI14-511	Cricket Valley	Trachyte	6 (f, aeg)	1	78			12	9		1
AI14-485	Ariane flow	Trachyte	4 (f)	15	77			19			4
AI14-419	Letterbox felsic lava	Trachyte	<1 (f)	25	60		1	1		37	1
AI-103	Mountain Red Hill	Trachyte	2 (f, ox)	4	70			24	5		1
AI15-621	Devil's Riding School	Trachyte	3 (f)	13	68			27	4		1
AI-94	Middleton's Ridge	Rhyolite	<1 (f)	18	57			35	6		2

Arranged by relative age (see Table 1 and references therein)
Crystal percentages represent groundmass (<500 μm) crystals as well as those represented as phenocryst phases; Fspar = feldspar (plagioclase and ternary); Ol = olivine; Cpx = clinopyroxene; Cbt = cristobalite; Aeg = aegirine; Ox+Acc = bright in Back Scattered Electron imagery oxides and accessory phases including zircon and apatite.
*Phenocrysts used to represent phases > 500 μm in thin sectioned area. Phases which constitute phenocryst phases indicated in brackets: f= feldspar, ol = olivine; cpx = clinopyroxene; aeg = aegirine; ox = oxides;

Table 4: Representative feldspar data for Ascension samples

Sample	**AI114-411**				**AI14-423**		**AI14-445**		**AI14-522**		**AI14-485**		
Location	Young Sisters				Young Letterbox		Young Wideawakes		Young South Coast		Ariane		
Rock type	Trachy-basalt				Trachy-andesite		Basalt		Basalt		Trachyte		
Spot location	**F3-C**	**F3-R**	**F5-C**	**F5-R**	**F1-C**	**F1-R**	**F5-C**	**F5-R**	**F1-C**	**F1-R**	**K3-C**	**K3-R**	**K10-C**
SiO_2	53.50	53.29	47.46	52.69	56.56	56.19	52.57	51.22	48.05	51.89	63.33	61.71	62.46
TiO_2	0.16	0.17	0.05	0.13	0.04	0.06	0.13	0.16	0.05	0.10	0.00	0.01	0.01
Al_2O_3	28.26	28.18	32.79	29.25	26.89	26.57	28.59	29.16	32.44	29.44	22.67	23.21	23.19
FeO*	0.91	0.92	0.45	0.77	0.37	0.49	0.77	0.87	0.46	0.66	0.20	0.24	0.25
MgO	0.10	0.09	0.13	0.11	0.04	0.05	0.12	0.13	0.15	0.15	0.00	0.01	0.01
CaO	11.45	11.61	16.66	12.19	8.93	8.88	12.20	12.80	15.92	13.46	3.48	4.44	4.28
Na_2O	5.04	5.10	2.30	4.74	6.55	6.63	4.48	4.29	2.67	4.17	9.17	8.56	8.87
K_2O	0.32	0.33	0.07	0.26	0.36	0.36	0.24	0.23	0.10	0.18	1.26	1.17	0.83
Total	99.76	99.70	99.91	100.15	99.75	99.23	99.10	98.87	99.86	100.05	100.11	99.34	99.90
An	54.6	54.7	79.7	57.8	42.1	41.7	59.3	61.4	76.3	63.4	16.1	20.8	20.0
Ab	43.5	43.5	19.9	40.7	55.9	56.3	39.3	37.2	23.1	35.6	76.9	72.7	75.3
Or	1.8	1.9	0.4	1.5	2.0	2.0	1.4	1.4	0.6	1.0	7.0	6.5	4.7
Sc	4.55	4.90	4.64	4.60	4.6	3.11	6.38	12.0	8.48	7.22	6.60	5.20	8.00
Ti	421	612	696	664	254	344	797	4970	508	526	136	137	147
V	0.53	1.60	1.73	1.58	0.42	0.51	3.49	83	3.12	2.41	0.16	bdl	0.48
Mn	32.8	32.6	36.5	38.8	37.7	36.9	37.9	323	37.8	28.3	27.0	25.0	27.0
Ga	21.2	20.0	24.9	23.0	24.8	26.0	24.7	22.9	23.1	23.1	28.2	27.1	26.8
Rb	0.31	0.45	0.28	0.14	0.86	0.56	0.93	2.90	0.24	0.32	1.56	1.64	1.29
Sr	1130	1096	1104	1168	1289	1317	922	811	793	718	834	883	836
Y	0.19	0.18	0.20	0.40	0.64	0.40	0.57	9.00	0.11	0.08	0.02	0.13	0.13
Zr	0.41	0.22	0.00	0.11	2.80	1.54	1.26	31.5	0.50	0.17	bdl	1.86	0.25
Ba	134	137	121	175	295	324	109	131	70.7	86.2	1248	1353	1087
La	3.16	2.76	2.46	2.71	5.88	6.40	2.13	9.23	1.08	1.10	8.29	7.78	7.35
Ce	5.21	3.73	3.61	4.33	8.62	6.47	4.00	20.0	1.93	1.55	9.14	9.42	8.43
Pr	0.54	0.41	0.24	0.42	0.90	0.81	0.37	2.33	0.17	0.18	0.74	0.57	0.60
Nd	2.24	0.99	1.00	1.55	2.10	2.36	1.72	11.4	0.59	0.70	1.71	1.80	1.51
Sm	0.23	0.09	0.34	0.41	0.57	0.19	0.31	2.37	0.04	bdl	0.13	0.00	0.17
Eu	1.07	0.68	0.78	0.98	3.04	2.50	0.68	1.21	0.38	0.39	8.97	9.59	9.15
Gd	0.17	0.27	0	0.25	0.35	0.20	0.25	2.44	bdl	0.06	bdl	0.21	0.17
Yb	bdl	bdl	bdl	bdl	0.13	bdl	0.01	0.61	0.02	bdl	0.00	0.00	0.00
Pb	0.40	0.22	0.26	0.22	0.84	0.65	0.23	0.63	0.22	0.10	1.04	1.01	0.84

Sample	**AI114-485**	**AI14-511**		**AI14-419**		**AI14-435A**		**AI14-493A**		**AI14-488A**		**AI14-459A**		
Location	Ariane	Cricket Valley		Letterbox felsic lava		Echo Canyon		NASA Unit E		NASA Unit A		Middletons Valley		
Rock type	Trachyte	Trachyte		Trachyte		Trachyte		Trachyte		Trachyte		Trachy-andesite		
Spot location	**F10-R**	**F2-C**	**F2-R**	**F3-C**	**F3-R**	**F4-C**	**F4-R**	**F26-C**	**F26-R**	**K13-C**	**K13-R**	**K18-C**	**K18-R**	**K20-C**
SiO_2	65.60	65.20	65.89	65.20	64.76	65.21	65.91	67.98	68.53	68.51	67.88	62.04	61.39	58.09
TiO_2	0.03	0.02	0.01	0.00	0.00	0.00	0.01	0.00	0.00	0.00	0.01	0.02	0.07	0.04
Al_2O_3	19.42	19.33	19.00	20.71	20.90	21.22	20.57	19.24	19.53	19.36	19.31	22.50	23.09	24.64
FeO*	0.53	0.32	0.31	0.17	0.20	0.22	0.18	0.29	0.24	0.28	0.32	0.34	0.49	0.35
MgO	0.00	0.00	0.00	0.00	0.00	0.00	0.00	0.00	0.00	0.01	0.00	0.03	0.03	0.04
CaO	0.75	0.23	0.07	1.44	1.67	3.21	2.59	0.07	0.12	0.13	0.12	5.10	5.86	7.59
Na_2O	8.56	7.79	7.74	9.19	9.13	8.96	9.28	7.50	7.73	7.53	8.03	8.28	7.96	7.29
K_2O	4.37	6.30	6.54	2.40	2.46	1.12	1.40	6.64	6.36	6.08	5.92	0.94	0.74	0.48
Total	99.28	99.22	99.57	99.10	99.14	99.95	99.93	101.71	102.52	101.89	101.58	99.25	99.62	98.52
An	3.5	1.1	0.3	6.9	7.9	15.5	12.3	0.3	0.6	0.6	0.6	24.1	27.7	35.5
Ab	72.2	64.6	64.1	79.4	78.2	78.1	79.8	63.0	64.5	64.9	67.0	70.6	68.1	61.8
Or	24.3	34.4	35.6	13.7	13.9	6.4	7.9	36.7	34.9	34.5	32.4	5.3	4.2	2.7
Sc	6.90	6.77	7.44	0.33	6.97	3.90	5.20	6.30	3.20	5.20	6.90	5.20	4.20	3.60
Ti	156	104	76.5	6.89	124	105	104	62.0	84.0	69.8	67.7	229	264	352
V	0.31	0.45	0.17	0.02	bdl	0.11	bdl	bdl	1.70	0.09	0.01	bdl	1.40	1.70
Mn	20.1	1.20	0.60	2.55	7.00	22.1	11.8	1.10	bdl	2.10	bdl	19.9	28.0	34.8
Ga	27.8	25.6	24.5	0.95	28.7	28.0	25.9	32.2	34.7	30.7	35.3	29.5	23.5	33.9
Rb	2.40	39.0	47.3	0.33	10.2	2.06	1.91	51.2	45.7	32.8	33.0	1.56	2.16	1.18
Sr	828	1.31	0.81	13.0	222	644	571	0.79	2.28	2.35	1.46	1169	1230	1930
Y	0.31	0.17	0.03	0.19	0.79	0.04	0.00	0.00	0.00	0.00	0.00	0.10	0.27	0.36
Zr	2.70	3.22	0.45	2.17	bdl	0.00	0.00	bdl	2.90	0.30	0.47	bdl	5.50	1.80
Ba	1261	120	80.6	96.7	3770	1680	1552	66.0	129	194	97.4	533	753	448
La	8.60	0.67	0.42	0.48	6.96	7.35	6.03	0.65	0.66	0.43	0.56	11.6	12.4	11.7
Ce	9.90	0.68	0.23	0.73	8.47	8.37	7.14	0.13	0.30	0.37	0.17	15.2	14.2	15.9
Pr	0.74	0.02	bdl	0.07	0.72	0.48	0.52	0.00	0.00	0.00	0.00	1.01	1.14	0.85
Nd	2.40	0.27	0.04	0.28	2.20	1.47	1.24	0.00	0.00	0.00	0.00	3.10	3.60	3.10
Sm	0.26	0.03	bdl	0.05	0.22	0.00	0.00	0.00	0.00	0.00	0.00	0.00	0.00	0.27
Eu	9.82	0.98	0.99	0.28	7.07	8.85	8.50	0.73	1.00	1.25	1.00	2.27	3.65	3.53
Gd	0.18	0.01	bdl	0.04	0.35	0.00	0.00	0.00	0.00	0.00	0.00	0.00	0.04	0.00
Yb	0.00	bdl	bdl	0.02	0.00	0.00	0.00	0.00	0.00	0.00	0.00	0.00	0.00	0.00
Pb	1.21	1.12	0.93	0.07	1.94	1.29	1.34	0.53	0.88	0.89	0.69	1.91	1.85	1.02

Major element data given as wt.%; Anorthite, albite and orthoclase (An, Ab, Or) contents as mol. %; trace elements in ppm. For full data set, see Electronic Appendix 2. Where elements are below the detection limits of the method, bdl is written. Spot location refers to the analysis being core [C] or rim [R].

Table 5: Representative olivine major and trace element data for selected Ascension samples

Sample	**AI14-411**		**AI14-423**		**AI14-445**		**AI14-522**		**AI14-435A**		**AI14-493A**	
Location	Young Sisters		Young Letterbox		Young Wideawakes		Young South Coast		Echo Canyon		NASA unit E	
Rock type	Trachy-basalt		Trachy-andesite		Basalt		Basalt		Trachyte		Trachyte	
Spot tag	**16_C**	**16_R**	**2_C**	**2_R**	**6_C**	**6_R**	**6_C**	**6_R**	**3_C**	**3_R**	**10_C**	**10_R**
SiO_2	39.59	38.43	35.49	35.07	38.96	37.31	37.93	37.17	29.42	29.23	28.74	29.11
Al_2O_3	0.06	0.00	0.02	0.02	0.03	0.03	0.03	0.04	0.00	0.00	0.00	0.00
FeO*	14.67	24.67	32.21	32.30	19.05	28.37	22.89	29.63	59.56	59.01	62.61	61.38
MnO	0.22	0.76	1.10	1.13	0.25	0.48	0.33	0.56	4.96	4.94	5.53	5.48
MgO	43.65	34.97	30.98	30.87	41.46	34.30	38.63	32.92	3.77	3.73	0.83	0.98
CaO	0.22	0.26	0.18	0.18	0.25	0.26	0.34	0.32	0.31	0.32	0.31	0.52
Cr_2O_3	0.03	bdl	0.00	0.00	0.01	0.00	0.00	0.00	0.00	0.00	0.00	0.00
NiO	0.19	0.00	0.01	0.00	0.15	0.04	0.07	0.05	0.02	0.00	0.00	0.00
P_2O_5	--	--	0.10	0.04	0.01	0.04	0.01	0.03	--	--	--	--
Total	98.63	99.16	100.15	99.65	100.19	100.83	100.25	100.73	98.04	97.24	98.02	97.48
Fo (%)	84.1	71.7	63.2	63.0	79.5	68.3	75.1	66.5	10.1	10.1	2.3	2.8
Fa (%)	15.9	28.3	36.8	37.0	20.5	31.7	24.9	33.5	89.9	89.9	97.7	97.2

Major element data given as wt.%; Fosterite, fayalite contents as mol. %. For full data set, see Electronic Appendix 2. Spot location refers to the analysis being core [C] or rim [R].

Table 6: Representative clinopyroxene major element data for selected Ascension samples

Sample	**AI14-423**		**AI14-429**		**AI14-449**		**AI14-522**		**AI14-485**	**AI14-511**		**AI14-428**		**AI14-419**		**AI15-621**		**AI15-618**	
Location	Young Letterbox		Old Letterbox		Old Wideawakes		Young South Coast		Ariane	Weatherpost		White Horse		Letterbox bedrock		Devils Riding School		Young pumice fall	
Rock type	Trachy-andesite		Trachy-andesite		Trachy-basalt		Basalt		Trachyte	Trachyte		Trachyte		Trachyte		Trachyte		Trachyte	
Spot tag	**2_C**	**2_R**	**GM**	**GM**	**1_C**	**1_R**	**1_C**	**1_R**	**GM**	**GM**	**GM**	**GM**	**GM**	**1_C**	**1_R**	**GM**	**GM**	**10_C**	**10_R**
SiO_2	48.35	50.51	49.37	36.12	50.22	48.46	50.63	47.34	47.79	47.74	47.90	50.81	50.86	48.50	48.20	47.94	49.82	51.82	51.58
TiO_2	1.27	0.75	0.97	0.02	0.96	2.25	1.09	1.94	2.05	0.29	0.42	1.95	1.88	0.39	0.53	0.32	0.47	0.63	0.56
Al_2O_3	3.62	1.98	3.03	0.02	2.15	5.37	2.82	5.19	2.59	0.29	0.33	2.35	3.50	0.70	0.89	0.21	1.99	1.59	1.69
FeO*	9.50	9.65	12.42	31.46	11.76	9.61	8.44	8.11	25.67	26.08	26.72	27.00	24.79	22.35	22.84	27.99	26.35	11.30	10.81
MnO	0.47	0.61	0.72	1.09	0.67	0.25	0.19	0.15	2.38	1.54	1.64	1.25	1.25	1.52	1.47	1.37	0.91	0.72	0.67
MgO	13.93	14.33	12.66	30.88	15.56	13.23	16.29	13.92	3.21	2.71	2.97	0.84	1.12	5.04	5.26	1.17	0.86	15.26	13.92
CaO	20.54	20.55	19.84	0.14	17.24	20.05	19.86	21.74	13.17	19.05	18.26	2.19	2.41	20.41	20.30	15.64	10.73	18.70	20.34
Na_2O	0.49	0.50	0.55	0.01	0.46	0.56	0.29	0.39	2.09	1.04	1.01	11.76	11.88	0.51	0.53	4.78	6.50	0.43	0.50
K_2O	0.00	0.03	0.00	0.00	0.01	0.00	0.00	0.01	0.09	0.00	0.00	0.70	1.24	0.01	0.01	1.39	2.06	0.00	0.01
Cr_2O_3	0.00	0.00	0.00	0.00	0.00	0.00	0.13	0.23	0.00	0.00	0.00	bdl	bdl	0.00	bdl	bdl	0.00	0.00	0.00
Total	98.16	98.91	99.58	99.74	99.03	99.78	99.76	99.02	99.05	98.74	99.25	98.85	98.94	99.44	100.02	100.81	99.69	100.45	100.09

Major element data given as wt.%. For full data set, see Electronic Appendix 2. Spot location refers to the analysis being core [C], rim [R] or groundmass [GM].

Table 7: Representative glass analyses from Ascension Island
7a: Major element analyses normalised to 100 wt.%

Sample	**AI14-419**		**AI15-618**		**AI14-552**		**AI14-438**		**AI14-435A**			**AI14-493A**		**AI14-488A**		**AI14-459A**	
Location	Letterbox felsic lava		Young pumice		Green Mountain sc.		NE scoria		Echo Canyon			NASA unit E		NASA unit A		Middelton's Valley fall	
Spot Tag	**419-1**	**419-2**	**15-5**	**15-6**	**1-1**	**1-4**	**14-1**	**14-2**	**10-2**	**10-3**	**10-4**	**8-1**	**8-4**	**15-1**	**15-2**	**4-1**	**4-3**
SiO_2	71.21	72.69	70.64	70.74	48.91	49.14	50.79	50.99	67.86	69.22	67.98	71.17	71.30	71.07	70.11	67.23	67.60
TiO_2	0.27	0.31	0.19	0.19	3.68	3.72	3.61	3.52	0.10	0.29	0.22	0.21	0.22	0.17	0.18	0.48	0.49
Al_2O_3	12.04	10.48	13.26	12.91	13.51	13.87	13.54	12.90	17.98	13.88	16.01	12.33	11.78	13.67	13.60	16.80	16.64
FeO*	5.64	5.77	4.50	4.89	13.53	13.27	12.02	11.97	1.38	4.47	3.43	4.77	4.87	3.28	3.96	2.78	2.94
MnO	0.27	0.28	0.27	0.25	0.15	0.23	0.19	0.20	0.08	0.19	0.16	0.18	0.16	0.12	0.20	0.07	0.06
MgO	0.06	0.07	0.03	0.02	5.32	5.41	3.78	4.52	0.02	0.08	0.09	0.02	0.02	0.00	0.00	0.54	0.50
CaO	0.77	0.51	0.48	0.46	9.70	9.43	7.91	8.56	0.65	0.64	0.90	0.29	0.28	0.46	0.45	1.32	1.23
Na_2O	5.15	4.44	6.14	6.11	3.34	3.16	3.48	3.22	7.32	5.43	6.09	5.52	4.42	4.42	4.95	5.88	5.73
K_2O	4.56	5.41	4.46	4.40	1.20	1.10	2.19	2.21	4.36	5.03	4.47	4.75	5.94	6.14	5.74	4.41	4.43
BaO	0.00	0.00	0.00	0.00	0.05	0.07	0.08	0.06	0.11	0.06	0.09	0.04	0.00	0.00	0.00	0.09	0.04
P_2O_5	0.03	0.04	0.03	0.01	0.57	0.56	1.97	1.74	0.04	0.01	0.00	0.03	0.01	0.04	0.01	0.11	0.10
Cl	0.00	0.00	0.00	0.00	0.04	0.05	0.11	0.12	0.11	0.43	0.34	0.54	0.60	0.56	0.54	0.25	0.24
F	0.00	0.00	0.00	0.00	0.00	0.00	0.33	0.00	0.00	0.27	0.22	0.14	0.40	0.07	0.26	0.03	0.00
Total	100	100	100	100	100	100	100	100	100	100	100	100	100	100	100	100	100

Major element data given as wt.%. For full data set, see Electronic Appendix 2.

Table 7b: Selected trace element data from glass in felsic samples (all elements in ppm); where elements are below the detection limits of the method, bdl is written. Analyses in italics previously published in Chamberlain et al., 2016.

Sample	**AI14-419**		**AI14-435A**		**AI14-493A**		**AI14-459A**			***AI14-439D***		***AI14-439G***		
Location	Letterbox felsic lava		Echo Canyon		NASA unit E		Middleton's Valley fall			*Compositionally-zoned mid (D) and upper (G)*				
Tag	**G1**	**G2**	**G1**	**G2**	**G1**	**G2**	**G1**	**G2**	**G3**	**G1**	**G2**	**G1**	**G2**	**G3**
Li	10.0	15.0	10.0	17.0	15.5	29.0	24.0	bdl	13.0	*13.6*	*18.0*	*29.0*	*20.0*	*18.0*
Sc	13.6	15.9	13.8	12.8	9.70	9.40	5.00	11.1	13.0	*11.2*	*21.0*	*27.0*	*10.1*	*27.0*
Ti	994	1020	1705	1300	1448	1437	5400	4960	5400	*2360*	*5690*	*4200*	*4530*	*2900*
V	1.60	1.20	0.71	bdl	4.37	6.80	10.1	10.0	21.0	*bdl*	*5.30*	*1.10*	*33.8*	*11.0*
Mn	863	820	1544	1290	1259	1270	1720	1060	1190	*1160*	*2720*	*2130*	*1290*	*1550*
Zn	84	90	154	215	268	239	178	113	94	*97*	*164*	*134*	*107*	*155*
Ga	34	32	30	32	39	42	57	38	33	*16*	*37*	*35*	*27*	*17*
Rb	101	58	90	90	169	182	166	134	161	*44*	*73*	*97*	*56*	*64*
Sr	90	106	50	44	10	8	246	175	220	*175*	*390*	*184*	*117*	*159*
Y	76	49	77	80	124	129	52	44	38	*34*	*74*	*70*	*41*	*79*
Zr	930	584	791	868	1507	1661	1180	1000	1310	*286*	*620*	*760*	*490*	*830*
Nb	133	89	147	161	234	247	160	135	141	*64*	*138*	*141*	*83*	*98*
Ba	746	1240	790	720	55	61	950	651	1020	*470*	*900*	*1290*	*840*	*1300*
La	76	51	83	83	138	145	93	65	71	*41*	*73*	*81*	*54*	*79*
Ce	160	113	169	178	274	283	197	124	145	*75*	*160*	*153*	*102*	*153*
Pr	18	12	19	20	30	30	17	12	9	*7*	*19*	*15*	*12*	*19*

Nd	67	50	73	77	112	115	57	43	45	*33*	*85*	*60*	*43*	*75*
Sm	16.9	9.3	15.3	14.8	24.2	23.9	13.6	8.2	7.8	*8*	*12.9*	*14.8*	*8.5*	*10.2*
Eu	2.67	3.92	3.24	2.52	2.61	2.40	2.57	2.40	2.60	*1.72*	*4.60*	*4.40*	*3.06*	*3.60*
Gd	11.6	8.8	13.8	14.9	21.9	22.4	10.6	6.1	10.0	*7.0*	*12.0*	*11.6*	*10.2*	*8.9*
Dy	13.3	11.0	14.4	14.1	23.6	24.2	9.4	7.3	10.0	*7.7*	*11.2*	*11.8*	*7.8*	*14.6*
Er	8.10	5.66	8.45	7.91	12.93	13.39	5.30	5.20	4.70	*3.70*	*8.10*	*7.40*	*4.40*	*4.90*
Yb	8.70	6.70	7.97	7.48	11.91	13.00	4.60	5.20	6.20	*3.60*	*7.80*	*6.70*	*2.50*	*5.50*
Lu	1.18	1.00	1.15	1.15	1.61	1.76	1.18	0.81	0.60	*0.27*	*0.99*	*0.59*	*0.37*	*0.51*
Hf	18.6	12.7	17.1	19.2	30.3	33.8	26.8	21.0	23.5	*6.9*	*12.8*	*14.5*	*9.2*	*13.2*
Ta	7.2	5.0	8.5	9.0	13.3	13.4	11.1	9.5	6.9	*3.2*	*6.8*	*6.1*	*4.5*	*6.9*
W	2.50	0.79	1.88	1.95	3.58	4.00	5.50	2.77	1.90	*0.54*	*2.00*	*1.03*	*1.00*	*1.14*
Pb	5.91	4.65	6.75	6.79	14.37	13.06	13.50	10.20	4.30	*2.90*	*4.10*	*6.30*	*3.50*	*6.20*
Th	10.9	7.8	10.8	10.7	21.1	21.8	20.5	16.0	16.0	*4.2*	*8.7*	*7.9*	*5.7*	*9.1*
U	3.15	2.02	3.33	3.40	6.42	6.32	7.00	5.80	5.70	*1.13*	*2.71*	*2.20*	*1.82*	*2.77*

Table 8: Intensive variables modelled for Ascension Island samples

Sample number	Region	FeTi-Oxide Thermometry[1]		Feldspar-melt Thermometry [2,3]	
		T (°C)	fO_2 (ΔNNO)	T (°C)	wt.% H_2O[4]
AI14-411	Youngest Sisters	935	-0.4	1150	
AI14-471	Older Sisters	--	--	1152	
AI14-423	Youngest Letterbox	990	-0.05	1093	
AI14-429	Older Letterbox	1025	+0.08	1110	
AI14-445	Youngest Wideawakes	985	-0.34	1167	
AI14-511	Cricket Valley	884	-1.6	886	5.2
AI14-428	White Horse	--	--	837	5.5
AI-94	Middleton's Ridge	--	--	772	4.7
AI-103	Mountain Red Hill	967	-1.9	801	7.2
AI14-419	Letterbox felsic lava	--	--	837	
AI15-621	Devil's Riding School	--	--	871	5.1
AI15-618	Youngest pumice fall	--	--	847	6.4
AI14-435A	Echo Canyon	--	--	993	
AI14-438	NE scoria	--	--	1164	
AI14-493A	NASA unit E	--	--	811	7.1
AI14-488A	NASA unit A	--	--	813	8.1
AI14-459A	Middleton's Valley fall	950	-0.2	1034	
AI14-552	Green Mountain scoria	--	--	1174	
AI14-439A[+]	*Compositionally-zoned scoria*	*845*	*-2.28*		
AI14-439G[+]	*Compositionally-zoned pumice*	*866*	*-1.94*		

[1]Using the calibration of Ghiorso & Evans, 2008, on oxides which have passed the equilibrium test of Bacon & Hirschmann (1988).
[2] Plagioclase-melt thermometry from Putirka (2008), only analyses where K_D(Ab-An) was 0.1 ± 0.11 for T < 1050 °C, or 0.27 ± 0.05 at T > 1050 °C were used (Putirka, 2008).
[3]Alkali-feldspar-melt thermometry (Putirka, 2008). Only analyses within the equilibrium bounds outlined in Mollo et al. (2015) were used.
[4] Alkali-feldspar-melt hygrometry (Mollo et al., 2015). Only analyses within the equilibrium bounds outlined in Mollo et al. (2015) were used. Uncertainties of ±0.7 wt.% consistent with that published in Mollo et al. (2015) are assumed.